ORIGINAL CONTAINS
COLOR ILLUSTRATIONS

LASA

Lidar Atmospheric Sounder and Altimeter

EARTH OBSERVING SYSTEM
Volume IId

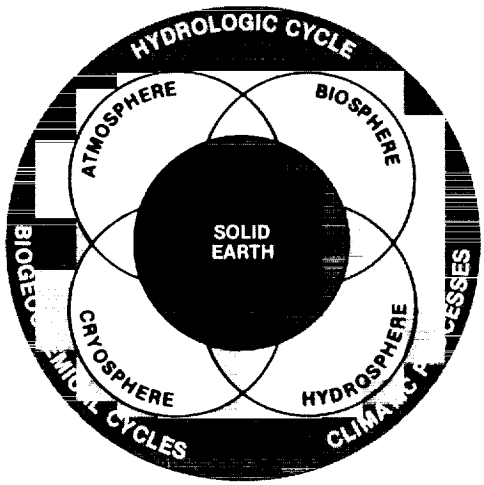

INSTRUMENT PANEL REPORT

National Aeronautics and
Space Administration

1987

EARTH OBSERVING SYSTEM REPORTS

Volume I	Science and Mission Requirements Working Group Report
Volume II	From Pattern to Process: The Strategy of the Earth Observing System Science Steering Committee Report
Volume IIa	Data and Information System Data Panel Report
N87-18906 → Volume IIb	MODIS Moderate-Resolution Imaging Spectrometer Instrument Panel Report
Volume IIc	HIRIS & SISEX High-Resolution Imaging Spectrometry: Science Opportunities for the 1990s Instrument Panel Report
Volume IId	LASA Lidar Atmospheric Sounder and Altimeter Instrument Panel Report
Volume IIe	HMMR High-Resolution Multifrequency Microwave Radiometer Instrument Panel Report
Volume IIf	SAR Synthetic Aperture Radar Instrument Panel Report
Volume IIg	LAWS Laser Atmospheric Wind Sounder Instrument Panel Report
Volume IIh	Altimetric System Panel Report

LIDAR ATMOSPHERIC SOUNDER AND ALTIMETER PANEL FOR THE EARTH OBSERVING SYSTEM

Robert J. Curran, Chairman
Richard R. Nelms, Executive Secretary
Frank Allario
Robert A. Bindschadler
Edward V. Browell
Jack L. Bufton
Robert L. Byer
Steven Cohen
John J. Degnan
William B. Grant
Reynold Greenstone
William S. Heaps
Benjamin M. Herman
Antony Jalink
Dennis K. Killinger
Laurence Korb
James B. Laudenslager
M. Patrick McCormick
S. Harvey Melfi
Robert T. Menzies
Volker Mohnen
James Spinhirne
H. J. Zwally

PREFACE

The Lidar Atmospheric Sounder and Altimeter (LASA) Panel was organized to develop the scientific objectives and corresponding engineering requirements for a lidar instrument as part of NASA's Earth Observing System (Eos) study. The initial concept of LASA was described in Volume I of the Earth Observing System Reports (Butler *et al.*, 1984). The Panel members were selected by the Earth Science and Applications Division of NASA Headquarters.

The primary task of the LASA Panel was to develop the specific objectives for this lidar instrument, give a rationale for the observational requirements, and identify the envelope of instrument parameters needed to satisfy the observational requirements. This task was accomplished through a series of panel meetings held over a one and one-half year period. The necessary simulation calculations and report writing were performed by the Panel members at their respective home organizations. Meeting logistics as well as the difficult job of document preparation were most ably handled by Ms. Lori Nelson, Ms. Terry Edgar, and Ms. Dianna Gemma of Birch & Davis Associates, Inc. It is a pleasure to acknowledge the support provided by the staff of Birch & Davis Associates, Inc. Recording of the proceedings of the Panel meetings and the arduous task of final editing of this report was performed by Mr. Reynold Greenstone of ORI, Inc. The Panel wishes to acknowledge the strongly professional efforts of Mr. Greenstone, without which this report would be considerably less well organized.

A number of individuals aided in discussions with the Panel to develop its relationship to other instruments in Eos. Drs. Robert S. Fraser and Howard Gordon discussed the contribution LASA could make to correcting passive observations to be made in the visible and infrared. Dr. Ramesh Kakar described the anticipated accuracy and resolution that microwave instruments will provide in remotely sensing atmospheric water vapor. Drs. Wayne Esaias and William L. Barnes helped in developing a synergism between LASA and the Moderate-Resolution Imaging Spectrometer (MODIS). Dr. Robert Thomas helped in defining the scientific rationale for LASA's use in determining ice and snow mass balance.

Robert J. Curran
Chairman, LASA Instrument Panel
Washington, D.C.

EXECUTIVE SUMMARY

One of the major opportunities facing Earth scientists in the next decade is the deployment of new satellite instrument technologies. These new devices can provide both unique observational measurements not previously achievable and measurements with greater accuracy, precision, and resolution than passive and active remote sensors currently in use. This report provides recommendations and background for an active laser remote-sensing system designed to be a significant contributor to Eos, the Earth Observing System of the 1990s.

The new active laser remote-sensing system has been designated the Lidar Atmospheric Sounder and Altimeter (LASA). LASA will be part of a complement of new instruments to fly in polar orbit. Working together, these instruments will form an Earth observing system to provide the information needed to further understanding of the fundamental, global-scale processes which govern the Earth's environment. The outline of Eos is set forth in Volume I of the Earth Observing System Reports (Butler *et al.*, 1984). The Science and Mission Requirements Working Group identified the role of active laser observations in Eos.

The LASA Panel was created to consider the role that the rapidly evolving light detection and ranging (lidar) technology could play in furthering the interdisciplinary objectives of Eos. The conclusions and recommendations of the LASA Panel discussed in this report are directed both toward a series of atmospheric composition and structure measurements, and toward a set of surface ranging measurements using laser techniques.

Lidars operate in the ultraviolet, visible, and infrared regions of the electromagnetic spectrum. Their use permits derivation of remotely sensed atmospheric profiles with unprecedented resolution. Lidar can be used to measure distances to centimeter-level precision over a wide range of terrestrial baselines. In a retroranging mode, distance measurements can be used to determine relative motion and deformation of the lithospheric plates, and they can also be used to study the Earth's crustal movements. In an altimetric mode, lidars can be used to measure the topography of the Earth's surface. In performing altimetry and retroranging, lidar's shorter wavelengths offer surface footprints in tens of meters leading to improved measurement and discrimination of land features. Lidar's improved resolution has also enabled the accurate detection of small crustal displacements for accurate measurements of tectonic plate motions.

The remote measurement of atmospheric, land, and oceanic properties with active optical techniques has progressed rapidly since the invention of the laser in 1960. Lidar can be used to measure remotely from space atmospheric parameters such as the height of the planetary boundary layer (PBL), the vertical and horizontal distribution of atmospheric aerosols, cloud-top heights, the vertical distributions of atmospheric trace gases such as water vapor and ozone, and the vertical distributions of atmospheric pressure and temperature. In making composition measurements of the atmosphere, lidar provides enhanced vertical resolution (50 to 100 m for aerosols and clouds and 0.5 to 1 km for gases). Such high resolution is consistent with many atmospheric science requirements. For many of these parameters lidar provides a new measurement capability; for others, lidar provides measurements with improved vertical resolution and decreased size of the ground footprint.

As an optical device, lidar has the advantage of high-sensitivity detection, with capability in some cases to detect single photons. (Photomultiplier tubes and solid-state detectors are well developed at lidar wavelengths.) A further lidar advantage is its high level of monochromaticity. With these advantages, lidar may be used to uniquely measure molecular concentrations against interfering background spectra. With the development of tunable laser sources, molecular species such as water vapor and ozone as well as the atmospheric structure parameters, pressure and temperature, can be measured through the Differential Absorption Lidar (DIAL) technique. Thus, lidar has a unique capability to make many measurements from space that cover an altitude range from the stratosphere through the troposphere to the surface of the Earth.

At most of the available wavelengths, strong return signals from the ground and clouds are obtained with lidar. Additionally, laser sources with pulse lengths in the picosecond range and high repetition rates (>1 kHz) have been achieved. These pulse characteristics, coupled to modern signal processing and electronic filtering techniques, permit measurement of physical heights to an unprecedented centimeter resolution and accuracy. Ice and terrain roughness at centimeter scales can be measured via laser-pulse waveform analysis for footprints an order of magnitude smaller (with correspondingly higher resolution) than can be measured with radar.

The LASA concept incorporates two separable remote-sensing techniques. Sensing of atmospheric properties is the primary role of the LASA instrument proper whereas measurement of Earth surface features is the role of a separately designated instrument identified as the Geodynamics Laser-Ranging System (GLRS). The LASA instrument can function as an altimeter with somewhat limited vertical resolution as compared to GLRS, which has the potential of achieving 10 cm resolution.

SCIENCE OBJECTIVES

The LASA Panel concentrated on five major scientific objectives derived from the major thrusts of Eos:

1. Improve understanding of the global hydrological cycle through observations of atmospheric water vapor.
2. Improve understanding of the role of aerosols and clouds in the physical climate system.
3. Improve understanding of the large-scale structure and dynamics of the Earth's atmosphere through globally distributed high-resolution observations of atmospheric composition and structure.
4. Improve understanding, through altimetry, of the processes that influence ice and snow amount.
5. Improve understanding of geodynamic processes through retroranging to locally and globally distributed reflectors and through altimetric mapping of land topography.

In order to arrive at a recommended set of experiments responsive to these broad scientific objectives, the LASA Panel reviewed the current status and future potential of lidar techniques in the Eos era. These reviews included the technology readiness of laser sources, lidar detectors, telescopes, and optical receivers. The status of calibration techniques and associated subsystems such as laser wavemeters and spectrometers was also reviewed.

The LASA Panel recommends that the LASA instrument package be incorporated within Eos in a time-phased manner consistent with the technological readiness of the lidar components. The measurement objectives in the areas of the global hydrological cycle, aerosols and clouds, and atmospheric state parameters and ozone are to be met by the LASA instrument proper. The further measurement objectives, ice-sheet mass balance and land topography, and crustal movements and tectonic processes are to be addressed by the GLRS instrument. Depending upon the state of technology, the LASA instrument and the GLRS instrument can be used to meet the following measurement objectives that are responsive to the major thrusts of Eos.

LASA INSTRUMENT MEASUREMENT OBJECTIVES

Global Hydrological Cycle

- Measure the total column content of water vapor with a horizontal spatial scale on the order of 1 km and an accuracy of ±10 percent.
- Measure the vertical profiles of atmospheric water vapor from the stratosphere, through the troposphere, to the ground with a vertical resolution of 1 km and with an accuracy better than 10 percent at night and 15 percent during the day.

Aerosols and Clouds

- Measure cloud-top heights to a resolution of ±50 m and also measure cloud-top parameters. Measure the height of the planetary boundary layer with a resolution of 50 m and the heights of volcanic aerosol layers with a resolution of 1 km. Measure the vertical profiles of atmospheric aerosols over an altitude range from the ground to 30 km, with a resolution from 50 m to 2 km, and an accuracy of 15 percent.

Atmospheric-State Parameters and Ozone

- Measure the surface pressure with an accuracy of ±2 mb.
- Measure the vertical profiles of temperature and pressure from the stratosphere, through the troposphere, to the ground. Measure temperatures with an accuracy better than 1 K and with a vertical resolution of 1.25 km in the lower troposphere, 2.5 km or better in the mid-troposphere and upper troposphere, and 3 km in the lower stratosphere. Measure vertical profiles of pressure in the troposphere with an accuracy better than 0.4 percent (i.e., approximately 2 mb at 5 km) with a vertical resolution of 1 km.
- Measure the total column content of ozone with an accuracy of 1 to 2 percent.
- Measure the vertical profiles of ozone, especially in the region below the stratospheric peak to the ground, with a vertical resolution better than 2 km, and an accuracy better than 1 percent nighttime and 10 percent daytime.

GLRS INSTRUMENT MEASUREMENT OBJECTIVES

Ice-Sheet Mass Balance and Land Topography

- Measure ice and terrain topography to better than 10 cm vertical resolution and 300 m horizontal separation with a 70 m footprint.

- Measure the surface roughness and surface height distribution, at centimeter scales, of bare terrain, sea ice, and surfaces covered by vegetation, by analysis of the range distribution within a laser footprint.
- Measure topographical profiles of selected terrain to characterize volcanic, erosional, catastrophic geomorphic and subsurface processes.

Crustal Movements and Tectonic Processes

- Measure three-dimensional regional scale (25 to 500 km) crustal movements to a precision of 1 cm in seismically active zones using dense networks of retroreflectors.
- Measure regional scale (100 to 1,000 km) tectonic plate movements and intraplate rigidity using more broadly distributed retroreflectors.

INSTRUMENT CAPABILITIES

LASA sounding experiments from space will provide direct measurements of atmospheric properties. Profiles of tropospheric and lower-stratospheric water vapor and profiles of ozone, pressure, and temperature can be obtained with 1 to 2 km vertical resolution in keeping with the science objectives.

In altimetry, the unique collimation ability of laser pulsed radiation provides a small footprint (approximately 100 m) on the Earth's surface. The resulting high-resolution time-of-flight data are unique, and can resolve the important scales of ice-sheet elevation profiles, sea ice structure and distribution, and micro-roughness of terrain.

The retroranging experiments can provide a unique set of high-density, quasi-simultaneous crustal movement measurements. In a seismically active zone, ranging measurements will determine the intersite distances along a strike of a major fault to accuracies on the order of 1 cm. A more globally distributed network of cube-corner reflectors will be used to develop a set of tectonic plate movement and plate internal deformation measurements. Retroreflectors placed on the surfaces of ice sheets and smaller glaciers will provide similar data for studies of ice dynamics.

HERITAGE

Significant lidar investigations have been performed from both aircraft and space platforms. Lidar measurements have already been made from the NASA ER-2 aircraft, and an experiment is planned to measure the vertical distribution of lower-tropospheric water vapor from the NASA ER-2 aircraft in 1988. In addition, a technology development flight with lidar to measure vertical profiles of aerosols and cloud-top heights with a multi-wavelength lidar system is planned for a 1990-91 Shuttle flight. Space-based altimetry measurements with a solid-state laser were demonstrated on several Apollo missions in the 1970s. The Apollo Lunar Laser Altimeter returned very useful data sets on lunar topography and demonstrated the viability of space-based lidar systems.

TECHNOLOGY REQUIREMENTS

The LASA Panel recognizes that laser technology is rapidly evolving in response to NASA and other national needs. In particular, the development of tunable solid-state laser materials is progressing rapidly in that portion of the optical spectrum that covers experiments proposed in this report. Additionally, semiconductor lasers arranged in arrays are rapidly developing as replacements for conventional flashlamp pumping, with potential improvements of an order of magnitude in laser power, efficiency, and operating lifetimes. Flashlamp lifetimes are also constantly being improved. Gas laser technology in both excimers and carbon dioxide is being developed for long-lifetime space applications. Improvements in any one or all of these technologies before 1990 will substantially improve the Eos lidar capability to perform both daytime and nighttime measurements with full duty cycles.

Although there are limitations on lidar performance in space based on present technology, the Panel has assumed, for the most part, that the required laser technology will be available in the Eos time frame. The Panel did recognize that some experiments may be constrained to limited duty cycles and to nighttime operation for the earlier Eos experiments. These constraints are dictated by limitations in average power available and the relatively long instrument servicing intervals.

SYNERGISTIC SCIENCE

Spaceborne lidar instruments will provide observations whose characteristics include high spatial resolution with limited coverage. The coverage limitations follow primarily from the limitations in laser efficiency and available power, and secondarily from the limitations in laser system lifetime. These characteristics of lidar systems make their observations ideal for studies which synergistically use other Eos observations. An example of the synergistic use of the LASA data would be the combination of LASA-determined vertical profiles of water vapor together with two-dimensional depictions of water vapor

distributions from an Eos scanning microwave radiometer. In this example, the LASA instrument would give high vertical resolution profiles of water vapor at nadir with a horizontal spacing of approximately 1 km along the sub-satellite track. The microwave instrument would provide observations from which can be derived water vapor distributions with low vertical and horizontal resolution but broad spatial coverage.

The lidar altimetry data sets are highly synergistic with data products from radar altimeters and imaging radar instruments. This is true for ice, terrain, and ocean surface targets where the small footprint of the laser can be used to calibrate radar data and provide a high-resolution (vertical and horizontal) nadir track.

CONCLUSION

Eos will provide an ideal forum in which the strongly synergistic characteristics of the lidar systems can be used in concert with the characteristics of a number of other sensors to better understand the Earth as a system. Progress in the development of more efficient and long-lasting laser systems will insure their availability in the Eos timeframe. The necessary remote-sensing techniques are being developed to convert the LASA observations into the proper scientific parameters. Each of these activities reinforces the promise that LASA and GLRS will be a reality in the Eos era.

CONTENTS

	Page
PREFACE	iv
EXECUTIVE SUMMARY	v
Science Objectives	vi
LASA Instrument Measurement Objectives	vi
GLRS Instrument Measurement Objectives	vi
Instrument Capabilities	vii
Heritage	vii
Technology Requirements	vii
Synergistic Science	vii
Conclusion	viii
ACRONYMS	x
I. INTRODUCTION	1
Earth Observing System: Concept and Overview	1
LASA Science Issues	1
Atmospheric Structure and Composition	1
Surface Ranging	4
II. LASA SCIENCE: ATMOSPHERIC SOUNDING	8
Lidar Techniques	8
Cloud Observations	9
Planetary Boundary Layer Observations	11
Tropospheric Aerosol Observations	13
Stratospheric Aerosol Observations	15
Water Vapor Observations	19
Atmospheric Pressure Observations	28
Atmospheric Temperature Profile Observations	31
Ozone Observations	33
Lidar Scanning	37
Synergistic Science	39
III. LASA SCIENCE: ICE-SHEET DYNAMICS AND SURFACE ALTIMETRY	41
Lidar Altimetry Applications	41
Measurement Objectives	41
Synergistic Science	42
Altimeter Instrument Description	42
Measurement Simulations	42
Examples of Laser-Altimeter Data	49
IV. LASA SCIENCE: GEODYNAMICS AND LASER-RANGING APPLICATIONS	54
Introduction	54
Measurement Objectives and Strategy	56
Demonstration Experiments and Performance Simulations	62
Synergistic Science	67
V. HERITAGE, CONCEPTS, AND LASER TECHNOLOGY ASSESSMENT	70
Lidar Heritage	70
Instrument Concepts	71
Laser Technology Assessment for Atmospheric Measurements	73
Laser Technology Assessment for Surface-Ranging Measurements	78
Comparison of LASA Objectives with Laser Capabilities	79
VI. Eos COMMAND AND DATA MANAGEMENT SYSTEMS FOR LASA	83
Data Rates	83
Command Uplinking and Control	83
System Redundancy	84
Ground Computer Facilities	84
VII. CONCLUSIONS AND RECOMMENDATIONS	85
APPENDIX A: EYE SAFETY ISSUES	87
REFERENCES	88

ACRONYMS

AFGL	Air Force Geophysics Laboratory
ANSI	American National Standards Institute
AOL	Airborne Oceanographic Lidar
APD	Avalanche Photodiode
BRDF	Bidirectional Reflectance Distribution Function
BUV	Backscattered Ultraviolet
CLS	Cloud Lidar System
cw	Continuous Wave
DARPA	Defense Advanced Research Projects Agency
DC	Direct Current
DIAL	Differential Absorption Lidar
DIALEX	Differential Absorption Lidar Experiment
FHST	Fixed-Head Star Trackers
FOV	Field-of-View
FWHM	Full-Width Half-Maximum
GCM	General Circulation Model
GEM	Goddard Earth Model (of Gravity)
GEOS II	Geodynamic Satellite II
GLRS	Geodynamics Laser-Ranging System
GMT	Greenwich Mean Time
GPS	Global Positioning System
GRM	Geopotential Research Mission
GSFC	Goddard Space Flight Center
HMMR	High-Resolution Multifrequency Microwave Radiometer
IOC	Initial Orbiting Configuration
IRU	Inertial Reference Unit
LAGEOS	Laser Geodynamics Satellite
LASA	Lidar Atmospheric Sounder and Altimeter
LASE	Lidar Atmospheric Sensing Experiment
Lidar	Light Detection and Ranging
LITE	Lidar In-Space Technology Experiment
MACS	Modular Attitude Control System
MCP/PMT	Microchannel Plate/Photomultiplier Tube
MMS	Modular Mission Spacecraft
MODIS	Moderate-Resolution Imaging Spectrometer
MPE	Maximum Permitted Exposure
NEE	Noise Equivalent Energy
NEP	Noise Equivalent Power
OAST	Office of Aeronautics and Space Technology
OMC	Observed Minus Calculated
OPO	Optical Parametric Oscillator

ACRONYMS (continued)

PBL	Planetary Boundary Layer
PSC	Polar Stratospheric Cloud
RF	Radio Frequency
rms	Root Mean Square
SAGE	Stratospheric Aerosol and Gas Experiment
SAM II	Stratospheric Aerosol Measurement II
SBUV	Solar Backscatter Ultraviolet
SLR	Satellite Laser Ranging
SMRWG	Science and Mission Requirement Working Group
SNR	Signal-to-Noise Ratio
SPE	Signal Photoelectron
STP	Standard Temperature and Pressure
TFE	Tropopause Fold Event
TOMS	Total Ozone Mapping Spectrometer
UV	Ultraviolet
VLBI	Very Long Baseline Interferometry

I. INTRODUCTION

EARTH OBSERVING SYSTEM: CONCEPT AND OVERVIEW

Through the centuries, vast amounts of data and much phenomenological knowledge about the Earth have been accumulated through ground, airborne, and space observations. However, to acquire systematic, synoptic, and temporal knowledge of our planet, and an understanding of the mechanisms underlying the global processes that affect it, requires a multidisciplinary approach with long-term observations from space. The key to progress in Earth science for the next decade will be to address those multidisciplinary questions that concern the integrated functioning of the Earth as a system. The fundamental processes that govern and integrate this system include the global hydrological cycle, the biogeochemical cycles, climate processes, and geologic activities. A plan to address the integration of these cycles and processes has been developed and reported in Earth Observing System (Eos) (Butler *et al.*, 1984).

In order to address the multidisciplinary challenges confronting Earth science, observational capabilities must be employed that range in scale from detailed *in situ* and laboratory measurements to the global perspective offered by satellite-based remote sensing. Eos will use polar-orbiting space platforms to provide this global perspective. It is, of course, recognized that information obtained from space must be used in concert with information obtained from conventional observations.

The understanding of the global integrated functioning of Earth will require, in addition to integrated observation systems, a data system to ensure that information from all systems will be extensively exploited. The integration of ground-based, airborne, and spaceborne measurements to obtain quasi-instantaneous coverage (on the order of 2 days) with broad areal, almost global extent, is the motivation for creating Eos. This new entity, Eos, will enable a comprehensive multidisciplinary approach to understanding Earth as a system.

Eos is envisioned as a user-friendly information-gathering system with near-global coverage, augmenting to the maximum extent, existing operational systems. The implementation strategy for Eos is to maintain the ongoing time series of Earth science data, to broaden the measurement basis commensurate with technology achievements, and to demonstrate new and more powerful instrument capabilities. Through this evolutionary process, Eos will eventually serve all Earth science communities.

LASA SCIENCE ISSUES

The recommendations of the Lidar Atmospheric Sounder and Altimeter (LASA) Panel discussed in this report are directed toward a series of atmospheric composition and structure measurements, as well as a set of surface-ranging measurements. The LASA instrument concept incorporates two separable remote-sensing techniques. Sensing of atmospheric properties is the primary role of the LASA instrument proper whereas measurement of Earth surface features is the role of a separately designated instrument identified as the Geodynamics Laser-Ranging System (GLRS). The LASA instrument can function as an altimeter with somewhat limited vertical resolution as compared to GLRS, which has the potential of achieving 10 cm resolution. Accordingly, the material that follows separates into two parts: atmospheric composition and structure, and surface-ranging measurements.

The LASA instrument may operate in the ultraviolet, visible, and infrared range of the electromagnetic spectrum, and provides vertical profiles of water vapor, aerosols, clouds, ozone, and other atmospheric gases. Temperature and pressure profiles may also be determined as can locations of atmospheric discontinuities such as the top of the planetary boundary layer (PBL) and the tropopause. In addition, aerosol distributions can be used as tracers of atmospheric motions, and, using the Doppler technique, a direct measurement of winds is possible (see the report of the Panel on Lidar Atmospheric Wind Sounder). Laser altimetry will be used to observe the accumulation of ice and snow on the Greenland and Antarctic ice sheets and to measure the topography of the Earth's surface. GLRS will perform high-accuracy distance measurements over a wide range of terrestrial baselines and, by ranging off retroreflectors, observe both relative motion and internal deformation of the Earth's lithospheric plates. Similarly, GLRS will also be used to study local scale crustal movements.

ATMOSPHERIC STRUCTURE AND COMPOSITION

There are many features of the atmosphere, both structure and composition, that need elucidation. These features include the distribution of moisture as water vapor and as cloud droplets, characteristics of the PBL, variations in temperature and pressure, the distribution and nature of atmospheric aerosols, and the distribution of atmospheric ozone. All of these features can be studied by remote sensing using spaceborne lidars.

Water Vapor

The transfer of water between its three phases, solid, liquid, and vapor, among the land, oceanic, and atmospheric reservoirs is important in energy transport around the Earth. The movement of water between the oceans, the marine and terrestrial atmosphere, the land, the subsurface reservoirs, etc., constitutes the global hydrological cycle. The mechanisms of the atmospheric circulation are strongly coupled to the components of this hydrological cycle. Because of the distinct features of the global circulation, the spatial distribution of water is highly variable over the globe. The hydrological cycle plays an important role in atmospheric chemistry, in weather and climate, and in the Earth radiation budget.

Water vapor is an important mechanism for the transport of energy in the form of latent heat, primarily from tropical regions poleward. This latent heat is converted into sensible heat upon recondensation, primarily in the regions of mid-latitude cyclones. Latent heat release is the primary energy source for tropical cyclones. Thus, the vapor phase latent heat represents a large source of potential energy, and therefore, the water vapor distribution is key to global dynamics and circulation.

Water vapor is of prime importance in the transfer of infrared radiation. Since water vapor is a highly variable atmospheric constituent that is highly infrared-active, its effect on radiation transfer is significant, both spatially and temporally. A long-term increase of water vapor, with its accompanying effects on infrared radiation transfer, could result in greatly enhancing the predicted long-term effects on climate from increasing carbon dioxide in the atmosphere.

To date, measurements of water vapor have been primarily made from ground-based radiosonde stations and have generally been limited to populated land areas. Most of the precipitable water vapor is contained in the first one kilometer above the Earth's surface. To reasonably characterize this portion of the hydrological cycle, observations of the vertical profile of water vapor must be made with a resolution of 1 km or better for this part of the atmosphere. Huge gaps exist in data bases over oceanic and other inaccessible areas. Further, standard measurement techniques have been limited to the lower and mid-troposphere due to difficulties in determining the small amounts of water vapor in the upper troposphere and the stratosphere. In the stratosphere, the data base is extremely sparse.

Planetary Boundary Layer

The planetary boundary layer (PBL) determines near-surface fluxes of heat, moisture, particles, and trace gases. The PBL is that portion of the lower troposphere that marks the top of the convective activity near the Earth's surface. It is normally about 1 km thick and capped by a temperature inversion. As a result, exchange of atmospheric properties, such as heat, moisture, particles, and trace gases between the region above the PBL and the free troposphere, is greatly inhibited. The flux of heat and moisture from the Earth's surface to the lower atmosphere is largely governed by the intensity of convection within the PBL, as well as the thickness of this layer. Under conditions of deep convection, the PBL may extend through the entire troposphere up to the tropopause. For the most part, detection of the PBL is accomplished from analysis of upper-air radiosonde soundings, and has been confined to data points at standard radiosonde stations. This leaves large gaps in the data base and an incomplete description of the global PBL. To significantly improve our understanding of the PBL and its interaction with the surface and the free troposphere, measurements of PBL height are needed with a resolution of approximately 0.1 km.

Clouds

It is well known that many cumulus-type clouds under highly unstable atmospheric conditions actually penetrate the tropopause and reach into the lower stratosphere. The role of these clouds in the budget of stratospheric water vapor is presently unknown. It may be that these clouds represent a source of stratospheric water vapor from the troposphere through the tropopause. The existence of subvisible cirrus clouds has been known for some time. Their presence has been detected by aircraft and satellite observations and by inference from certain atmospheric optical effects. Little is known of their frequency of occurrence, their spatial distribution, and the physical and optical properties from which one could assess their importance on the radiation budget.

Pressure and Temperature

Pressure and temperature are basic to the inference of atmospheric properties from many passive remote sounders, and are crucial for interpretation of all atmospheric processes. While reasonably good data coverage exists over land masses in the northern hemisphere, the data bases over oceanic areas, and much of the land areas of the southern hemisphere, are very poor. Increased data coverage for these two variables is needed at a higher vertical resolution than the 2 to 4 km presently available.

Aerosols

Aerosols affect atmospheric radiative transfer processes, clouds, and chemistry. The recent El Chichon eruption inspired several studies on the subject

of volcanic aerosols in the atmosphere. These studies indicated that, in the lower troposphere, temperature decreases on the order of 2 K could result from intense volcanic activity. Considerably larger stratospheric changes in temperature were predicted, and evidence of these effects in tropical regions was observed. Determination of the distribution and optical densities of volcanic aerosol layers is important. With the exception of data from lidar and from solar photometers, our global knowledge of these layers depends on existing satellite observations such as those from the Stratospheric Aerosol Measurement II (SAM II) and Stratospheric Aerosol and Gas Experiment (SAGE) missions. Some data are available on tropospheric aerosols from conventional balloonsonde data, but the data base is inadequate.

Ozone

The global ozone distribution needs further study, particularly to establish possible trends in total ozone concentrations. There is continuing concern for the possibility of ozone destruction in the stratosphere due to the release of chlorofluorocarbons and a satellite- and ground-based data base on ozone distribution is being developed. In the troposphere, ozone is thought to have increased in recent years because of increases in methane and other gases. In order to detect early indications of a trend in either the stratosphere or troposphere, a more detailed measurement base is required.

Lidar Contributions Complementary to Passive Remote Sensing

The experiments proposed for the LASA observations of atmospheric structure and composition provide many avenues of interaction with remote-sensing experiments, with either currently operational or proposed Eos instruments. These interactions may be one or more of the following types:

1. The LASA-measured data will in many instances provide a completely independent data set from that determined by other experimental techniques, thus allowing for a cross-check of results.
2. The LASA-measured data can be used as input data for other experiments to assist in the data analysis.
3. The LASA-measured data will provide initial solution estimates for other experiments requiring mathematical inversion solutions.

Considering (1) above, the LASA experiments provide direct sounding information on atmospheric parameters, in contrast to passive techniques used in other experimental packages. Furthermore, the data analysis techniques employed in the LASA experiments involve direct data reduction, in contrast to inversion techniques required by passive experiments. Examples include proposed experiments to determine vertical profiles of water vapor, temperature, and ozone. The current techniques for inferring these profiles use passive instruments, requiring inversions of the data to recover the profiles. The active technique proposed in the LASA package will provide independent data and direct profile recovery. Lidar and Differential Absorption Lidar (DIAL) will present independent profiles for comparison with passive sounders. In addition, LASA will provide, in most cases, considerably higher vertical resolution than those techniques requiring inversions. For instance, features such as cloud-top altitudes and PBL heights can be resolved to approximately 0.1 km or better. Water vapor profiles can be determined using the DIAL approach to a vertical resolution of approximately 1 km.

Considering (2) above, the LASA data will be of considerable use in improving the data analysis from other experiments. For example, the tropospheric and stratospheric aerosol data obtained by lidar will be invaluable in removing aerosol effects from surface imagery and albedo measurements. As was the case after the eruption of El Chichon, artifacts due to the stratospheric aerosols produced by this eruption caused significant errors in the retrieval of sea-surface temperature and the concentrations of nitrogen dioxide, water vapor, and other gases obtained by existing satellite measurements. LASA measurements of the PBL, when combined with passive microwave measurements, will provide better information on the vertical distribution of water vapor. LASA measurements of cloud properties and heights, particularly for optically thin clouds, will assist in most passive measurements of atmospheric parameters, and will be a substantial aid in refining cloud-top heights determined by infrared passive sounders. LASA tropopause heights will be a great aid in infrared and microwave inversion techniques for determining temperature profiles.

Most profiles determined by lidar and DIAL could be used as initialization information ("initial estimates") for experiments that fall into category (3). Examples would be the water vapor, temperature, and ozone profiles obtained through lidar, and also obtained by inversion of passive measurements. The lidar profiles could be used to provide "initial guess" profiles for the inversion algorithms used by the passive techniques. Aerosol profiles from LASA will also be used to complement the passive aerosol measurements from the SAM II and SAGE instruments.

Lidar Technology Considerations

The LASA capabilities can be divided into two broad categories that are distinguished by the degree of technological difficulty anticipated in developing the instrumentation. These categories are: (1) existing technology with engineering improvements, and (2) future technology requiring continued research efforts.

Lidar measurement capabilities using existing technology (only engineering improvements required) include:

- water vapor column content
- boundary layer height
- relative aerosol profiles
- cloud-top heights
- optical depth of clouds

With anticipated technology developments, the following measurements may become operational within the Eos era:

- water vapor profile (lower troposphere)
- surface pressure and pressure-altitude profiles
- surface temperature and temperature-altitude profiles
- total aerosol optical thickness
- total ozone column content
- ozone profiles

SURFACE RANGING

Lidar is an ideal tool for very accurate measurement of distance. Laser ranging, either directly to the Earth's surface or to retroreflectors on the surface, can be used to accurately determine geometric positions. A particularly interesting application of satellite-borne laser surface altimetry is in its use in understanding ice-sheet dynamics and variability. The most notable application of satellite laser retroranging is in improved understanding of geodynamical processes. These applications are described in the two sections which follow.

Ice-Sheet Dynamics and Variability

At present, it is not known whether the existing ice sheets of Greenland and Antarctica are growing or shrinking. There are mounting concerns that future changes of climate may disturb the equilibrium of polar ice masses and hence global sea levels (Polar Research Board, 1984a, 1984b). Present estimates of mass balance, which are based on estimates of the mass input (accumulation rate) and mass output (ablation, bottom melting, and iceberg discharge), are probably only accurate to ±50 percent. An uncertainty in ice-sheet mass balance of ±50 percent corresponds to a sea-level change of 3 cm/decade or an average ice elevation change of 100 cm/decade. Results from the few areas that have been studied in detail by surface measurements indicate that either thickening or thinning of the local ice is the rule rather than the exception. Steady state appears to be rare. It is also not known whether the ice flow is inherently stable or subject to accelerated flow. Further, knowledge of how the ice sheets respond to climate change is rudimentary (Thomas *et al.*, 1979; Polar Research Board, 1984b).

The boundaries of ice sheets and adjacent floating ice shelves are influenced by the seasonal cycle of temperature, radiation, precipitation, and ablation, as well as longer-term variations of atmosphere, ocean, and solar insolation. Two important parameters that can be uniquely observed by satellite for the study of the long-term behavior of ice sheets and ice shelves are changes in surface elevation and changes in the position of ice-shelf fronts. Other key parameters observable by satellite include iceberg discharge, ice velocities, extent and duration of summer melting, and possibly accumulation rates. Ice thickness has been surveyed by airborne radar sounders, and ongoing field projects will continue to provide detailed regional measurements of ice flow, internal characteristics, and ice bedrock interactions. Most of the ice parameters of interest for the study of ice dynamics should be averaged over at least 1 year, consistent with the slow response of glaciers to changes in boundary conditions. One exception is the extent and duration of surface melting in summer, which requires daily observations by passive microwave sensing for studies of interannual variations.

Repetitive, precise measurement of ice-surface elevation by satellite altimetry (Zwally *et al.*, 1981) has been recognized in recent years to be the only means of determining changes in ice volume, which is equivalent to determining the net mass balance. In addition, detailed repetitive profiling of the surface slope, which determines the driving force for the ice flow toward the sea, will provide information on the time-dependent behavior of the ice flow. This has been exceptionally difficult to obtain by conventional measurements. Therefore, repeated elevation surveys by satellite altimetry will provide a direct measure of the volume change and overall mass balance, as well as the redistribution of mass within the ice sheets.

Several recent reports support, in principle, the approach described in this report for studying ice-sheet dynamics and variability. They include: The Polar Regions and Climatic Change (Polar Research Board, 1984b), Research Emphases for the U.S. Antarctic Program (Polar Research Board, 1983), and Environment of West Antarctica: Potential Carbon Dioxide-Induced Changes (Polar Research Board, 1984a).

The required accuracy for satellite measurement of elevation changes is estimated by looking at the probable magnitude of thickening or thinning rates that might be observed and the significance of these changes in terms of changes in ice volume and sea level. The mass input per year averaged over the whole of Greenland and Antarctica is about 20 cm of ice per year, which is about one part in 10^4 of the total ice volume (average thickness is about 2,000 m). The ratio of average elevation change to sea-level change is about 30:1 (2,000 m thickness divided by sea level equivalent of 70 m). Therefore, a 50 percent mass imbalance would produce an average ice elevation change of 10 cm/year and a sea-level change of about 0.3 cm/year, a figure somewhat larger than estimates of current rise in sea level.

The accumulation rate is not uniform over the ice sheets; in central regions, accumulation rates are about 2 to 5 cm/year. Therefore, in those regions, a 50 percent mass imbalance represents only a 1 to 2 cm/year elevation change. To permit detection of this change over a 5- to 10-year period requires a relative measurement accuracy of about ± 10 cm and averaging of multiple measurements over approximately 10^4 km^2 areas. The spacing of profiles should be less than 5 km and the spacing of height measurements along each profile track should be about 300 m to provide the density of coverage for detection of elevation changes without biases or aliasing due to ice-surface undulations (predominant wavelengths are about 5 to 10 km). The satellite orbit must also reach at least 81° latitude, with 87° most desirable, to cover most of the Antarctic ice sheet and provide overlapping measurements for calibration, referencing of successive orbits, and validation of precision. The anticipated Eos orbit of 98.2° will be ideally suited for this application. In operation, the altimeter will measure the elevation of the snow surface, beneath which there is a gradual transition to solid ice over a depth of 50 to 100 m. To translate changes in surface elevation to changes in ice-column mass, it is assumed that the depth of the snow-to-ice transition and the elevation of the bedrock topography are invariant during the period of measurement.

Ice-sheet topography has already been successfully mapped using a satellite radar altimeter (Brooks *et al.*, 1978; Thomas *et al.*, 1983). Because the accuracy of radar altimetry is limited by the rather large footprint of the radar beam (20 km diameter), changes within the resolving power of the radar would take decades to be detected. A satellite laser altimeter system with a range precision of ± 10 cm and footprint diameter of 70 m has been designed (Bufton *et al.*, 1982). Accurate repetitive mapping of the seaward boundary of the floating ice shelves has also been accomplished with radar altimetry (Thomas *et al.*, 1983). Other studies have shown the feasibility of measuring accumulation rates and summer melt zones with passive microwave images (Zwally, 1984). Ice-surface velocities can be measured by laser retroranging to reflectors placed on the ice sheets for studies of glacier dynamics. Measurements by altimetry, laser ranging, and passive and active microwave imaging on Eos are all complementary and will provide unique data for studying ice-sheet dynamics and variability.

The immediate science goals and objectives for ice-sheet dynamics and variability studies can be summarized as follows:

- determination of ice-sheet mass balance
- studies of ice dynamics
- investigation of stability/surging/flow changes

Geodynamics

Over the past 2 decades remarkable progress has been made in understanding geodynamic processes through the use of space techniques. High-accuracy determinations of satellite orbits by laser-tracking systems have been used to develop detailed representations of the Earth's gravity field. Variations in the height of the gravity equipotential surface (geoid) have been used to determine the mechanical strength of the crust and provide insight into the dynamics of tectonic plate motion. Insight into the processes responsible for mountain building and convection within the mantle has been developed by the synergistic merger of space and ground gravity and geodetic data with seismic, geological, and thermal information. Determination of whole-Earth tides, of polar motion, and variations in the length of day have all benefited from centimeter-accuracy laser tracking of satellites. Most importantly, laser tracking of satellites has permitted the determination of distances between sites to centimeter accuracies. Centimeter-level changes in baseline lengths for distances from a few tens of kilometers to several thousand kilometers are being used to monitor the motion of tectonic plates and to study crustal deformations. In addition, measurements of regional-scale crustal movements are providing important data for modeling strain accumulation in regions of past and future large earthquakes. Indeed, within the last few decades, the study of crustal dynamic processes has occupied one of the most prominent places within solid-Earth geophysics research. The theory of plate tectonics, in which the mechanically strong layers of the crust and uppermost mantle are fractured into a limited number of moving, relatively rigid units (lithospheric or tectonic plates), has provided a unifying geodynamic theory. Plate tectonics explains the geography of continents and oceans, the occurrence of earthquakes, volcanoes, and mountains, and the distribution and evolution of various rock types and geologic features. Tectonic plates move relative to one another at velocities of several centimeters per

year. The resistance to this motion at the contact points between plates causes stress to accumulate, which may subsequently be relieved by earthquakes.

Although tectonic plates are regarded as being relatively rigid within the context of first-order tectonic plate theory, significant internal deformations may occur. Strain related to stress accumulation on faults is important both at the boundaries between major plates and within certain plate interiors. Over geologically significant time spans, new tectonic plate boundaries are created and destroyed by plate rifting and suturing. The tectonic processes produce vertical as well as horizontal motions. Compressional folding and/or fault-related block uplift are two phenomena involved in mountain development within most major chains.

Tectonic plate motions, regional crustal deformations, fault-related strain accumulation, and other tectonic processes produce crustal movements of up to several centimeters per year. The fundamental scientific issues are to determine the contemporary rates for these motions, determine their spatial and temporal variations, and to develop models that explain these phenomena in terms of basic physical processes occurring in the solid Earth. The data required to carry out this task are the high-accuracy determinations of the relative motion between various points on the Earth's surface separated by tens to thousands of kilometers. The data must be obtained with improved temporal and spatial resolution unobtainable from ground-based observations. A unique geodetic surveying capability is provided by laser ranging from an Eos platform to cube-corner reflectors on the ground via GLRS.

The basic experiment involves a time-of-flight measurement of the distance between Eos and the ground targets. These data are used to determine the positions of the survey sites. The motions are deduced by resurveying the network at a later date to observe changes in the target site locations. As discussed in later sections of this report, laser ranging from ground-based observatories to satellite reflectors has already provided significant information on crustal dynamic properties. In the Eos concept, the sophisticated laser-ranging and optical-tracking equipment would be located on the satellite. This would permit orders-of-magnitude-greater density of sites than is possible with current techniques at selected locales throughout the world. In combination with the ground-based systems, this system would provide a truly global, centimeter-accuracy, geodetic network.

Thus, the operation of a laser-ranging instrument from an Eos platform to ground-based retroreflectors permits dramatic improvements in the temporal and spatial resolution with which geodynamic processes can be studied. The measurements would expand current capabilities to measure tectonic plate motion and provide unique opportunities to search for time variations in the plate velocities. Such a system could also provide a capability to observe the precursory geodetic motions believed to occur before the onset of large earthquakes and, in a broad sense, provide significant information on the evolution of the Earth and other planets.

The retroreflectors can also be attached to ice sheets to monitor their horizontal and vertical movements and complement measurements relating to the ice-sheet dynamics discussed earlier in this report.

Height determinations may also be made by operating the laser-ranging system in an altimetric mode without cube-corner retroreflector targets. Terrain topographic data can be correlated with gravity observations to determine how the lithosphere flexes under mountain belts. Flexure properties are useful in understanding the mechanical state and evolution of the lithosphere. Additionally, mapping of surface slopes can provide important input to hydrologic studies of rain runoff, and detailed mapping of height distributions within selected physiographic provinces is useful in both geological and geophysical studies. Retroranging data can be used to refine the orbital ephemeris of the Eos platform to the centimeter level. Since a highly accurate prediction of the Eos platform position can be made with gravity field models for some period of time following retroranging, few centimeter-accuracy measurements of the marine geoid or height of the underlying terrain may be possible if the LASA retroreflector instrument (GLRS) is operated in the altimetry mode or in conjunction with the higher-power, large-aperture LASA altimeter. This would lead to a further improvement in our knowledge of the Earth's gravitational field and of the mechanisms of support and gravity compensation for topographic features.

Specifically, the spaceborne laser-ranging system would build up a data set for studying the following fundamental geodynamic questions:

- What are the spatial distributions in crustal movement near various seismic zones, and how do the patterns change with distance into the tectonic plate interiors?

In this regard, detailed information on the pattern of strain provides insight into the forces responsible for crustal movement and, in turn, insight into the mechanism for transfer of stress between plate boundaries and interiors. This information is useful in modeling the mechanical structural properties of the Earth as they vary from one region to another.

Simultaneous surveying of a grid of cube-corner retroreflectors separated by roughly 50 km in a network with dimensions of several hundred kilometers would provide insight into earthquake mechanisms. In combination with ground observations within a few tens of kilometers about a fault zone the data would provide insight into the failure mechanisms

associated with earthquake occurrences and how aftershocks occur, and would provide more detailed understanding of how an earthquake relieves and redistributes tectonic stress. The detection of precursory crustal movements offer the potential for aiding earthquake prediction.

- What are the patterns of internal crustal deformations within tectonic plate interiors?

In discussing this point, we note that although first-order tectonic plate theory regards the plates as rigid units, significant internal deformations exist in many locations. Studies of the patterns of crustal movements over baselines of several hundred kilometers in North America, places in Eurasia, and elsewhere would provide information on the contemporary rates of these internal deformations. These would be used in studies of the mechanisms responsible for intraplate deformation.

Altimetric measurements are important for tectonophysics studies over both continental and oceanic regions. Terrain profile data, for example, can be used in studies of the mechanisms of support for topographic features. Studies correlating topography and gravity are basic to understanding how the Earth's lithosphere bends or supports crustal loads associated with mountain belts, islands, etc. Such studies provide information on the thickness of the lithosphere and its strength, on the distribution of density of rock within the crust and upper mantle, and insight into the evolution of the crust. Over continental regions with significant topographic relief, measurements with a spatial resolution of a few hundred meters would provide a valuable data set for these studies. Measurement accuracy of a few meters is sufficient for geodynamic applications over land. Over oceans, an accuracy of about 1 cm is required for accurately mapping the ocean geoid and determining ocean circulation parameters.

The measurements with the GLRS instrument are complementary to those made with other techniques. The crustal movement measurements provide a densification of the existing network of ground-based laser and very long baseline interferometry (VLBI) sites. They would extend well beyond the capabilities of conventional local surveys, which are very labor-intensive and of limited utility in mountainous regions. The networks should be designed to complement rather than compete with those that will be surveyed with highly mobile receivers operating on microwave signals from the Global Positioning System (GPS) satellites. The altimetric measurements would provide high-resolution topographic mapping to complement the coarser but more global coverage available from microwave altimeters. Gravity and magnetic data available from current sources and the planned Geopotential Research Mission (GRM) satellite can be used in combination with these data to provide a more complete picture of the geodynamics of the Earth than could be inferred from either data set taken by itself.

II. LASA SCIENCE: ATMOSPHERIC SOUNDING

LIDAR TECHNIQUES

Lidar sounding is a remote-sensing technique to measure profiles of atmospheric backscatter from aerosols and molecules and extinction properties of the atmosphere with an active laser transmitter. The lidar signal return (power) from a range Z is given by:

$$P(Z) = \frac{EA\eta\beta cT}{2\,Z^2}$$

where E is the energy per pulse of the laser source, A is the collection area of the receiving telescope, η is the overall efficiency of the receiving system, β is the atmospheric volume backscattering coefficient, c is the speed of light, and T is the two-way atmospheric transmission from the transmitter to the range Z.

In the simplest form, a lidar system consists of three basic components: (1) the laser transmitter as a source of energy, (2) a suitable telescopic receiver to collect backscattered light, and (3) a detector system to produce an electrical signal proportional to the received power. In general, the transmitter and detector systems are collocated. The wavelength range of lidar operation is normally from 0.2 to 10 μm, with either pulsed or continuous operation of the laser transmitter.

Active laser sensors, such as lidar, offer the possibility of significantly enhanced vertical resolution compared with that typically achieved with passive sounders. Time gating of the detector signal permits a vertical resolution limited ultimately by the laser pulse length, detector sensitivity, and background sources of light. Since lidar provides its own light source, it can perform measurements under both daytime and nighttime conditions.

Lidar operates by detecting laser radiation transmitted through the atmosphere and backscattered from the atmosphere itself, or from surfaces such as clouds or the ground. Developments in laser atmospheric sounding have reached the point where there have been ground-based measurements (for the past 20 years) and aircraft-based measurements (for the past 10 years) of many important atmospheric properties, including clouds, aerosols, temperature, ozone, and water vapor distributions.

Because of the global coverage provided by the Eos platform, LASA can be utilized to investigate long-range transport of haze layers, aerosols, and several atmospheric species, tropospheric/stratospheric exchange processes, boundary layer properties, and free tropospheric conditions.

In the following sections, the science objectives and the experimental approaches associated with each lidar measurement technique are described. The techniques include those associated with backscatter lidar for measuring cloud-top heights, PBL, tropospheric and stratospheric aerosols, the DIAL techniques associated with the measurement of water vapor and ozone concentrations, and atmospheric pressure and temperature measurements. It is emphasized that each measurement category complements the other. For example, with the backscatter lidar technique, cloud-top heights, PBL, and tropospheric and stratospheric aerosol profiles can be measured simultaneously, and, with a pulsed DIAL system, these measurements can still be obtained but also profiles of gaseous species, temperature, and pressure can be obtained. In addition, the total column content of gaseous species can be determined.

Differential Absorption Lidar Technique

In general, the Differential Absorption Lidar (DIAL) technique depends on the existence of a spectral feature (absorption line) in the atmosphere that is specific to a gas molecule, and whose spectroscopic characteristics are well known (i.e., line intensity, line position, and line broadening as a function of temperature and pressure). The absorption line must be free of spectroscopic interference from other molecules. In order to detect the molecular feature, the wavelength of the laser is tuned to overlap the absorption feature, preferably at the center of the line. A second laser wavelength is required, whose wavelength is shifted away from the molecular feature far enough to minimize molecular absorption, but sufficiently close so that the scattering properties of the atmosphere are virtually identical at the two wavelengths. The two laser wavelengths are pulsed and can be fired within a time spacing that is short compared to the time scale of atmospheric dynamics, i.e., <100 μs. The two laser pulses are backscattered to the receiver telescope by atmospheric aerosols and molecules, so that the return signals represent a time history of the scattering and absorption properties of the atmosphere for each laser-pulse pair. This time history is related to a spatial profile of these properties through the equation $(c\Delta t)/2 = \Delta R$, where Δt represents a time interval that is selected to correspond to a specific range interval, ΔR. The ratio of the return signal P_{on}, at the 'on' wavelength to the return signal, P_{off}, at the 'off' wavelength is measured. Through the lidar equation, this ratio can be related to the molecular concentration of the gas in the atmosphere as a function of distance from the transmitter. Another useful mode for a DIAL experiment is to measure column content by employing a pulsed or continuous wave (cw) laser and using reflection from the ground (or from layers such as clouds) to return

the two laser wavelengths to the receiving telescope. In the infrared, pressure broadening of atmospheric spectral lines as a function of altitude is large relative to the ultraviolet (UV) and visible portion of the spectrum. In this wavelength region one can selectively probe various segments of the absorption line by tuning the wavelength of the continuously transmitting laser from the central peak into the wings of the absorption line to determine the vertical layering of the selected molecule. Conceptually, this is similar to passive solar-reflection techniques. In the case of DIAL, however, the source of radiation is monochromatic, allowing a single absorption line to be probed.

Generically, lidar (including DIAL) measurements from space have three distinct advantages: (1) the capability to probe the troposphere between the clouds with minimal signal loss from low-level clouds and haze layers, (2) increasing signal strength with range from the top of the atmosphere down, due to the exponentially increasing atmospheric scattering, and (3) high horizontal spatial resolution with very good vertical resolution when used in the pulsed mode.

CLOUD OBSERVATIONS

Clouds are critical to the flow of energy and the cycling of water and trace species through the atmosphere. The climatic effects of changes in cloud cover are not well understood.

Cloud cover reduces solar input to the surface of the Earth through reflection of solar radiation, but cloud cover also reduces the infrared output from the surface, which is an opposing process. The net radiant flux change is a function of the density and temperature, or height, of the cloud. For cirrus, frontal clouds, or high cumulonimbus, the infrared process may dominate. Only direct observations, which include lidar height measurements, are likely to adequately resolve the actual radiative effects of these clouds.

A principal limitation to current understanding and modeling of the physical climate system is the inability to correctly account for the role of clouds. Better predictive cloud models are required for studies such as the influence of anthropogenic carbon dioxide on climate. Improved cloud climatologies are possible from a thorough study of the current satellite data base. However, existing observations from passive sensors do not adequately describe all cloud characteristics. The important cloud-height measurement is only a roughly inferred quantity, and optically thin clouds are poorly resolved. Future improvements can come from active sensors such as lidar. The fundamental measurement objective for LASA in cloud studies is to unambiguously describe the vertical structure of the cloud field. Passive techniques such as infrared imagery are inadequate for cirrus clouds where the emissivity is very much less than one. Even more advanced methods, such as carbon dioxide slicing, can obtain height resolutions to no better than several kilometers.

In addition to the cirrus problem discussed above, there are other direct applications that may be mentioned. The persistence and height of marine stratus are readily obtained from lidar measurements. Additional applications involving advanced analysis of lidar returns for cloud microphysics are possible. These would be important for cloud radiation parameterization.

Measurement Approach

For clouds, the basic lidar measurement approach will be to obtain vertical lidar backscattering profiles at a single wavelength. In addition, the polarization characteristics of the lidar pulse can be used to determine the thermodynamic phase of hydrometeors in the clouds. The transmitted laser pulse will be polarized. The polarization state of the backscattered signal will depend on the scattering properties of the medium. Precision backscatter measurements require detection of the complete polarization state. At a minimum, the polarization, parallel and perpendicular to the polarization of the transmitted pulse, must be detected. From these measurements the degree of polarization or depolarization, can be inferred. The latter quantity, depolarization, can be used to determine the presence of ice and/or liquid particles in the cloud.

Since clouds are highly inhomogeneous, the vertical structure information should be obtained with useful accuracy from single laser pulses at horizontal resolutions of less than 1 km. The most basic and easily obtained observation for clouds is the height of the cloud top. The existence of multiple cloud layers may be determined from lidar return profiles under certain conditions.

In addition to cloud-top height, a number of other significant cloud parameters are derivable from the lidar signal return. The backscatter signal from clouds is a function of the single scattering backscatter coefficient within the cloud, the attenuation above and within the cloud, and any addition to the signal from multiple scattering (Sassen, 1980; Spinhirne *et al.*, 1983). For dense clouds such as stratus, strong signal returns are received from the cloud top, but the signal is attenuated at fractional distances into the cloud and multiple scattering is significant. The parameters which may be obtained for stratus clouds are the cloud-top scattering coefficients and an inference of the water/ice phase of the cloud top from signal depolarization (Pal and Carswell, 1978).

In the case of optically thin cirrus clouds, the importance of lidar for retrieval of significant cloud parameters has been demonstrated by ground-based

and aircraft observations (Platt and Dilley, 1979; Platt and Dilley, 1981; Spinhirne *et al.*, 1982). For cirrus, lidar signal returns may typically be obtained through the entire cloud layer, and multiple scattering may be taken into account. The cirrus parameters which may be measured from lidar returns include the optical thickness and emissivity of cirrus layers, the presence of super-cooled droplets as a component of high, thin clouds, and the presence of subvisible cirrus. The presence, height, optical thickness, and relative emissivity of cirrus are possibly the most significant cloud observations that would result from a spaceborne lidar observation.

Instrument Characteristics

The various cloud measurement objectives listed above give rise to a broad range of instrument characteristics required for spaceborne observations of clouds. The system requirements to detect the height of dense clouds are modest. Next in order of measurement difficulty are the less-dense cirrus clouds and most difficult are the subvisible cirrus. Simulations of cirrus parameter retrievals have been run for selected lidar system parameters as listed in Table 1.

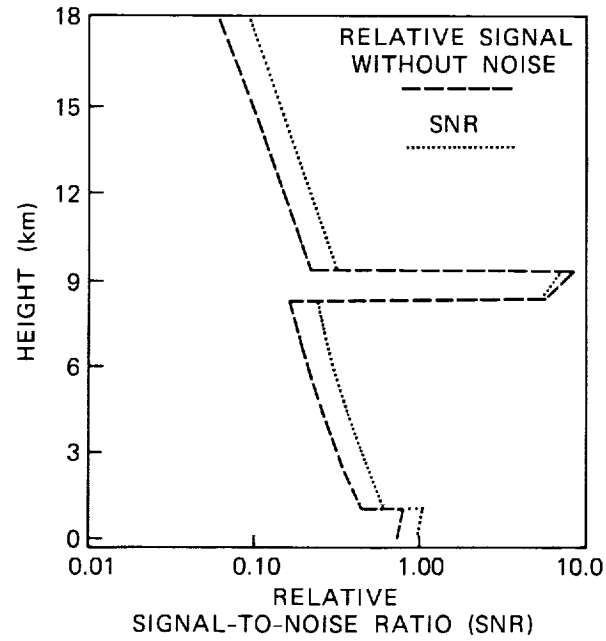

Figure 1. A modeled lidar return signal for the lidar system described in Table 1.

Table 1. System Parameters for Cloud Simulations

	Day	Night
System Altitude (km)	700	700
Receiver Clear Diameter (m)	1.0	1.0
Pulse Energy (J)	0.5	0.5
Wavelength (nm)	532	532
Detector Quantum Efficiency (%)	20	20
System Optical Efficiency (%)	25	12
Optical Bandwidth (nm)	0.2	1.0
Field-of-View (mrad)	0.2	2.5
Vertical Sampling Resolution (m)	30	30
Background Light Intensity (W/m^2-sr-nm)	0.46	5×10^{-7}

Simulations were run for a model cirrus cloud of optical thickness 0.2 and physical thickness 1.0 km to represent a thin but visible cloud. The background light intensity would correspond to cirrus over a bright, lower cloud layer. The model atmosphere included scattering by molecules and a background aerosol distribution with a boundary layer enhancement.

A modeled lidar return signal for the system parameters given in Table 1 is shown in Figure 1. The signal return has been modeled to include the expected signal noise that would exist for a single-shot return. As mentioned above, for cloud parameters it is desirable that measurements be obtained from a single laser return without recourse to averaging. From the signal return in Figure 1, it is seen that a single pulse return would be sufficient to define the presence and height of the thin cirrus layer.

The simulated signals were applied in a solution procedure that had been developed to derive the effective optical thickness of cirrus from lidar return data. The results for effective optical thickness may be presented as the number of pulses that must be averaged to achieve a given measurement accuracy. Results are given in Table 2.

In summary, for the most part, cloud parameters of interest for visibly evident clouds could be quantified to useful accuracies on a single-shot basis, with the proposed spaceborne system.

Measurement Example

An example of lidar return data for clouds is shown in Figure 2. Signal returns from both cirrus and an underlying stratus cloud layer are shown.

ORIGINAL PAGE IS
OF POOR QUALITY

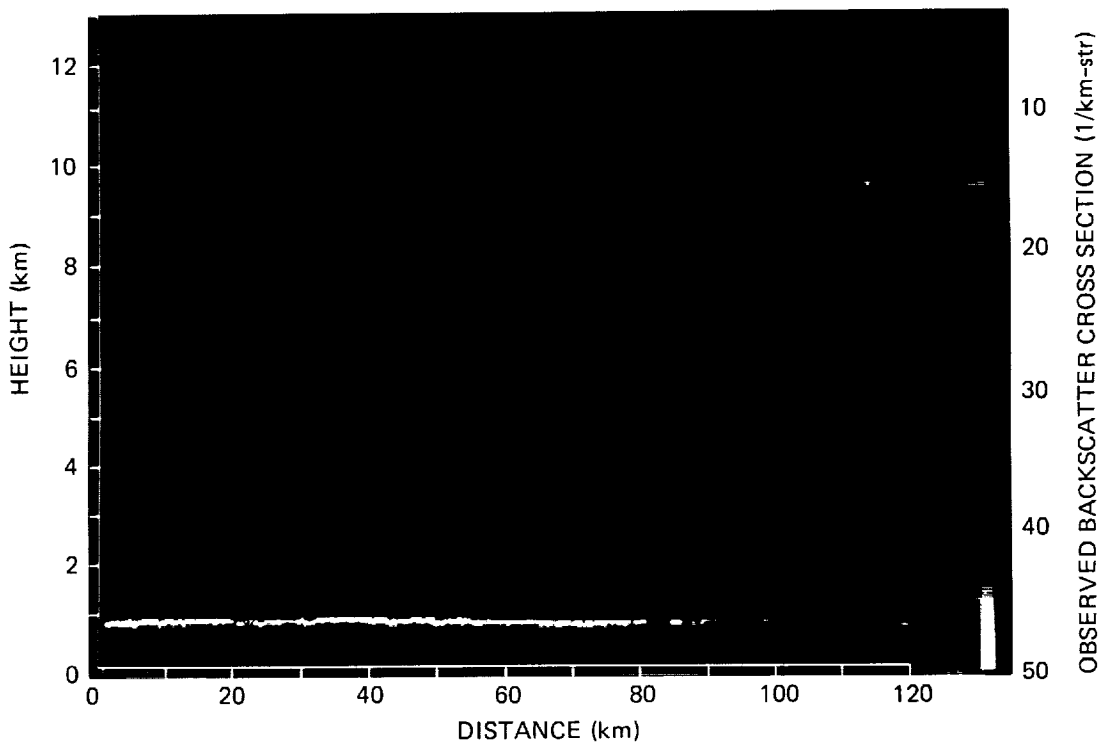

Figure 2. Example of lidar returns from both cirrus and an underlying stratus layer.

Table 2. Number of Pulses That Must be Averaged for Cloud Observations

	Day	Night
Cloud Presence	1	1
Cloud-Top Height	1	1
Cloud Backscatter Coefficient*	3	1
Cirrus Optical Thickness*	3	1

*10 percent accuracy

The data were obtained from a lidar system operating from a high-altitude (19 km) aircraft (Spinhirne *et al.*, 1982). The cirrus structure throughout the cloud layer is directly evident through the weak signal return, whereas a much stronger but rapidly attenuated signal is received from stratus. The signal measurement accuracies for the data shown are similar, on a single-shot basis, to those for the spaceborne system described previously.

PLANETARY BOUNDARY LAYER OBSERVATIONS

Measurements of PBL height on a global basis, especially over the oceans and in the Southern Hemisphere, would provide the foundation for studying the impact of the PBL and its characteristics on global circulation, storm development, and climate. The incorporation of PBL depth data into general circulation models (GCM) would open opportunities to both initialize and verify the PBL portion of the models. The results of such tests would assist in establishing the validity of basic assumptions used in the development of climate and weather models. The height of the PBL is also crucial in efforts to infer surface fluxes of energy and water vapor from remotely sensed data. To adequately support these objectives, the LASA instrument should obtain the PBL depth with a vertical resolution of 50 m over a horizontal scale of 50 km.

Measurement Approach

A convectively mixed PBL, which by definition is coupled to the surface, is characterized by a high concentration of aerosols and moisture. Generally, both the aerosol and moisture content of the free atmosphere are quite low, resulting in a sharp contrast in aerosols at the PBL top. LASA measurements of the height of this aerosol contrast can be interpreted to infer PBL depth. Continuous measurements of the PBL depth for each Eos orbit will provide a unique data set.

Measurement Simulations

PBL observations can be obtained from a basic backscatter lidar system with sufficient sensitivity to resolve aerosol scattering. The characteristics of four lidar systems that could be used for PBL observations are given in Table 3. Basically, they consist of a single-wavelength system incorporating a Nd:YAG doubled laser (λ = 0.532 μm).

Measurement simulations were performed utilizing the four lidar configurations shown in Table 3, along with a model atmosphere consisting of a U.S. Standard Atmosphere molecular profile with a simulated PBL whose aerosol content is equivalent to an optical depth of 0.05. The aerosol content in the PBL was assumed to be constant up to 750 m. Between this height and 1 km, it was assumed that the aerosol content would fall to zero linearly. An example of the expected lidar return without noise is shown in Figure 3.

Figure 4 shows the results of the simulations. The curves in Figure 4 for lidar configurations (A) through (D), as described in Table 3, respectively, show the effect of averaging lidar returns as the spacecraft moves. Curve A, a simulation for the largest lidar system, indicates that for each lidar return (0.7 km horizontal resolution) a measure of PBL height can be obtained to within ±35 m. Curve B shows the effect of reducing the receiver aperture to 0.5 m. With a 0.5 m aperture, two lidar returns (1.4 km horizontal resolution) must be averaged to obtain 50 m vertical resolution. Curve C shows the effect of reducing the laser output energy to 0.1 J. With 0.1 J laser output, 15 lidar returns (10 km horizontal resolution) must be averaged to obtain a PBL height certainty of ±50 m. Curve D represents the simulation for the smallest lidar system. A ±50 m measurement of the PBL requires lidar return averaging over a horizontal distance of 21.7 km. In summary, the smallest system (0.1 J laser output and 0.5 m aperture) can more than meet the measurement objectives of 50 m vertical resolution with 50 km horizontal averaging.

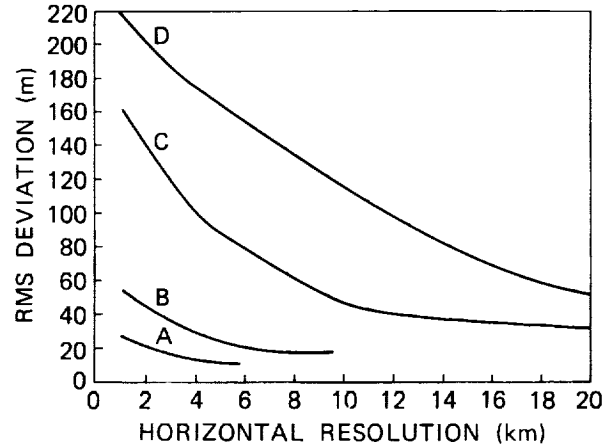

Figure 4. Root-mean-square (rms) deviation of the retrieved PBL height for satellite simulated data. Calculations performed for: λ = 532 nm, PBL depth = 875 m, and PBL optical depth = 0.05, daytime. Laser output energies and receiver apertures were as follows: A – 1.0 J, 1.0 m; B – 1.0 J, 0.5 m; C – 0.1 J, 1.0 m; D – 0.1 J, 0.5 m.

Table 3. Lidar System Configurations Used in PBL Simulations

	A	B	C	D
Laser Wavelength (nm)	532	532	532	532
Laser Output Energy (J)	1.0	1.0	0.1	0.1
Receiver Aperture (m)	1.0	0.5	1.0	0.5
Quantum Efficiency (%)	20	20	20	20
Optical Efficiency (%)	12	12	12	12
Telescope Field-of-View (mrad)	0.2	0.2	0.2	0.2
Digitization Rate (MHz)	10	10	10	10
Background	ocean	ocean	ocean	ocean

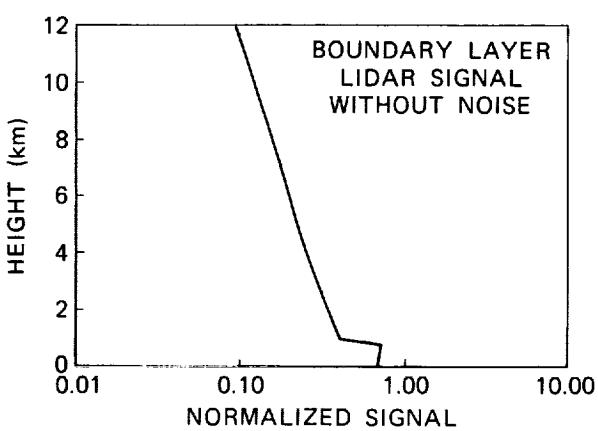

Figure 3. Expected lidar return showing the effect of aerosols trapped within the PBL.

Planetary Boundary Layer Measurement Example

PBL observations by ground-based and airborne lidar have become an established method of boundary layer research. Figure 5 shows a measure

ORIGINAL PAGE IS
OF POOR QUALITY

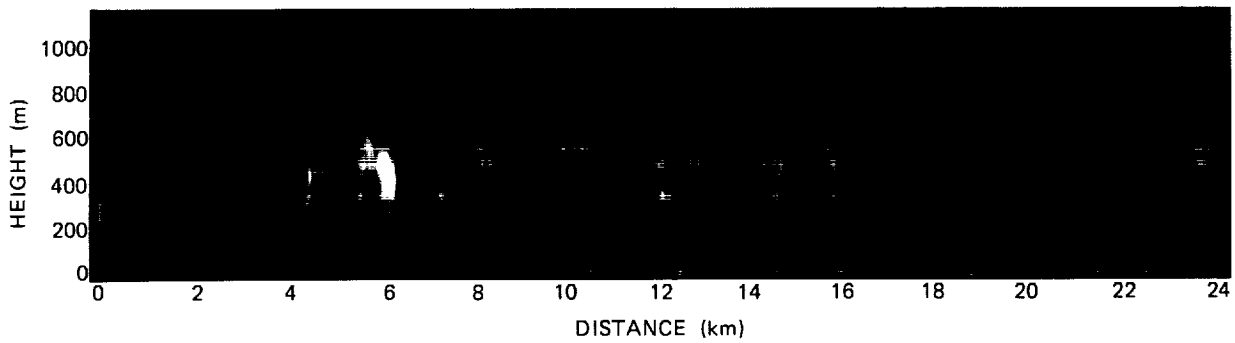

Figure 5. Lidar observations of PBL structure over the Atlantic Ocean (Melfi *et al.*, 1985).

of the structure in a developing PBL over the Atlantic Ocean during a cold arctic air outbreak in January 1983 (Melfi *et al.*, 1985). The data were acquired with a downward-looking lidar system mounted in the NASA Electra aircraft. The image, which was constructed by analyzing thousands of lidar returns, shows the sharp gradient in aerosol scattering associated with the PBL top. Also shown is the cellular convective structure that is a manifestation of strong PBL mixing.

TROPOSPHERIC AEROSOL OBSERVATIONS

Measurements of aerosols in the troposphere contribute to the understanding of atmospheric structure and dynamics and radiative budgets. Aerosol distributions can provide valuable insight into vertical and horizontal transport processes in the atmosphere. Convective cloud activity can transport gases and aerosols from the boundary layer into the free troposphere, and from the troposphere into the stratosphere. Aerosols can be used as a tracer of this vertical transport, which can occur over horizontal scales from 1 to 1,000 km. Downward transport of stratospheric air into the troposphere has been followed using aerosols as a tracer in investigations of Tropopause Fold Events (TFE). Since there are many TFEs occurring simultaneously over the globe, the global impact of these events could be studied for the first time with LASA.

Long-range transport of gases and aerosols over 100 to 10,000 km ranges can take place in the free troposphere under undisturbed conditions. LASA measurements of aerosols in these layers can provide information about the large-scale air masses and their impact on the global troposphere. Because aerosols efficiently scatter solar radiation, they must be included in any complete study of the global radiation budget. The presence of aerosol layers in the troposphere can also modify measurements of atmospheric emission in the infrared region of the spectrum and deleteriously affect various remote sensors. A secondary consequence of tropospheric aerosols is their effect on the microphysics of cloud formation and cloud radiative properties.

The objectives for the LASA measurement of tropospheric aerosols are to detect the presence of aerosol layers in the free troposphere and boundary layer and to determine the optical depth of aerosols to the surface. Since the PBL is typically 1 km in depth, vertical resolution should be 0.1 km in the PBL and approximately 1 km in the free troposphere. The aerosol optical depth of the troposphere including the PBL is typically 0.1 to 0.2 and should be measured with a resolution approaching 0.01.

Measurement Approach

A basic backscatter aerosol lidar system may be used to detect the distribution of aerosols in the free troposphere and boundary layer. By use of analysis techniques that may involve dual wavelengths or other techniques, the aerosol extinction coefficients and optical thicknesses may also be derived.

Measurement Simulations

A lidar system of sufficient power and aperture to provide signal returns that resolve aerosol scattering from background noise is required. Parameters of a lidar system that could provide the necessary accuracy are listed in Table 4.

Simulations were performed to demonstrate the feasibility of tropospheric aerosol measurements. Table 5 presents the number of lidar shots that would be necessary to detect with 95 percent confidence a change in the aerosol backscatter ratio at various levels for two altitude ranges and under day and night conditions. The detectability criterion is given in terms of the signals from a background region (S_b) adjacent to the aerosol layer under investigation and from an aerosol plus background layer (S_{a+b}) and their associated signal statistics (σ_b and σ_{a+b}, respectively). Specifically, the 95 percent detectability criterion is: $(S_{a+b} - S_b) > 3(\sigma_{a+b}^2 + \sigma_b^2)^{1/2}$. A ground reflectance of 0.3 was used in the daytime case to simulate the background solar radiation reflected from vegetation, which exceeds the

Table 4. Aerosol Lidar Parameters

Wavelength	727 nm		
Pulse Energy	500 mJ		
Pulse Rate	10 Hz		
Assumed Lidar Altitude	700 km		
Area of Receiver (active)	1.08 m^2		
FOV	0.1 mrad		
	Night*	**Day****	
Filters	Broadband	1 Å	0.1 Å
Optical Efficiency	60%	32%	29%
Quantum Efficiency	20%	20%	20%

*With interference filter
**With Fabry-Perot etalon

Table 5. Number of Shots Required to Detect Tropospheric Aerosols (No Cloud Cover)*

Atmospheric Backscatter Ratio** β_{a+b}/β_b	**Boundary Layer Aerosols** (0.5 km alt.)		**Mid-Troposphere Aerosols** (5.5 km alt.)	
	Night	**Day*****	**Night**	**Day*****
2	1	3	2	10
4	1	1	1	2
6	1	1	1	1

*Detectability of aerosols at 727 nm assuming 500 mJ/shot with no cloud cover and detectability criterion: $(S_{a+b} - S_b) > 3(\sigma_{a+b}^2 + \sigma_b^2)^{1/2}$.
**β_b is the total atmospheric backscatter coefficient of the background aerosol and β_{a+b} is that of the aerosol region to be detected.
***A 0.1 Å day filter and a ground albedo of 0.3 were used.

values for loam (0.2) and the ocean surface (0.03). The values listed in the table are for the case of no cloud cover.

It can be seen that even for the daytime case in the middle troposphere, an aerosol layer having a factor of two enhanced backscatter over the background level can be detected within 1 sec (10 shots or 8 km horizontal resolution). Small changes in the aerosol scattering can be detected with little horizontal averaging at the top of the boundary layer. The factor of $\beta_{a+b}/\beta_b = 2$ at 0.5 km corresponds to a visibility of 12 km in the boundary layer compared to 23 km above it. These are not unreasonable values for an unpolluted rural atmosphere. Table 6, using the same detectability criterion as in the no-cloud case, presents the results for the condition of a cloud cover having a one-way optical depth of 0.5. This is comparable to the characteristics of a moderate cirrus cloud condition. Nighttime measurements are degraded from the no-cloud case by about a factor of two, while the daytime measurements are degraded by about a factor of four. The increased daytime degradation is to be expected because of the higher background levels. Even under these adverse conditions, thin aerosol layers can be detected with reasonable horizontal resolutions (<32 km).

Measurement Example

Aerosol profiles in the free troposphere can be used to indicate the presence of stable layers, and these layers can be investigated in long-range transport studies (Browell *et al.*, 1983; Browell *et al.*, 1985; Shipley *et al.*, 1984). Figure 6 shows a Saharan dust layer aloft at about 3 km near Barbados on June 21, 1984 (Talbot *et al.*, 1986) (The data were taken from the NASA Electra aircraft with a down-looking lidar.) This layer was transported from the African continent over a period of 8 days. The marine boundary layer and some scattered clouds can also be seen in the figure.

Figure 7 shows another example of lidar measurements of elevated aerosol layers made from the NASA Electra aircraft. In this figure, a tongue of stratospheric-aerosol-laden air in a tropopause fold is shown in the lower troposphere over the Western United States (Browell *et al.*, 1986). The layer of stratospheric origin became perturbed by the

Table 6. Number of Shots Required to Detect Tropospheric Aerosols (With Cloud Cover)*

Atmospheric Backscatter Ratio** β_{a+b}/β_b	Boundary Layer Aerosols (0.5 km alt.)		Mid-Troposphere Aerosols (5.5 km alt.)	
	Night	Day***	Night	Day***
2	2	9	5	43
4	1	2	1	6
6	1	1	1	3
8	1	1	1	2
10	1	1	1	1

*Detectability of aerosols at 727 nm assuming 500 mJ/shot with a cloud optical depth of $\tau = 0.5$, and detectability criterion as in Table 5.
**β_b is the total atmospheric backscatter coefficient of the background aerosol and β_{a+b} is that of the aerosol region to be detected.
***A 0.1 Å day filter and a ground albedo of 0.3 were used.

boundary layer and eventually was fumigated into the boundary layer.

STRATOSPHERIC AEROSOL OBSERVATIONS

Detailed information on the global distribution of stratospheric aerosols can directly contribute to studies of stratospheric motions and to radiative model calculations. The analytical techniques for these stratospheric aerosol measurements have been well developed during 20 years of both ground-based and aircraft-based experiments. Spaceborne lidar measurements of stratospheric aerosols can provide better horizontal and vertical resolution than passive sensors for some aerosol loading conditions, and can provide much more information per orbit of the spacecraft. Simultaneous tropospheric measurements are useful for subsequent stratospheric/tropospheric exchange studies. The capability of these lidar measurements presents unique opportunities for measuring transient atmospheric events such as volcanic plumes and noctilucent and polar stratospheric clouds. In addition, lidar data obtained after volcanic eruptions can greatly aid in assessing aerosol effects on other remote sensors. For example, the large loading caused by the eruptions of El Chichon was shown to affect many spacecraft remote sensors (Bandeen and Fraser, 1982). Finally, a spaceborne lidar will greatly enhance our ability to monitor events that occur in otherwise inaccessible regions of the globe.

The objective is to determine stratospheric aerosol layering characteristics by measuring backscatter profiles at a minimum of two wavelengths and possibly two polarizations over each spacecraft orbit, with at least a 300-to-500 km horizontal and 2 km vertical resolution under background aerosol loading conditions. For special conditions, like those after a recent volcanic eruption, or for the study of stratospheric clouds and dynamical phenomena, the horizontal resolution will be reduced to about 100 km. These profiles will be used to describe aerosol amounts and distributions in the stratosphere, developing a global aerosol climatology. Studies using these data will include, as examples, aerosol effects on atmospheric temperature fields, aerosol potential for climate perturbation, heterogeneous surface chemistry, aerosol effects on photochemistry, and the use of aerosols as tracers for transport and circulation studies. In addition, the measurement objectives will include the investigation of stratospheric clouds (McCormick *et al.*, 1982).

Satellite-based lidar measurements will provide a greatly expanded opportunity for global sampling and geographic mapping of stratospheric aerosol spatial and temporal distributions. Measurements would be performed primarily in nighttime viewing conditions, but daytime measurements could also be obtained with longer integration times (and concomitant coarser horizontal resolution). Obviously, a spaceborne lidar instrument would be able to respond in sufficient time to make successful measurements of transient atmospheric events like volcanic eruptions. These measurements would permit detailed mapping of the volcanic plumes and subsequent studies of their transport and diffusion over time. Such measurements would greatly enhance the available data base for global climate and circulation studies. In addition, unique events such as the seasonal occurrence of polar stratospheric clouds (PSC) in the arctic and antarctic regions could be successfully monitored with a spaceborne lidar aerosol measurement system. The uniqueness of these PSCs has been documented by observations with the SAM II satellite experiment and two airborne lidar missions to the arctic region. Active lidar measurements from space would provide greatly enhanced opportunities for a more complete mapping of the occurrence of these unusual high-altitude clouds. In addition, they would allow much

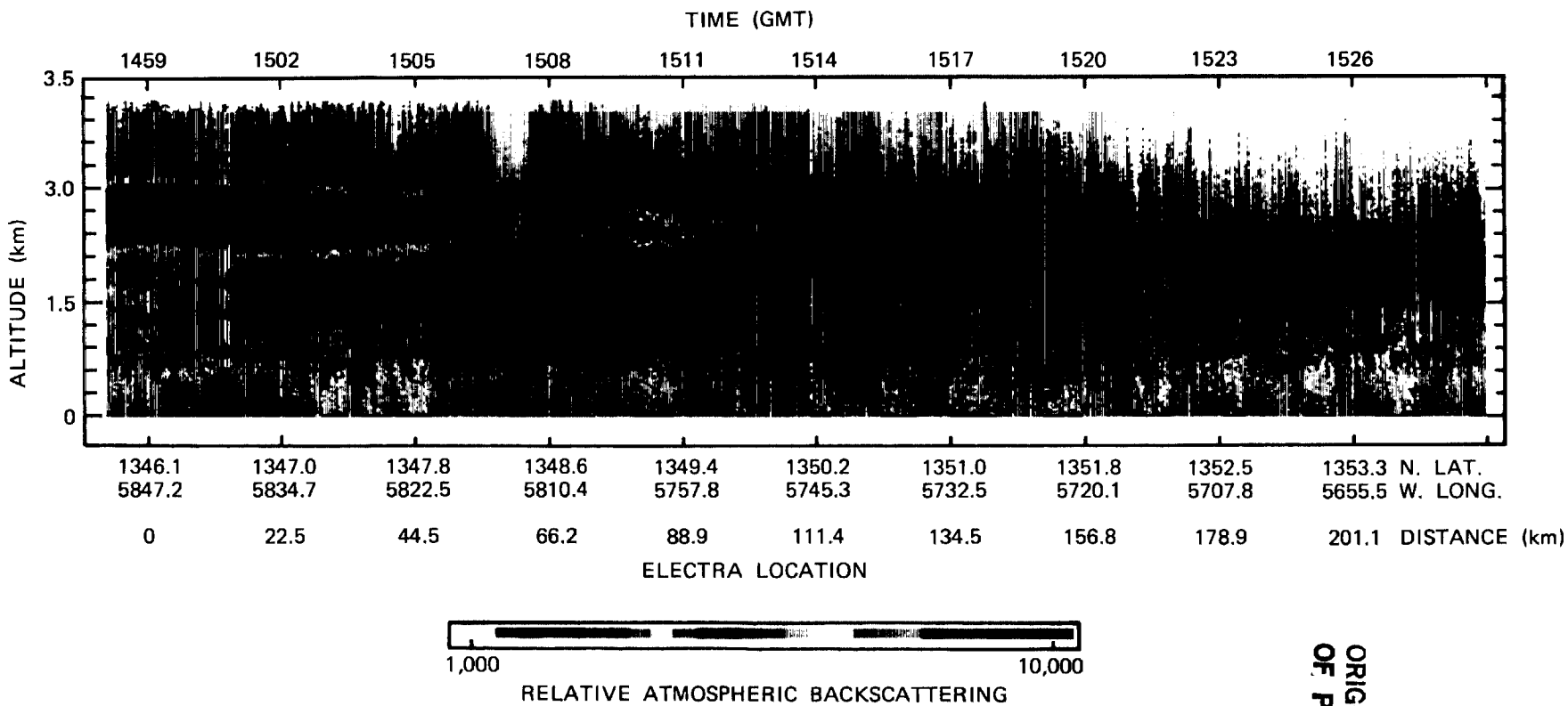

Figure 6. Lidar observations of Saharan dust layer near Barbados.

ORIGINAL PAGE IS
OF POOR QUALITY

ORIGINAL PAGE IS
OF POOR QUALITY

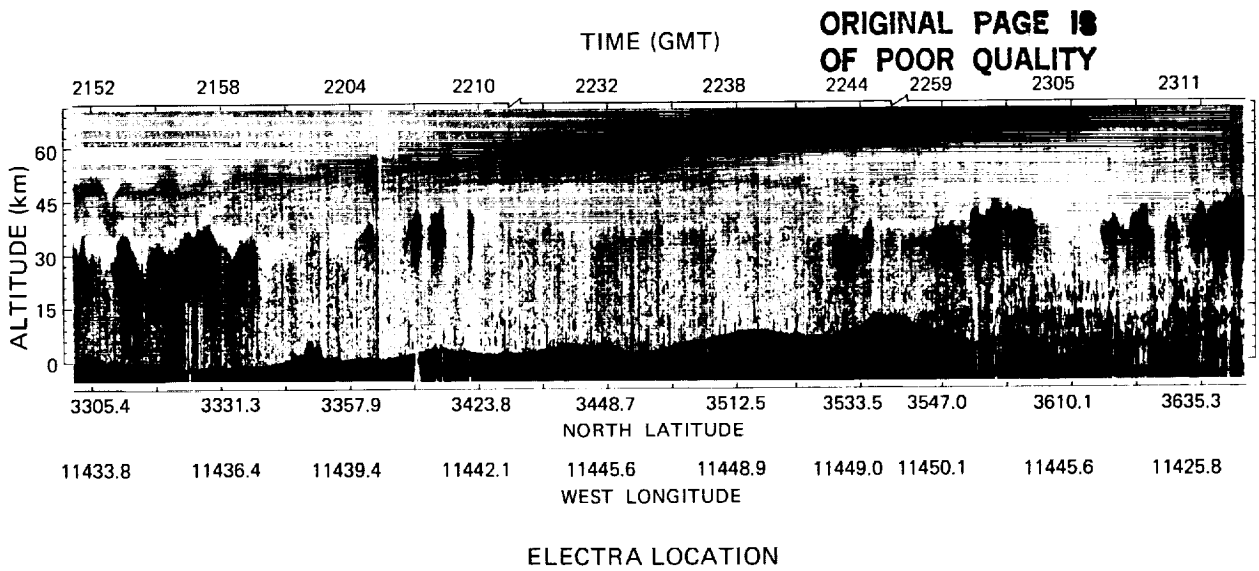

Figure 7. Lidar observations of aerosols in a tropopause fold event located over the Western U.S.

more complete studies of the inaccessible antarctic region.

Measurement Approach

The measurement technique utilizes elastic backscattering of the transmitted lidar signal, which is highly sensitive to the spatial distribution of stratospheric aerosols. Coordinated spaceborne lidar measurements with the SAGE II satellite sensor can also be performed. The combination of the lidar aerosol backscatter profile with the retrieval of aerosol extinction at several wavelengths would yield valuable information on the optical scattering properties of the stratospheric aerosol for deriving important aerosol radiative parameters.

Passive radiometers flown with a spaceborne lidar could provide coordinated data to combine with the high vertical resolution of the backscatter aerosol profile. These measurements would yield important information for the definition of the optical scattering properties of the stratospheric aerosol and also help in the retrieval of more accurate temperature profiles and cloud properties.

Measurement Simulations

Simulations have been performed to demonstrate the sensitivity in percent error for quantitatively retrieving from LASA the aerosol backscatter coefficient or scattering function in the stratosphere as a function of various vertical and horizontal resolutions and instrument parameters.

The aerosol model used in these simulations was based on a background mid-latitude profile, while a molecular density profile was modeled from the 1976 U.S. Standard mid-latitude atmosphere. Figure 8 plots the input atmosphere in terms of the backscattering coefficient as a function of altitude for a visible wavelength of 0.71 μm. Curve A is the aerosol backscatter coefficient profile, while curve

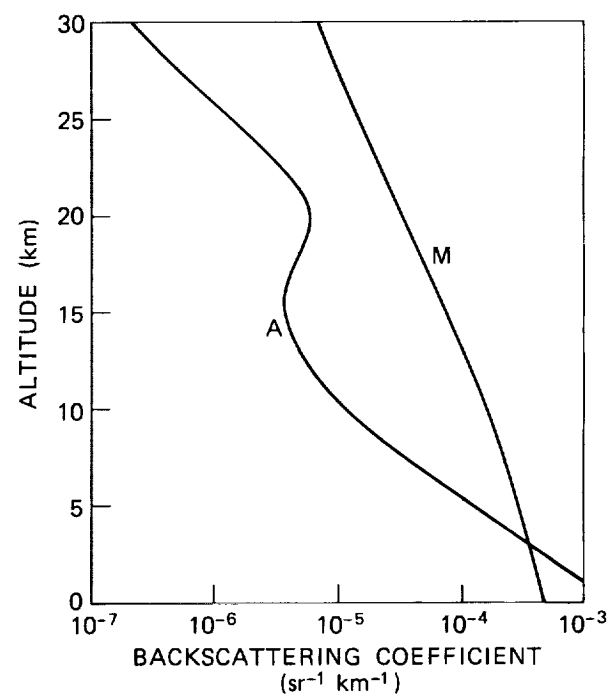

Figure 8. Model atmosphere extinction coefficient plotted as a function of altitude for λ = 0.71 μm. Curve A is the aerosol backscatter coefficient profile for background stratospheric aerosol concentrations, and curve M is the molecular backscatter profile for the 1976 Standard Atmosphere.

M is the corresponding molecular backscatter coefficient profile.

Table 7 describes the two lidar systems used in the simulations. Molecular density errors of 3 percent for z < 30 km and 5 percent for z > 30 km have been assumed, based on prior experience with the SAM II and SAGE satellite data analysis. It turns out that these molecular density uncertainties result in the largest error source when retrieving the aerosol scattering function (not just the total scattering function or backscatter radiance profile). The details of this analysis are given in Russell *et al.* (1979). Simultaneous two-wavelength lidar measurements can be performed where one wavelength in the UV is used to retrieve a lidar-derived molecular density profile in the stratosphere. If the result is employed with a visible wavelength lidar measurement, greatly improved accuracies are obtained for retrieving the aerosol scattering function (Russell and Morley, 1982). In addition, it should be realized that the simulations presented here are in terms of accuracy of retrieving aerosol backscatter coefficients or scattering functions. The measurement of the relative changes in aerosol scattering is straightforward and can be easily implemented with very few laser pulses.

Figure 9 summarizes the simulations for the stratosphere using the atmospheric model described above for a wavelength of 0.71 μm. As can be seen in the figure, the error in the retrieved aerosol backscatter coefficient (or aerosol backscatter function) is about 30 percent at the peak of the stratospheric aerosol layer (20 to 22 km) for these modeled background conditions. For volcanic conditions where there are enhanced aerosol concentrations such as those present in the stratosphere in 1986 from the El Chichon eruption of 1982, the retrieved accuracies at the layer peak are about 15 percent. Near the mid-latitude troposphere, where the aerosol concentrations are at a minimum, the retrieved accuracies are the worst, reflecting the minimal aerosol backscattering at those heights.

At all heights the molecular density uncertainties represent the dominant source of error. To minimize the uncertainty, the molecular as well as the aerosol backscatter coefficients can be obtained from a simultaneous two-wavelength lidar measurement. The second wavelength used is the frequency-doubled wavelength of 0.355 μm. The analysis technique consists of retrieving the aerosol backscatter profile at the fundamental wavelength of 0.71 μm in the usual single-wavelength manner. This aerosol profile can be modeled by a wavelength conversion factor to the aerosol backscatter profile at 0.355 μm. The estimated aerosol backscatter profile can then be combined with the measured lidar signal at 0.355 μm to yield a relative molecular density backscatter profile. This relative density profile is normalized to absolute values at a height where the density can be estimated to high-accuracy *a priori*. The level chosen is the isopycnic layer at a height of 8 km where

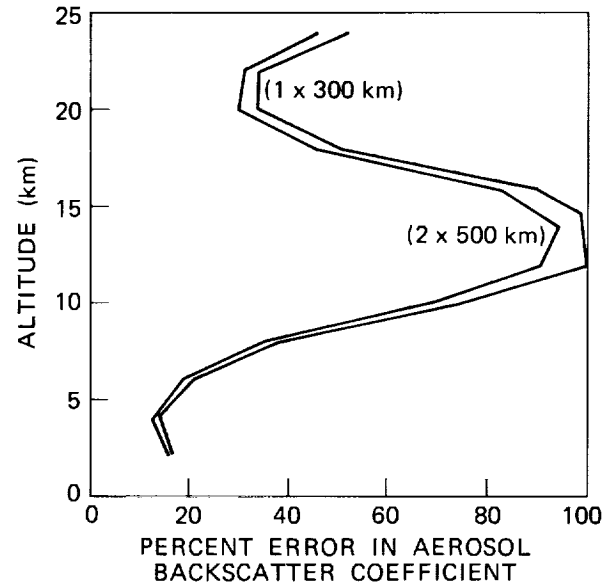

Figure 9. Simulation results for the percent error in the aerosol backscatter coefficient at λ = 0.71 μm, using model molecular density profile. Lidar characteristics are those listed in Table 7 for λ = 0.71 μm. The numbers in parentheses above refer to vertical and horizontal resolutions, respectively.

Table 7. Characteristics of Lidar Used in Two-Wavelength Simulations*

	Frequency Doubled	Fundamental
Wavelength	0.355 μm	0.71 μm
Energy	0.20 J	1.0 J
Rate	10 Hz	10 Hz
System Optical Efficiency	0.08	0.40
Quantum Detection Efficiency	0.20	0.15

*Assumed Conditions: Spacecraft Altitude = 700 km
Diameter of Receiver = 1.25 m
Receiver Field-of-View = 5×10^{-4} rad
Density Error = 3% for z < 30 km, 5% for z > 30 km

yearly density variations are of the order of 1 percent. The lidar-derived density profile and its associated errors are used with the lidar signal at the 0.71 μm wavelength to rederive the aerosol backscatter profile. The simulated error results using these two wavelengths are shown in Figure 10. With the lidar-derived density analysis, the errors in the retrieved aerosol backscatter coefficient have been reduced greatly and, at the peak of the aerosol layer, the error rate is about 15 percent.

The two-wavelength analysis of simultaneous lidar signals at 0.355 and 0.71 μm has been shown to give greatly improved results for the retrievals of the stratospheric aerosol backscatter coefficients. In addition, the lidar-derived density profile at the 0.355 μm wavelength can be analyzed for temperature. It is anticipated that such a temperature retrieval will result in uncertainties of 2 K between about 40 and 8 km.

Measurement Example

A long-term lidar data set of stratospheric aerosol measurements taken at a fixed site of 37°N, 76°W is shown in Figure 11 (McCormick *et al.*, 1984). The figure, which plots integrated aerosol backscattering function from the tropopause through 30 km at wavelength 0.6943 μm versus time, clearly shows the effects of the eruptions of various volcanoes (vertical arrows indicate the times of known eruptions) on stratospheric aerosol loading.

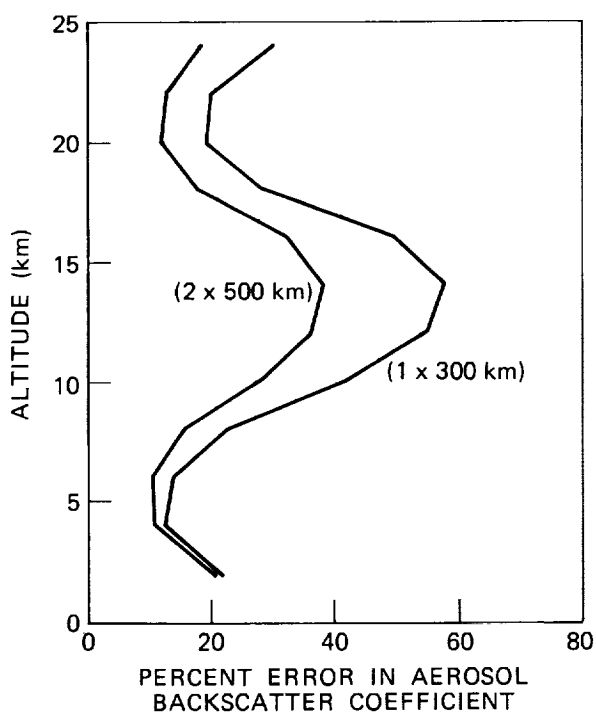

Figure 10. Simulation results for the percent error in the aerosol backscatter coefficient at λ = 0.71 μm, using lidar-derived molecular density profile (two-wavelength analysis). Lidar characteristics are those listed in Table 7 for λ = 0.355 μm and 0.71 μm.

An example of a cross-sectional plot of aerosol backscatter ratio versus height and latitude from aircraft measurements made over the Pacific Ocean about 1 year after the eruption of El Chichon is shown in Figure 12. By this time, the stratospheric material produced from the April 1982 eruption is shown to be spread throughout the latitudes 56°S to 72°N, the latitudes covered by this flight campaign.

WATER VAPOR OBSERVATIONS

The study of water vapor in the troposphere addresses important atmospheric processes in the large-scale hydrological and biogeochemical cycles, climate, and meteorology. The hydrological cycle was cited by the Eos Science and Mission Requirements Working Group (SMRWG) as the primary scientific issue that would require high-spatial-resolution water vapor data from a spaceborne lidar system. The transport of water and changes in its physical state are key to understanding the Earth as a system.

Lidar measurements of water vapor, especially in data-sparse regions, provide necessary inputs to both meteorological and climatological studies. Table 8 summarizes the science and observational requirements for the LASA measurements of water vapor. In general, the observational requirements for the global hydrological cycle are the most stringent of those listed.

Measurement Approach

Water vapor column content and profiles can be measured by the DIAL technique using water vapor spectral lines in the region from 725.2 to 730.9 nm. Using the DIAL technique, ratios are obtained of lidar return signals at two wavelengths, the ON and OFF wavelengths, which are typically separated by <70 pm. For the DIAL measurements to be useful, the ON and OFF wavelengths should be transmitted near simultaneously, and hence the DIAL system requires two laser sources. When pulsed laser sources are used, the range-resolved number density n of water vapor molecules can be calculated using the formula:

$$n = \frac{1}{2\Delta\sigma(Z_1 - Z_2)} \cdot \ln\left[\frac{P_{on}(Z_1)}{P_{on}(Z_2)} \cdot \frac{P_{off}(Z_2)}{P_{off}(Z_1)}\right]$$

where $\Delta\sigma$ is the differential absorption cross section per molecule of the species being measured in the altitude region Z_1 to Z_2. For the column-content measurement, only ON and OFF signals from a

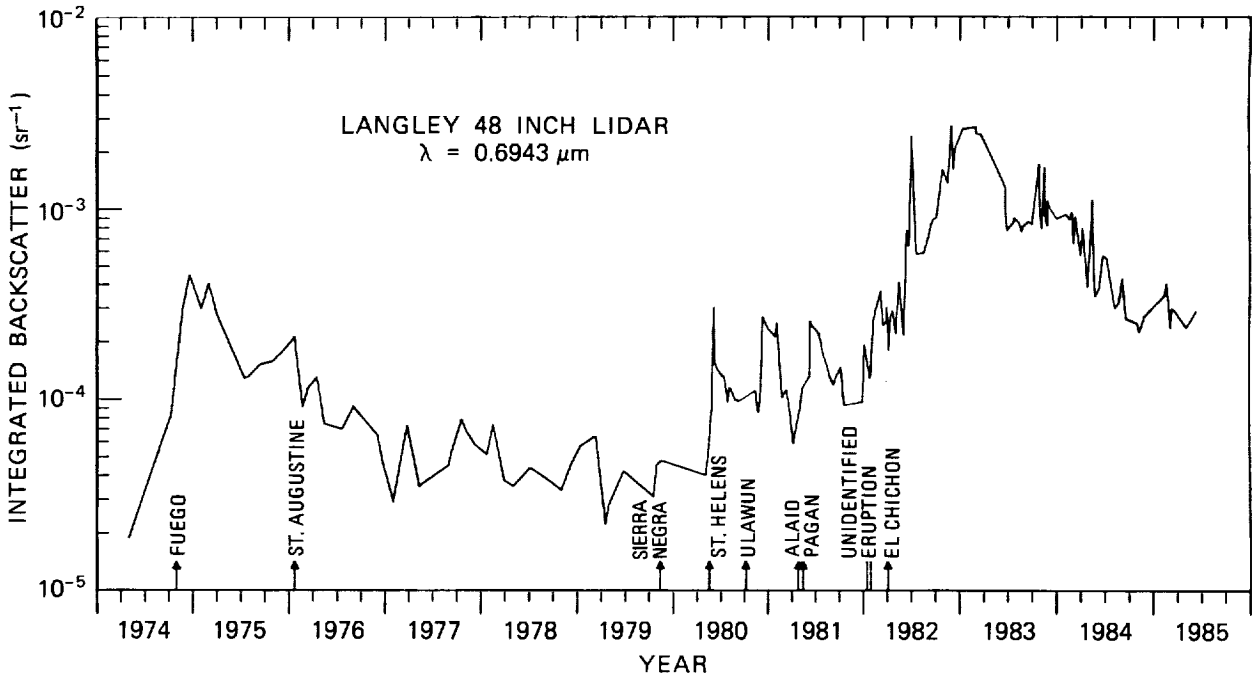

Figure 11. Long-term variation of integrated stratospheric aerosol backscattering function – Hampton, Virginia (37°N).

Table 8. Water Vapor Science Needs

Application	Science Problem	Observational Requirements			
		Altitude	Resolution Δz	Resolution Δx	Accuracy
Global Hydrological Cycle	Precipitation, Evaporation, Evapo-transpiration, Atmospheric Transport	0 to 10 km	1 km	100 km	±10%
Radiative Budget/Climate	Water Vapor Influence on Global Radiative Budget	0 to 10 km 10 to 30 km	2 km 2 km	500 km 400 km	±20% ±50%
Atmospheric Composition and Trace Gases	Trace Flow of Gases and Aerosols	0 to 10 km 10 to 50 km	1 km 2 km	100 km 500 km	±10% ±10%
Meteorology	Improve Short- and Long-Term Predictions and Augment Synoptic Observations in Data-Sparse Regions	0 to 8 km	1 km	250 km	±10%

strong reflecting target (like ground or a cloud) are needed.

Measurement Simulations

Predictions of LASA DIAL system performance have been made based on computer simulations. LASA DIAL system parameters assumed in these simulations were the same as those given in Table 4. The lasers used in this differential absorption technique must have a spectral purity of better than 99.5 percent.

Table 9 lists the various atmospheric models for aerosols, water vapor, temperature, and pressure used in the following experiment simulation calculations. Model water vapor profiles for tropical, mid-latitude summer, mid-latitude winter, and subarctic winter regions are shown in Figure 13. These models are used in water vapor DIAL simulations to show

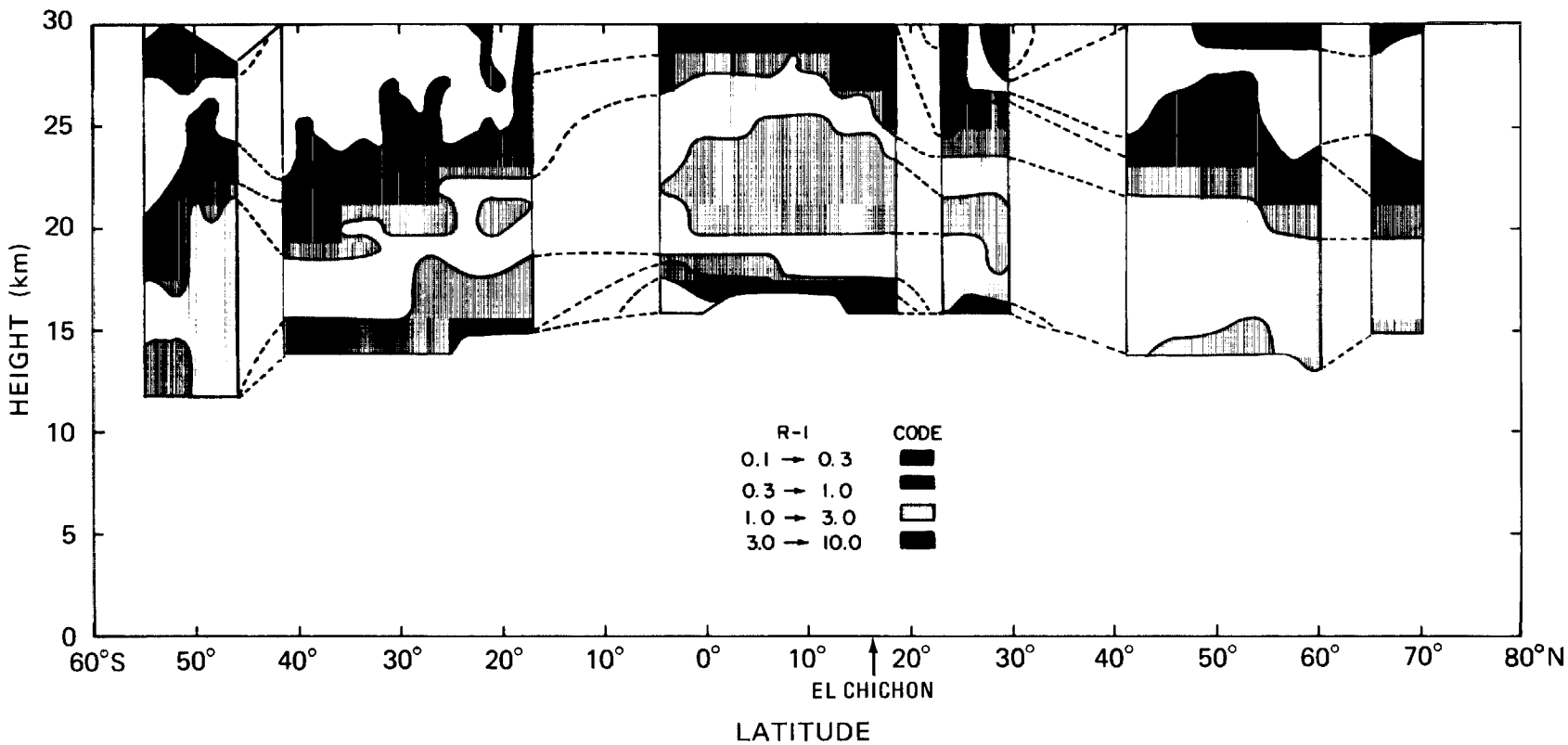

Figure 12. Aerosol backscatter ratio measured by aircraft over the Pacific Ocean 1 year after the eruption of the El Chichon volcano.

Table 9. Model Atmospheres

Model Type	Reference
Molecular Atmosphere	U.S. Standard 1976 Mid-latitude Model
Aerosol Model	The Deirmendjian Haze M Model with a 23 km Visibility for Background Aerosols
Water Vapor Profile	Tropical, Mid-latitude (Summer/Winter), and Subarctic Winter (McClatchey *et al.*, 1972)
Other Profiles (Pressure and Temperature)	Mid-latitude Model (McClatchey *et al.*, 1972)

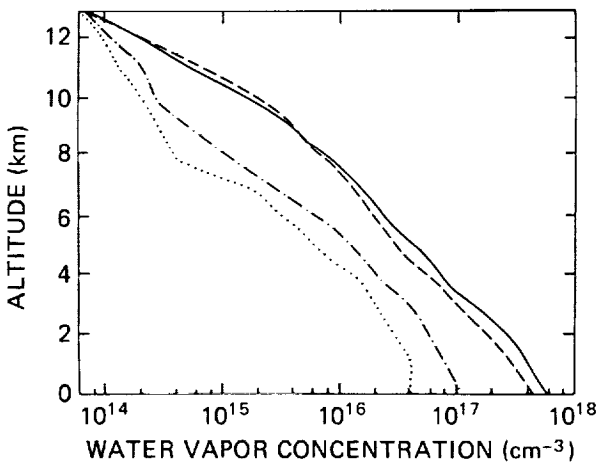

Figure 13. Water vapor concentration profiles for the indicated latitudinal bands and seasons: —— tropical, ----- mid-latitude (summer), —·— mid-latitude (winter), ····· subarctic (winter).

the effect of water vapor profile variations on DIAL measurement uncertainties. The tropospheric aerosol model used in the aerosol and water vapor DIAL calculations, the Deirmendjian Haze M model with phase function $\rho_\pi/4\pi = 0.01$, is shown in Figure 14 (dashed line). Using an off-line wavelength of 727 nm leads to the return signal per 100 m range bin shown in the figure (solid line). The wavelength chosen (727 nm) is representative of off-line wavelengths in this water vapor band where the return signal will be relatively constant with wavelength. The horizontal bars represent the one sigma variation of the signal for each shot.

Candidate water vapor absorption lines that could be used in LASA DIAL measurements are listed in Table 10. Selection of appropriate water vapor absorption lines for application in various latitudinal and altitude regions will produce less than 1 percent error in the DIAL measurement resulting from temperature uncertainties.

The results of the simulations are estimates of the uncertainties which can be achieved. Table 11 shows the measurement uncertainties in the measurement of water vapor total column content. A surface reflectance of 0.03 (corresponding to the ocean) is used in these calculations. As can be seen from the table, a nighttime measurement uncertainty of <10 percent is achievable for a single shot for all assumed water vapor profile conditions and for any of the three water vapor absorption lines. This indicates that the water vapor column-content measurement could be made using only one water vapor line for all latitudes. The daytime measurement uncertainties are more dependent on the choice of water vapor lines. A compromise choice of water vapor lines, such as one having a cross section of 10.0×10^{-24} cm^2, produces a water vapor column-content measurement uncertainty of <10 percent over all latitudes for both day and night. This results in a water vapor column-content measurement every 800 m along the satellite ground track.

Table 12 shows the variation in water vapor measurement uncertainty with different surface albedos and various water vapor models. Even with an absorption cross section of 7.0×10^{-24} cm^2, the results indicate that over land a measurement uncertainty of <5 percent can be achieved for all water vapor profiles investigated. Scanning of this system would provide 20 column-content measurements on a 30 km × 30 km grid over a ±500 km cross-track scan, and an average of 10 samples would be obtained for each 100 km × 100 km resolution element.

LASA has the capability to make water vapor profile measurements as well as the column-content measurements just discussed. Figure 15 shows the LASA water vapor profile measurement uncertainties for various water vapor absorption line cross sections. For the mid-latitude water vapor summer profile, the optimum measurement region is dependent on the selection of the water vapor

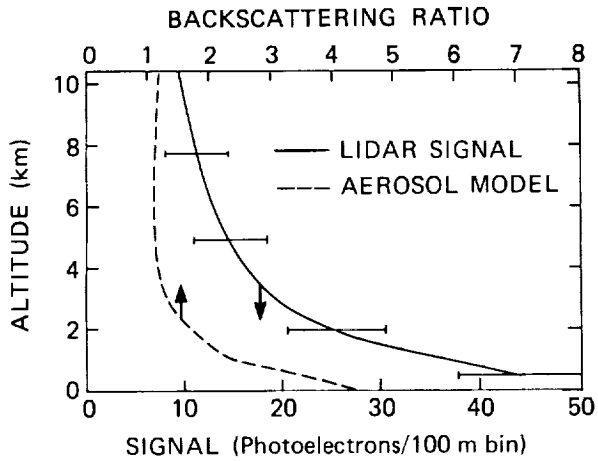

Figure 14. Tropospheric aerosol model and lidar signal for each 500 mJ pulse at 727 nm. Atmospheric backscattering ratio ($\beta_m + \beta_a$)/β_m corresponds to Deirmendjian Haze M aerosol model with phase function, $\rho_\pi/4\pi$ = 0.01.

absorption line, and it gets progressively higher with increasing water vapor absorption cross section. Operation on the 40.0×10^{-24} cm^2 line would permit measurements from about 800 m to 7 km altitude with <10 percent uncertainty for a 1 km vertical resolution (Δz) and a 100 km horizontal resolution (Δx). To cover the entire altitude range from the surface to 100 km altitude would require the use of two water vapor lines; however, the range from 0 to 6 km could be covered by one line.

Figure 16 gives the results of simulations for various latitudinal water vapor models. These results show that the water vapor line used in this calculation is optimum for maximum altitude coverage in tropical and mid-latitude summer regions. In the other two regions, the use of this line is limited to below 3 km altitude.

Daytime measurements of water vapor profiles provide important information on diurnally varying atmospheric processes. Figure 17 presents results of simulation calculations for daytime water vapor profile measurements using various water vapor lines and a surface albedo of 0.3. The region of minimum measurement uncertainty is restricted to the lowest 4 km. Measurements up to 9 km can be made with <20 percent uncertainty, and with additional horizontal averaging to Δx = 250 km. This uncertainty can be reduced to near 10 percent (see Figure 18). The variation in daytime water vapor measurement uncertainties with water vapor model profiles is shown in Figure 19. Daytime measurements are more restrictive in the usable altitude range for each water vapor line than are the nighttime measurements. As a result, there will have to be different water vapor lines used for the different latitudinal regions of interest. The lines chosen could complement each other in improving latitudinal and altitude coverage. For example, lines having cross sections of 10.0×10^{-24} (see Figure 19) and 40.0×10^{-24} (see Figure 20) would complement each other in altitude coverage in the mid-latitude summer region; and, whereas the 10.0×10^{-24} line could be used for the low altitudes in the mid-latitude summer, and the 40.0×10^{-24} line could be used for the mid-latitude winter and subarctic regions at low altitudes.

The LASA system will be able to measure water vapor profiles under night or day conditions with vertical and horizontal resolutions of <0.1 km and

Table 10. Candidate Temperature-Insensitive Lines for LASA Water Vapor DIAL

	λ (nm)	σ_o ($\times 10^{-24}$ cm^{-2})	E″ (cm^{-1})	S° (cm^{-1}/molec/cm^2)	γ_L^o (cm^{-1})
1	726.5594	86.40*	136.77	32.30	0.1190
2	727.0129	9.41	325.35	2.54	0.0859
3	727.5407	41.20*	212.15	14.31	0.1106
4	727.6314	11.45	224.83	3.30	0.0919
5	727.6549	9.70*	224.83	3.13	0.1026
6	727.6848	12.25	222.06	4.10	0.1064
7	727.7388	70.10	224.83	24.10	0.1097
8	727.8078	16.79*	222.06	5.75	0.1092
9	728.7379	43.10	300.35	14.53	0.1074
10	728.8126	20.87*	275.52	7.05	0.1075
11	729.1401	4.37	325.35	1.35	0.1019
12	729.2109	14.78	315.79	4.71	0.1015
13	730.8701	5.95	285.43	1.311	0.0702
14	730.8782	13.00	285.43	4.100	0.1010

*These cross-section values are ±5% of the values used in simulations.

Definitions: σ_o is the center line absorption cross section at standard temperature and pressure (STP); E″ is the ground-state energy level; S° is the absorption line strength at STP; γ_L^o is the absorption line half-width at STP.

Table 11. Percent Measurement Error Per Shot from LASA DIAL Water Vapor Column-Content Simulations* for Various Water Vapor Absorption Line Cross Sections, $\Delta\sigma$

Model Water Vapor Profile	$\Delta\sigma = 19.5 \times 10^{-24}$ cm^2		$\Delta\sigma = 10.0 \times 10^{-24}$ cm^2		$\Delta\sigma = 7.0 \times 10^{-24}$ cm^2	
	Night	Day**	Night	Day**	Night	Day**
Tropical	9.8	75	3.9	8.3	3.4	5.6
Mid-latitude Summer	4.9	18	3.5	5.8	3.9	5.6
Mid-latitude Winter	3.9	6.6	6.5	9.3	9.3	15
Subarctic Winter***	1.4	1.9	2.6	3.3	3.6	4.6

*Assumes pulse energy = 500 mJ, albedo (ρ) = 0.03
**A 1 Å interference filter is assumed.
***A surface albedo of 0.6 is assumed for the snow-covered subarctic region.

Table 12. Percent Measurement Error Per Shot from LASA DIAL Water Vapor Column-Content Simulations for Various Surface Albedo Variations, ρ

Model Water Vapor Profile	$\rho = 0.03$ (Ocean)		$\rho = 0.2$ (Loam)		$\rho = 0.3$ (Vegetation)	
	Night	Day*	Night	Day*	Night	Day*
Tropical	3.4	5.6	1.4	2.2	1.1	1.8
Mid-latitude Summer	3.9	5.6	1.6	2.2	1.3	1.8
Mid-latitude Winter	9.3	15	3.5	4.8	2.8	3.9
Subarctic Winter**	3.6	4.6	3.6	4.6	3.6	4.6

Water vapor absorption line cross section is: $\Delta\sigma_o = 7.0 \times 10^{-24}$ cm^2.
*A 1 Å interference filter is assumed.
**A surface albedo of 0.6 is assumed for the snow-covered subarctic region.

100 to 250 km, respectively. Nighttime measurements in a given latitudinal region can be made to <10 percent uncertainty over a 6 km altitude range using one water vapor line. To globally study the <3 km altitude region, only one water vapor line will be required for nighttime measurements, and daytime global coverage measurements can be achieved using two water vapor lines. Investigations at mid- to upper-tropospheric altitudes will need line selections for the specific latitudinal region to be studied.

Some calculations, assuming reasonable improvements in overall LASA system performance, indicate the possibility of measuring water vapor profiles with a 10 percent measurement accuracy for a vertical and horizontal resolution of 0.5 km and 50 km, respectively, during night, and also permit 10 percent measurement accuracy over the oceans during day with a resolution of 1 km and 100 km, respectively. It is also expected that with stronger new laser sources the water vapor DIAL technique could be used in the 0.93 μm region where stronger water vapor absorption lines are available that will permit measurements up to about the 12 km altitude range.

Measurement Example

Figure 21 shows water vapor variations in the marine boundary layer across the Gulf Stream Wall as measured on September 24, 1982, with an airborne DIAL system aboard the NASA Electra aircraft (Browell *et al.*, 1984). The abrupt decrease in water vapor missing ratios can be seen at the top of the boundary layer on both sides of the Gulf Stream Wall. There are some small-scale variations in the water vapor mixing ratios in the boundary layer; however, in this example, there does not seem to be any significant difference in the average water vapor concentrations on the two sides of the Gulf Stream

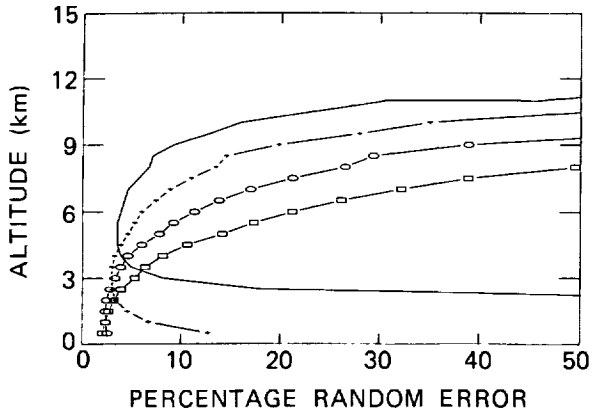

Figure 15. LASA water vapor DIAL range-resolved measurement simulations. Variations with line strength (night filter, mid-latitude (summer) water vapor model. Calculations performed for: λ_{on} = 727 nm, 500 mJ pulse at 10 Hz, Δz = 1,000 m, Δx = 100 km. Water vapor line absorption cross sections ($\Delta\sigma$):
——— 90.1 × 10^{-24} cm², ·—·—· 40.0 × 10^{-24} cm², ○—○—○ 19.5 × 10^{-24} cm², □—□—□ 10.0 × 10^{-24} cm².

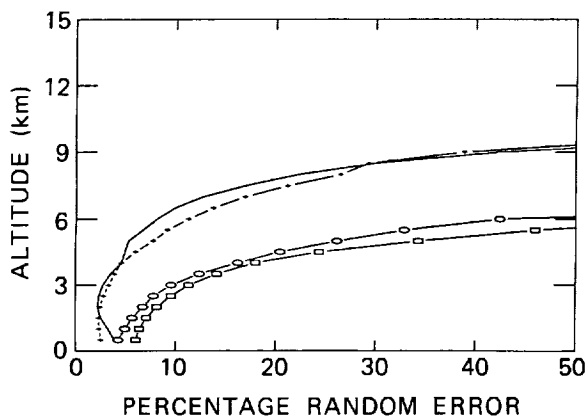

Figure 16. LASA water vapor DIAL range-resolved measurement simulations. Latitudinal variations (night filter). Calculations performed for: $\Delta\sigma$ = 19.5 × 10^{-24} cm², λ_{on} = 727 nm, 500 mJ pulse at 10 Hz, Δz = 1,000 m, Δx = 100 km. Latitudinal bands and seasons as follows: ——— tropical, ·—·—· mid-latitude (summer), ○—○—○ mid-latitude (winter), □—□—□ subarctic (winter).

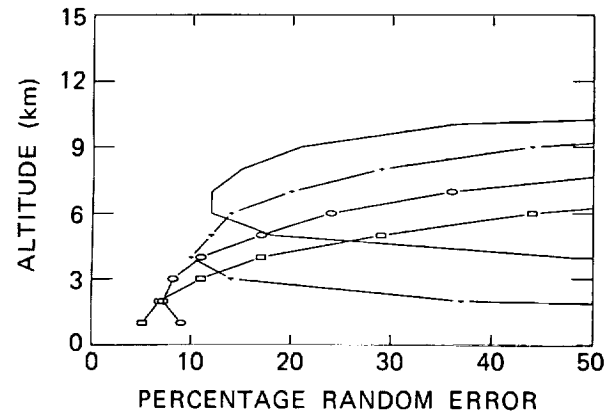

Figure 17. LASA water vapor DIAL range-resolved measurement simulations. Variations with line strength (day filter (0.1 Å); mid-latitude (summer) water vapor; albedo = 0.3). Other parameters as in Figure 15. Water vapor line absorption cross sections ($\Delta\sigma$):
——— 90.1 × 10^{-24} cm², ·—·—· 40.0 × 10^{-24} cm², ○—○—○ 19.5 × 10^{-24} cm², □—□—□ 10.0 × 10^{-24} cm².

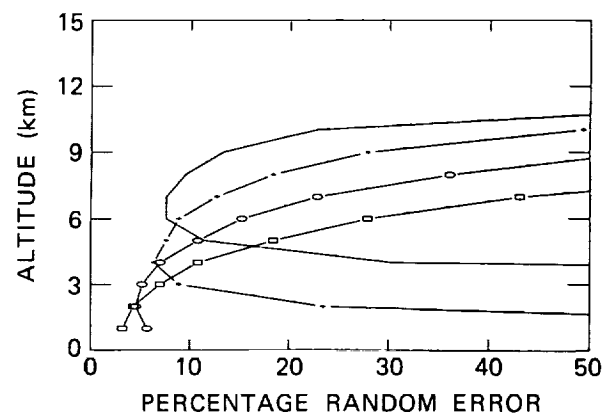

Figure 18. LASA water vapor DIAL range-resolved measurement simulations. Variations with line strength (day filter (0.1 Å); mid-latitude (summer) water vapor; albedo = 0.3). Calculations performed for: λ_{on} = 727 nm, 500 mJ pulse at 10 Hz, Δz = 1,000 m, Δx = 100 km. Water vapor line absorption cross sections ($\Delta\sigma$):
——— 90.1 × 10^{-24} cm², ·—·—· 40.0 × 10^{-24} cm², ○—○—○ 19.5 × 10^{-24} cm², □—□—□ 10.0 × 10^{-24} cm².

Wall. This result was confirmed with simultaneous *in situ* aircraft measurements.

An Alternative Measurement Approach

Total column-content water vapor can be measured through a cw carbon dioxide laser differential absorption approach. The cw carbon dioxide laser water vapor measurement instrument could meet the Eos two-year lifetime requirement with 100 percent duty cycle operation, assuming only that a relatively small-scale lifetime testing program is supported. The instrument would be able to measure water vapor column-content abundances over land and water, day or night, with 10 km horizontal resolution along the suborbital track. The measurement accuracy would be in the 5 to 10 percent range. Water vapor measurements are valuable for radiative transfer and energy budget calculations. Often these applications can make use of data based on sampling of several geographical regions around the globe in a period of 1 to 10 days. Coverage rate can be improved by using scanning lidar.

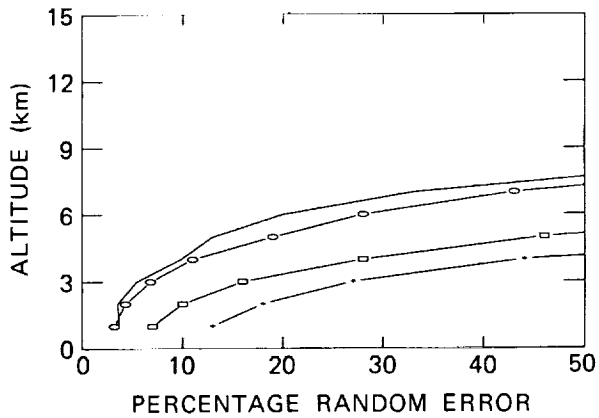

Figure 19. LASA water vapor DIAL range-resolved measurement simulations. Latitudinal variations (day filter (0.1 Å); $\Delta\sigma$ = 10.0 × 10^{-24} cm²; albedo = 0.3; Δz = 250 km). Other parameters as in Figure 16. Latitudinal bands and seasons as follows: ——— tropical, ○—○—○ mid-latitude (summer), □—□—□ mid-latitude (winter), ·—·—· subarctic (winter).

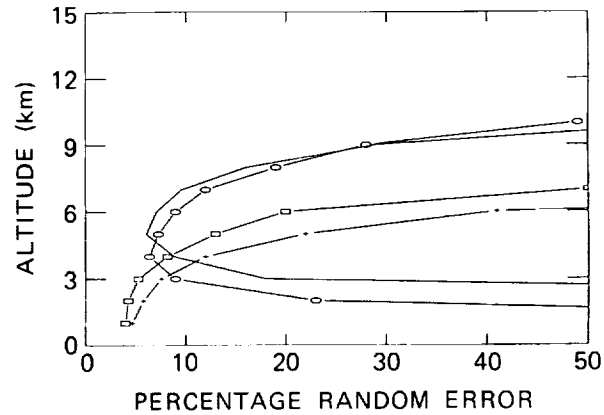

Figure 20. LASA water vapor DIAL range-resolved measurement simulations. Latitudinal variations (day filter (0.1 Å); $\Delta\sigma$ = 40.0 × 10 ^{24} cm²; albedo = 0.3). Other parameters as in Figure 19. Latitudinal bands and seasons as follows: ——— tropical, ○—○—○ mid-latitude (summer), □—□—□ mid-latitude (winter), ·—·—· subarctic (winter).

The measurement of water vapor depends on the existence of several water vapor absorption lines in the 850 to 1,100 cm^{-1} region where many carbon dioxide laser wavelengths exist. The measurements of differential absorption would be made by simultaneously transmitted co-linear radiation from two cw carbon dioxide lasers, one wavelength tuned to overlap with a water vapor absorption feature, and the other chosen to interact minimally with water vapor. To avoid atmospheric carbon dioxide absorption (due to the "hot bands" of atmospheric carbon dioxide that are the same as the laser bands) rare isotopes of carbon dioxide would be used in the laser gas mixes.

Figure 22 is a water vapor volume mixing ratio profile for a U.S. Standard Atmosphere. (This shows that most of the water vapor occurs in the lower 5 km, and, in fact, usually drops off rapidly above the boundary layer.) Using this model, synthetic spectra have been computed for one-way vertical transmission through the atmosphere for a number of spectral regions. Figure 23 shows the 925 to 933 cm^{-1} region. Most of the absorption lines shown are due to water vapor. (Those at 927, 931, and 933 cm^{-1} are isolated carbon dioxide lines.) The R(20) line of the $^{13}C^{16}O_2$ laser overlaps a weak water vapor line and can be used for water vapor column-content measurements in wet regions, such as subtropical or mid-latitude summer conditions. Other laser line frequencies are indicated with vertical marks, using the notation that 636, for example, is a carbon dioxide molecule with two ^{16}O atoms and a ^{13}C atom. (The normal isotope would be 626.) Figure 24 shows the transmission in the 997 to 999 cm^{-1} region. The P(22) line of the $^{13}C^{16}O_2$ laser (high-frequency band) overlaps with a moderately strong water vapor line, which appears as a relatively broad feature between two narrow ozone lines. Most of the sharp, narrow lines shown in this region are due to stratospheric ozone. (The typical ozone line half-widths are approximately 0.05 cm^{-1}.) Several other overlaps have been identified, allowing for measurements to be made over a wide variety of atmospheric moisture conditions just by tuning each laser to a few selected lines.

Measurement Simulations

The instrument characteristics and the assumptions used in deriving the instrument parameters to meet the measurement objectives are described in the following paragraphs. Using the standard lidar equation shown earlier, where the volume backscattering coefficient is replaced by the factor $(\rho \cos \Theta)/\pi$, where ρ/π is the collinear Bidirectional Reflectance Distribution Function (BRDF) and Θ is the angle of incidence of the radiation relative to the local normal to the surface, we can compute the expected return power and compare it with the Noise Equivalent Power (NEP) of the heterodyne receiver. NEP is given by NEP = $(h\nu/\eta^2)(B_{IF}/\tau)^{1/2}$ where η is the detector quantum efficiency, $h\nu$ is the laser radiation photon energy, B_{IF} is the resolving bandwidth of the receiver, and τ is the integration time. We can achieve a detected SNR of 100, sampling over 10 km along-track segments, with the set of system parameters given in Table 13, for the water vapor column abundance measurement.

It is assumed that the receiver would contain a minimum of 10 filter channels, each 250 kHz bandwidth, with 50 percent overlap. These system parameters are consistent with a speckle averaging efficiency that would allow for a 1 percent minimum

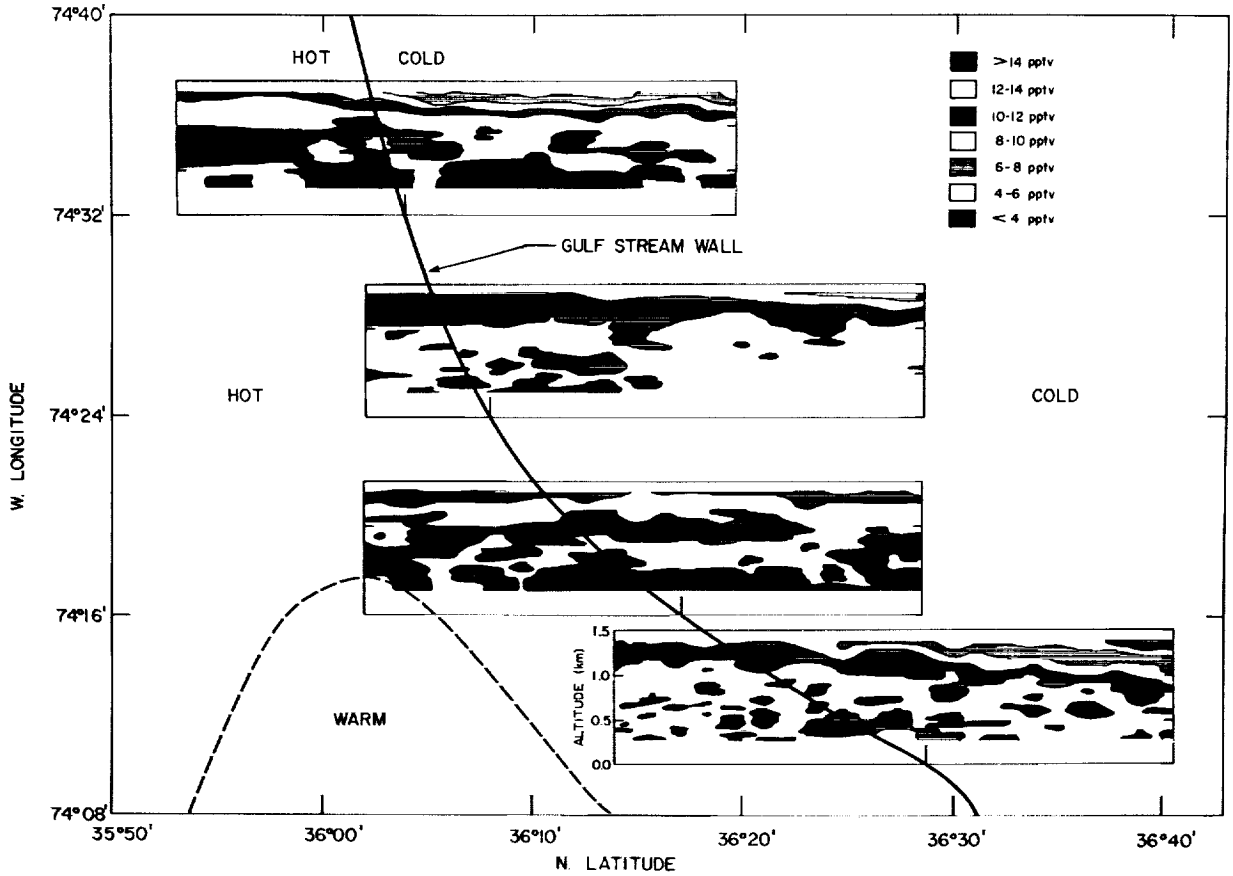

Figure 21. Airborne DIAL measurement of water vapor distribution in Gulf Stream region.

detectable differential absorption. Independent speckle lobe sampling would occur every 1 m of along-track motion, resulting in an average of over 10^4 samples in a 1.5 sec integration time.

Measurement Example

Using various common model atmospheres (McClatchey *et al.*, 1972), measurement accuracies have been computed using a number of spectral overlaps of atmospheric water vapor lines with certain laser lines of the $^{13}C^{16}O_2$ isotope carbon dioxide lasers. The absorption cross sections for these water vapor line overlaps range from 4×10^{-24} cm^2 to 2.5×10^{-23} cm^2. Table 14 lists simulation results, indicating percentage measurement errors for four atmospheric models that cover the range from warm, humid conditions to cold, dry conditions. These measurement errors do not include spectral line parameter inaccuracies and assume that the atmospheric temperature profile for the region from surface to 8 km altitude is known to within ± 3 K. The spectral line parameters at present are at a level of uncertainty such that this would contribute an additional 5 to 10 percent error; however, the appropriate spectroscopic studies can reduce this source of inaccuracy to the 2 to 4 percent level.

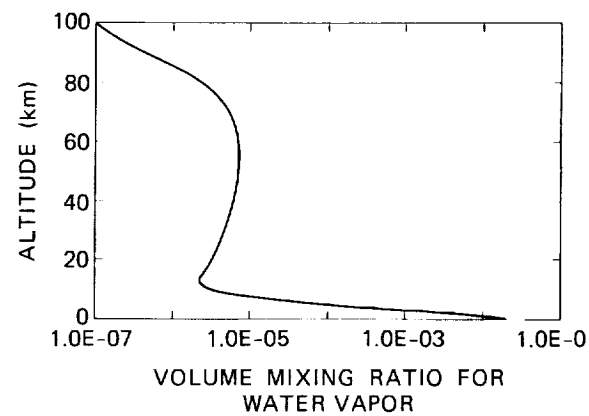

Figure 22. Volume mixing ratio profile for water vapor U.S. Standard Atmosphere.

These simulations include the water vapor continuum absorption expected for each atmospheric model. The simulation results indicate that the intrinsic instrument measurement accuracy would be better than 5 percent under a wide variety of circumstances. In each case, the "off-line" wavelength would be selected to minimize the wavelength

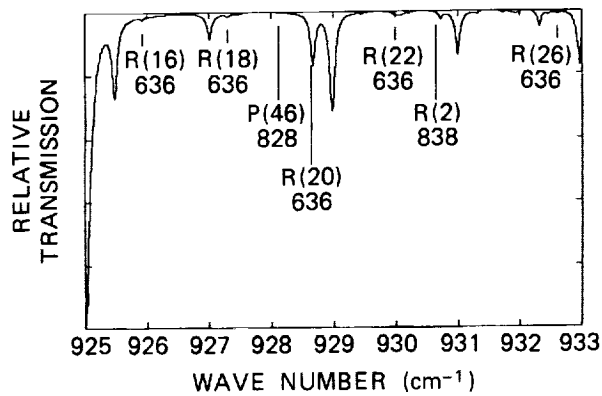

Figure 23. One-way relative vertical transmission spectrum through the Earth's atmosphere (U.S. Standard Atmosphere) from 925 to 933 cm^{-1}. Laser lines which can be obtained with rare isotope versions of carbon dioxide are noted with tic marks. Lines due to standard isotope carbon dioxide appear at 927, 929, 931, and 933 cm^{-1}. The remaining lines are water vapor features, including one which is blended with the 929 cm^{-1} carbon dioxide line.

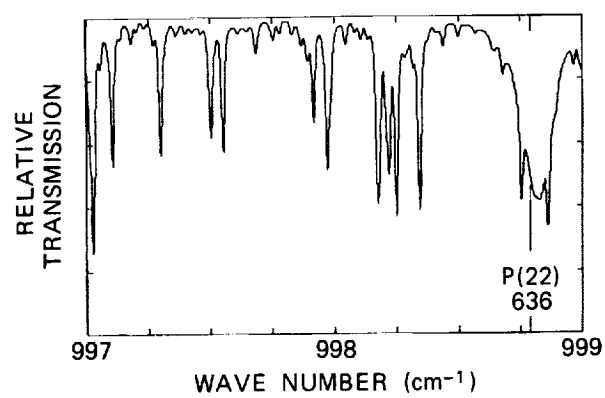

Figure 24. One-way relative vertical transmission through the Earth's atmosphere (997 to 999 cm^{-1}). The P(22) carbon dioxide laser line (with the ^{13}C and ^{16}O isotopes) at 998.77 cm^{-1} is noted with a tic mark, and overlaps with a strong water vapor line.

separation, and the wavelengths would be in the 10 to 11 μm region in order to minimize the silicate Reststrahlen band and other differential reflectance effects that occur mainly in the 9 to 10 μm region. (It is estimated that the residual spectral reflectance fluctuations would add a 5 percent measurement error over land, and would add negligible error over water.)

A cw carbon dioxide laser system employing heterodyne detection has been developed and flown for measurements of water vapor column content (see Figure 25) (Englisch *et al.*, 1983).

ATMOSPHERIC PRESSURE OBSERVATIONS

The pressure field is one of the fundamental variables used for weather prediction and atmospheric circulation studies. Surface pressure and 500 mb heights are used by meteorologists and other atmospheric scientists to describe the state of the atmosphere to define frontal characteristics, and to determine mass movement. The three-dimensional pressure field is also a principal variable used in general circulation models for mid-range and long-range forecasting. It may be noted that the pressure profile can be used directly to specify both the temperature profile and the balanced wind. In contrast, the derivation of a pressure profile from a temperature profile is not possible without specifying pressure at a reference height.

Lidar provides the only remote-sensing technique for the direct measurement of the pressure profile. In addition, it also provides the only remote-sensing technique for measuring surface pressure over both land and ocean surfaces. Moreover, the lack of an accurate pressure reference level hinders the derivation of pressure profiles from radiometrically sensed temperature profiles. As a result, measurements of the pressure profile are available only at radiosonde locations and where satellite

Table 13. Summary of Carbon Dioxide Laser Differential Absorption Spectrometer Parameters

Parameter	Value
Altitude	700 km
Optical Receiver Mirror Area	1 m^2
Laser Transmitter Power	5 W (2 lasers, 10 W total)
Optical Efficiency	0.4
Photomixer Heterodyne Quantum Efficiency	0.4
Surface "Reflectance" (ρ/π)	0.005 (worst case)
Two-Way Path Transmission	0.3 (including water vapor continuum)
Receiver Bandwidth	250 KHz
Integration Time	1.5 sec

Table 14. Water Vapor Measurement Accuracy Based on Model Simulations

Model	Column Abundance (g/cm^2)	Laser Line Wave Number (cm^{-1})	Differential Cross Section (cm^2)	Accuracy (%)
Tropical	5.2	928.656	3.2×10^{-24}	2.5
Mid-latitude Summer	3.7	928.656	2.9×10^{-24}	2
Mid-latitude Winter	1.05	998.788	14×10^{-24}	3
Subarctic Winter	0.48	948.308	4.1×10^{-23}	1.5

temperature profiles and a surface pressure measurement coincide.

Measurement Approach for Surface Pressure

This experiment will accurately determine surface pressure over land and ocean regions of the globe for both day and night operation. In areas with low-lying clouds, the pressure and altitude of the clouds will be measured; this measurement can be used to derive surface pressure.

The surface pressure experiment is a two-wavelength DIAL measurement (Korb and Weng, 1983) utilizing the backscattered energy from the Earth's surface or from low-lying clouds. The measurements can be made in either a crosstrack scanning or nadir-viewing mode, depending upon availability of a scanning configuration. Only modest laser energy is required since the backscattered signals are large. A pressure-sensitive measurement is obtained by locating one wavelength in a temperature insensitve absorption trough region. A trough region is the region of minimum absorption between two strongly absorbing lines in the oxygen A-band near 0.76 μm, or 13,150 cm^{-1}. The absorption in the trough is proportional to the square of the pressure. A second wavelength located in a weakly absorbing region with a shift of 0.0001 to 0.001 μm is used as a reference to normalize out the effects of surface

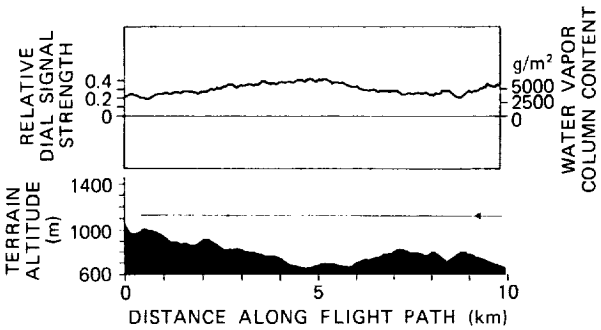

Figure 25. Water vapor column content measured using the Differential Absorption Lidar Experiment (DIALEX) (cw carbon dioxide laser system) (Englisch *et al.*, 1983).

reflectance. The use of an absorption trough technique reduces the sensitivity of the measurements to the effects of laser frequency jitter by up to two orders of magnitude. The integrated path absorption method used for the measurement allows high sensitivity to be achieved.

Measurement Simulations

A two-wavelength solid-state Alexandrite laser tunable over the 0.76 μm region is assumed. It has a spectral resolution of 0.02 cm^{-1} or better, a pulse length of less than 100 ns, and an energy of 0.1 to 0.5 J/pulse is used for the measurement. The two wavelengths are separated in time by a nominal 300 μs, which allows temporal separation and single-channel detection of both the on-line and reference wavelengths. An energy monitor is needed to measure the transmitted laser energy at each wavelength and a wavemeter must be used to precisely measure and control the laser wavelength.

The atmospheric model used for the simulations is a one-dimensional model with up to 50 homogeneous vertical layers. The temperature and pressure data are taken from the mid-latitude January U.S. Standard Atmosphere model and the aerosol composition data are taken from the Elterman model (Elterman, 1968). The simulations were performed using a high spectral resolution atmospheric transmission code. The transmission at a given frequency is calculated using the Voigt line profile and integrated vertically over the layers from space to altitude z. The simulations include detailed calculations of laser finite bandwidth. The effects of background radiation on the simulations have been considered. These include surface reflectance, aerosol scattering, and Rayleigh scattering.

The simulations used the following parameters for measurements from a 700 km Eos platform. A 0.5 J Alexandrite laser transmitter with a repetition rate of up to 10 Hz, a three-mode spectral output with a bandwidth of 0.02 cm^{-1}, a telescope diameter of 1.25 m, a receiver field-of-view (FOV) of 0.15 (0.5) mrad for daytime/nighttime experiments, and a surface reflectance of 0.1. An optical efficiency of 0.59 was used for nighttime simulations, which includes the transmission of a wide-band 20 Å spectral detection filter, and an optical efficiency of 0.38 was

used for daytime simulations, which includes the additional narrow-band (1.6 or 5 cm^{-1}) filters required. A quantum efficiency of 0.15 is assumed for the detector. The detailed parameters for nighttime and daytime experiments are given on the attached figures with the overall efficiency for each experiment. Figures 26 and 27 give the results of simulations for a crosstrack scanning experiment to measure surface pressure using the pressure-sensitive trough absorption at 13,150.86 cm^{-1}. The figures give the number of shots required to achieve 0.2 percent surface pressure accuracy versus scan angle for nighttime and daytime measurements with a 250 km grid. As shown, a 2.9 Hz repetition rate is sufficient for nighttime measurements and 4.5 Hz is sufficient for daytime measurements. For a nadir experiment, the required laser energy could be reduced by a factor of four and still achieve these

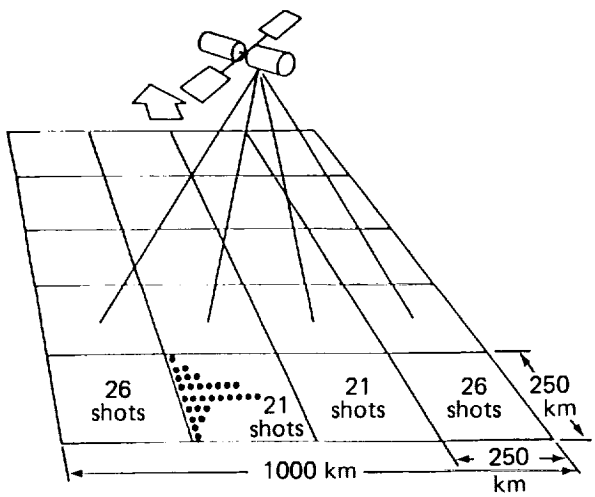

Figure 26. Surface pressure scanning lidar simulated for Eos experiment at 700 km—night. Calculations performed for: 500 mJ pulse at 2.9 Hz, ν = 13,150.86 cm^{-1} or (13,152.49 cm^{-1}), $\Delta\nu$ = 0.02 cm^{-1}, 3-mode laser, D = 1.25 m, $\Delta P/P$ = 0.02%, eff. = 0.0885, FOV = 0.5 mrad, $\Delta\lambda_F$ = 20 Å, ρ = 0.1.

accuracies. We note that for cloud-top pressure altitude measurements, an accuracy of 0.2 percent or better could be obtained with approximately one-fifth the laser power factor.

Measurement Approach for the Pressure Profile

LASA can also accurately determine the pressure profile–the pressure and altitude structure of the atmosphere over land and ocean regions of the globe for both day and night operation.

The pressure profile experiment is a two-wavelength DIAL measurement utilizing the backscattered energy from the clear atmosphere. In a man-

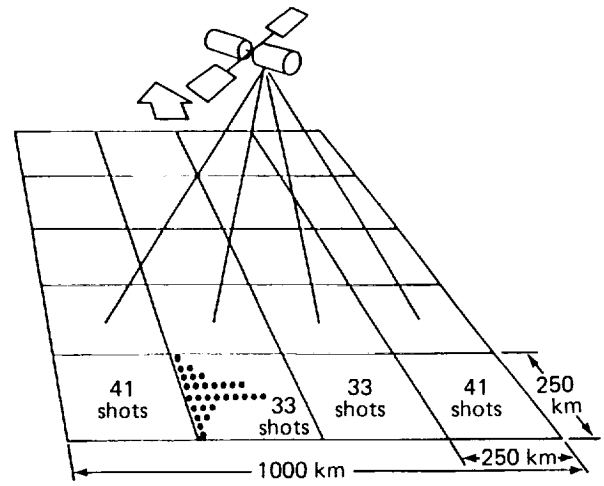

Figure 27. Surface pressure scanning lidar simulated for Eos experiment at 700 km—day. Calculations performed for: 4.5 Hz pulse rate, eff. = 0.057, FOV = 0.15 mrad, $\Delta\lambda_F$ = 1.6 cm^{-1} or (5 cm^{-1}), ρ = 0.3. Other parameters as in Figure 26.

ner similar to the surface pressure measurements, a pressure-sensitive measurement is obtained by locating one wavelength in an absorption trough region in the oxygen A-band near 0.76 μm or 13,150 cm^{-1}. A second wavelength located in a weakly absorbing region is used as a reference to normalize out the effects of atmospheric backscatter. The absorption trough technique greatly reduces the sensitivity of the measurements to the effects of laser frequency jitter, and the integrated path absorption method allows high sensitivity to be achieved.

Measurement Simulations

The instrument characteristics required are similar to those given for surface pressure, again using a two-wavelength tunable solid-state laser. Higher energy, 0.5 J/pulse, is needed for the profiling measurement. The profiling measurements, however, do not require an energy monitor measurement.

The basic atmospheric model used for these simulations is similar to that used for surface pressure. The laser transmitter assumed for the simulations is an Alexandrite laser with a three-mode spectral pattern with a bandwidth of 0.02 cm^{-1}. The simulations include detailed calculations of laser-finite bandwidth. The effects of background radiation on the simulations have been considered. These include the effects of surface albedo, aerosol scattering, and Rayleigh scattering.

The pressure profile simulations used almost the same parameters as those used for surface pressure. Differences were the use of a wide-band 10 Å spectral detection filter for nighttime and a narrow-band 0.12 cm^{-1} filter for daytime simulations. Also, a quantum efficiency of 0.2 is assumed for the

detector. The detailed parameters for nighttime and daytime experiments are given on the attached figures with the overall efficiency for each experiment.

Figures 28 and 29 show the results of simulations of pressure profiling for a nadir-viewing experiment. As shown, for 1 km vertical and 250 km horizontal resolution, good accuracy (<0.4 percent) can be obtained over a large portion of the troposphere using the pressure-sensitive absorption troughs located at either 13,150.86 or 13,153.79 cm^{-1}. We note that the use of a 0.15 mrad FOV and a 0.12 cm^{-1} spectral detection filter minimizes the effects of background radiation and allows high-accuracy daytime measurements.

Measurement Example

The atmospheric pressure profile has been measured from both ground-based (Schwemmer, 1984) as well as aircraft platforms (Korb *et al.*, 1986). An example of a comparison of aircraft lidar measurements of the pressure profile with radiosonde measurements is shown in Figure 30. The lidar system used two high-resolution Alexandrite lasers (0.02 cm^{-1} resolution) tuned to an absorption trough and a reference wavelength near 760 nm. The measurements were made from the NASA Electra aircraft at an altitude of 2,790 m, approximately 220 km off the coast of Delaware during the nighttime of November 20, 1985. The lidar measurements were made with a 30 m vertical resolution and analyzed for a 100 shot average. The average deviation between the lidar and radiosonde data was less than 0.2 percent (2 mb).

ATMOSPHERIC TEMPERATURE PROFILE OBSERVATIONS

The temperature field is of fundamental importance in meteorology, climate, and for initializing global circulation models for all scales of weather forecasting. Temperature profiles are required for determining tropopause height, tropopause breaks, the depth and structure of the planetary boundary layer, and frontal and air mass characteristics, as well as numerous other meteorological phenomena. In the mid- and high-latitudes, temperatures are of added importance since over oceanic areas in these latitudes wind fields are derived from temperature fields using balance relationships.

General circulation models have now developed to the point where data at as many as seven independent tropospheric levels are required. The most advanced passive sounders currently under study cannot accurately provide vertical resolution at this scale.

Lidar differential absorption measurements can provide direct measurements of the temperature profile with extremely high vertical resolution. The use of the lidar technique will allow the temperature

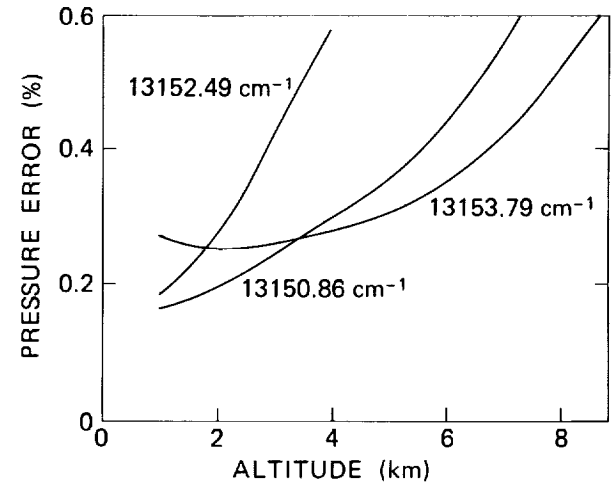

Figure 28. Pressure profiling accuracy for simulated Eos experiment at 700 km—night. Calculations performed for: 500 mJ pulse at 10 Hz, $\Delta\nu$ = 0.02 cm^{-1}, 3-mode laser, D = 1.25 m, eff. = 0.118, Δx = 250 km, Δz = 1 km, FOV = 0.5 mrad, $\Delta\lambda_F$ = 10 Å, ρ = 0.1.

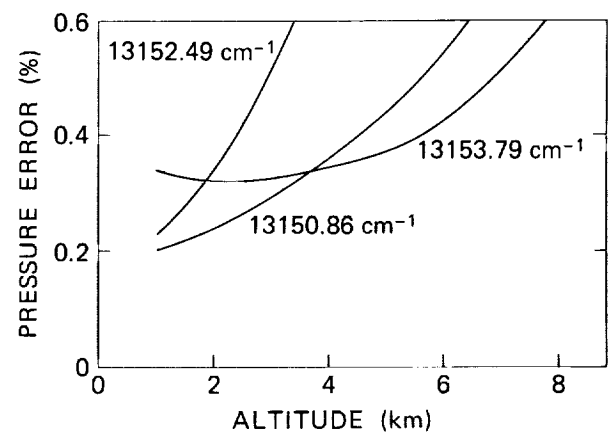

Figure 29. Pressure profiling accuracy for simulated Eos experiment at 700 km—day. Calculations performed for: eff. = 0.076, FOV = 0.15 mrad, $\Delta\nu_F$ = 0.12 cm^{-1}. Other parameters as in Figure 28.

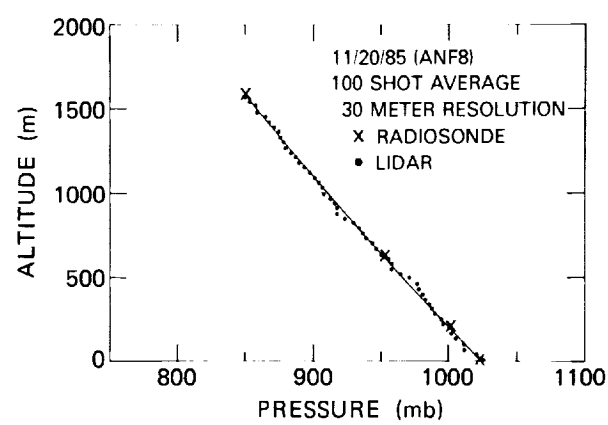

Figure 30. Lidar measurements of atmospheric pressure profile as a function of altitude (aircraft – 2,790 m).

to be measured in a direct manner, rather than requiring the use of inversion techniques as must currently be done in order to use the data from passive profilers. The simulations below indicate that a lidar temperature profile experiment could achieve 1 K temperature accuracy while simultaneously obtaining 1.25 to 2.5 km vertical resolution.

Measurement Approach for the Temperature Profile

LASA can accurately determine the atmospheric temperature profile over land and ocean regions of the globe for both day and night operation.

The temperature profile measurement uses a two-wavelength DIAL technique (Korb and Weng, 1982) utilizing the backscattered energy from the clear atmosphere. The measurement is made in a differential ranging mode to obtain vertical resolution. A measurement highly sensitive to temperature is obtained by locating one wavelength on a high j line in the oxygen A-band near 0.77 μm, or 13,000 cm^{-1}, where the variation of absorption coefficient with temperature is as high as the sixth power of temperature. A second wavelength located in a weakly absorbing region with a shift of 0.02 to 0.5 nm is used as a reference to normalize out the effects of atmospheric backscatter.

Measurement Simulations

The instrument characteristics for temperature profiling are the same as those given for pressure profiling. Also the return signals are measured with a nominal 100 m range cell. The atmospheric model and the laser transmitter used for these simulations are the same as those used for the surface pressure and pressure profile experiment.

The simulations used the same parameters as those used for pressure profiling: a 0.5 J Alexandrite laser transmitter with a repetition rate of 10 Hz, a three-mode spectral output with a bandwidth of 0.02 cm^{-1}, a telescope diameter of 1.25 m, and a receiver FOV of 0.15 (0.5) mrad for daytime (nighttime) experiments. An optical efficiency of 0.59 was used for nighttime simulations, which includes a wide-band 10 Å spectral detection filter, and an optical efficiency of 0.38 was used for daytime simulations, which includes a narrow-band 0.12 cm^{-1} filter. A quantum efficiency of 0.2 is assumed for the detector. The detailed parameters for nighttime and daytime experiments are given on the attached figures with the overall efficiency for each experiment.

Figures 31 to 33 show the results of simulations of temperature profiling for a nadir-viewing experiment. As shown for the line at 12,999.95 cm^{-1}, 2.5 km vertical resolution allows high-accuracy measurements with less than 1 K error for altitudes up to 10 km. In addition, the use of the stronger absorption line at 13,010.81 cm^{-1} with 3 km resolution allows high-accuracy measurements to be extended to 15 km altitude. The horizontal resolution is 175 km for nighttime and 250 km for daytime measurements. The effects of background are small for the

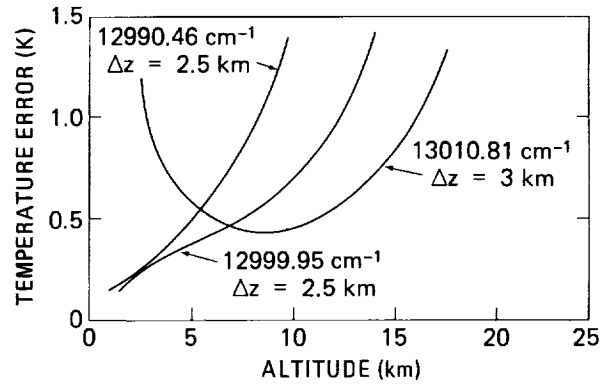

Figure 31. Temperature accuracy for simulated Eos experiment at 700 km—night. Calculations performed for: Δx = 175 km. Other parameters as in Figure 28.

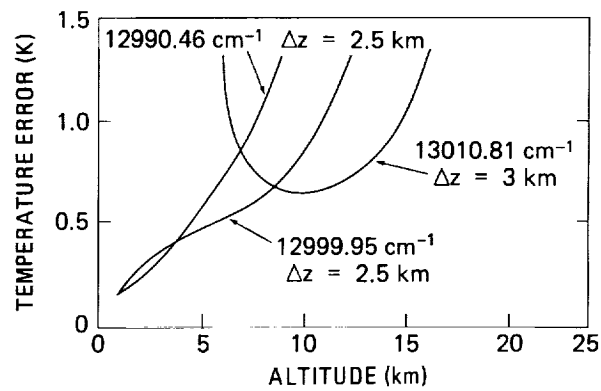

Figure 32. Temperature accuracy for simulated Eos experiment at 700 km—day. Parameters as in Figure 29.

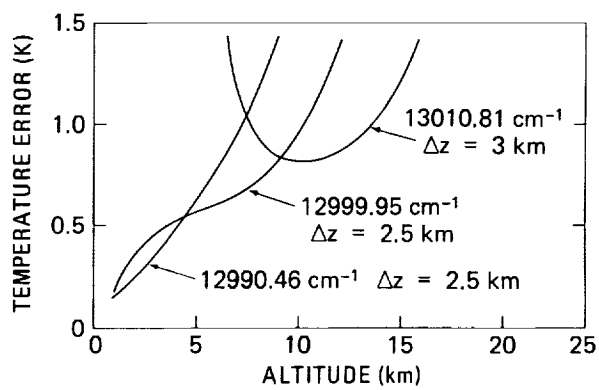

Figure 33. Temperature accuracy for simulated Eos experiment at 700 km—day. Calculations performed for ρ = 0.3. Other parameters as in Figure 29.

12,999.95 cm^{-1} measurement but become significant for the 13,010.81 cm^{-1} measurement.

Figures 34 to 36 show the results of temperature profiling accuracy simulations for a 1.25 km vertical resolution nadir-viewing experiment. As shown, high temperature accuracy and high vertical resolution can be obtained in the lower portion of the troposphere.

Measurement Example

Differential absorption measurements of atmospheric temperature have been made over a 1 km horizontal atmospheric path to better than 1 K using an ultrahigh spectral resolution cw dye laser system (Kalshoven *et al.*, 1981). Recently, range-resolved differential absorption lidar measurements were made with a ground-based upward-viewing lidar system (Korb *et al.*, 1985). The system used dual high-resolution Alexandrite lasers with a spectral resolution of 0.02 cm^{-1}. The measurements were made over the altitude range from 800 to 2,700 m. For a 300 m vertical resolution and a 300 shot average, the accuracy was better than 2 K.

OZONE OBSERVATIONS

The ozone layer determines the ultraviolet transmission properties of the atmosphere. The amount of ultraviolet radiation reaching the surface of the Earth has direct effects on living systems. Ozone is formed in the stratosphere by ultraviolet photolysis of oxygen, and some ozone is transported from the stratosphere providing one source of tropospheric ozone. Ozone is a key compound in the atmospheric chemistry of trace constituents. Ozone in the troposphere is an oxidant directly affecting the surfaces of living organisms. A global data base, sufficient to produce a coarse resolution ozone climatology, is needed for the field of tropospheric chemistry. It would enable production of a

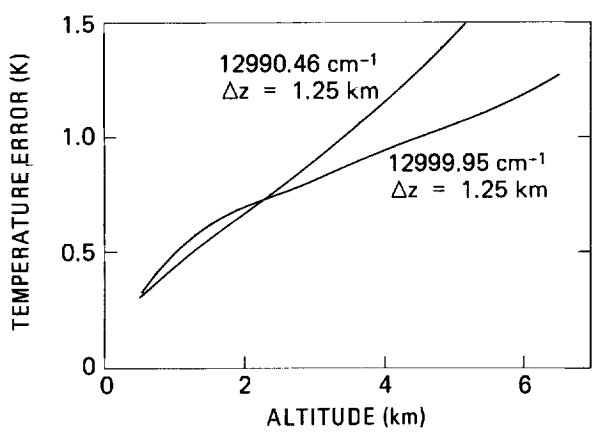

Figure 34. Temperature accuracy for simulated Eos experiment at 700 km—night. Calculations performed for ρ = 0.3. Other parameters as in Figure 31.

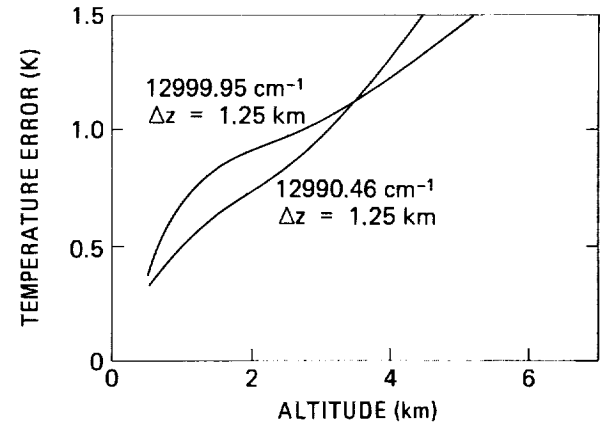

Figure 35. Temperature accuracy for simulated Eos experiment at 700 km—day. Parameters as in Figure 29.

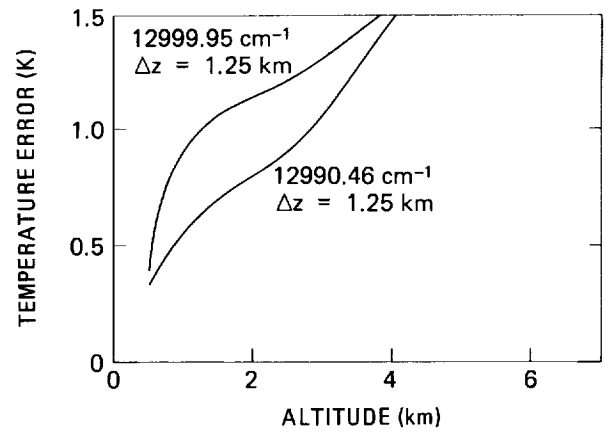

Figure 36. Temperature accuracy for simulated Eos experiment at 700 km—day. Calculations performed for ρ = 0.3. Other parameters as in Figure 29.

global distribution of hydroxyl radical, the principal oxidizing species in the various elemental cycles, and it would also provide a framework for tropospheric photochemistry as a whole. Due to the high variability of ozone in the troposphere, relative standard deviations in the range of 25 to 100 percent, a realistic global data base will require relatively high spatial and temporal resolution, which can best be obtained from an orbiting laser DIAL measurement of global ozone profiles.

There is a continuing concern that the total column and vertical distribution of atmospheric ozone will be affected by changing concentrations of a number of trace species such as chlorofluorocarbons, carbon dioxide, oxides of nitrogen, and methane. If ozone were to be seriously depleted by these compounds, increased amounts of solar ultraviolet radiation would be allowed to reach the ground and could have serious impact on human health and agricultural and oceanic productivity. The ozone absorption of solar energy also provides the main

source of heating for the middle atmosphere; without it there would be no middle atmosphere. Thus, the measurement of the vertical distribution of ozone is important in determining the temperature structure and dynamics of the middle atmosphere. The distribution of ozone is also critical in determining connections between stratospheric and tropospheric weather and climate that can occur through radiative, dynamical, and chemical mechanisms.

Both the Dobson network and satellite observations (Solar Backscatter Ultraviolet (SBUV) and Total Ozone Mapping Spectrometer (TOMS)) provide a global field of total ozone measurements. Unfortunately, approximately 90 percent of the total ozone resides in the stratosphere, and existing techniques are not able to accurately measure the small fraction that resides in the troposphere. It has not been possible to use these two existing passive methods for trend analysis of ozone. This has been in part due to lack of precision in these techniques and drift in their calibrations. For example, the Nimbus 4 Backscattered Ultraviolet (BUV) total ozone data show a drift of about 0.5 percent per year relative to the ground-based measurements. This instrument also showed wavelength-dependent drifts in radiance data. These instrument artifacts are sufficiently large to overwhelm trends of the size predicted for chlorofluorocarbon chemistry-induced ozone destruction. The longest data base available for altitude-resolved ozone measurements is that from the Umkehr measurements, which provide vertical ozone profiles up to 48 km. Derivation of ozone profiles from Umkehr data requires an indirect inversion method and suffers from limited vertical resolution and nonuniqueness of the profiles, and the absence of simultaneous measurements of aerosols and other factors which affect the inversion.

The best existing tropospheric ozone data set is provided by individual ozonesonde stations that are now measuring or have measured vertical profiles of ozone from the ground to the middle stratosphere on a more-or-less regular basis. Unfortunately, a number of different types of sensors have been used, many of which were never accurately intercalibrated. Serious doubts have recently been raised about the absolute accuracy of the ozonesonde measurements in the troposphere particularly for the older types of sondes that are no longer in operation or available for intercomparisons with current devices. Previous intercomparisons of operational devices alone have raised serious doubts about combining measurements from different research groups or devices into a single data set.

Three key issues involving atmospheric ozone concentrations are to determine: (1) the climatology of ozone (i.e., the concentration distribution including mean values and higher moments); (2) the process or combination of processes that exert dominant control on ozone climatology; and (3) the possible existence of long-term changes in the mean and extremes of concentration, and the causes of such trends if they do exist.

Measurement Approach for Ozone Profiles

A satellite lidar system using the ultraviolet DIAL measurement method based on the XeCl excimer laser is a promising approach to obtain global profiles at high vertical resolution of both stratospheric and tropospheric ozone. Recent ground-based measurements (Uchino *et al.*, 1979; Werner *et al.*, 1983) of tropospheric and stratospheric ozone profiles using an XeCl excimer-based lidar have demonstrated that precise high-resolution measurements of ozone can be obtained on a routine basis.

The XeCl excimer-based DIAL system for ozone measurements transmits two laser lines in the ultraviolet: one at 308 nm and the other at either 338 or 353 nm. It is straightforward by further Raman shifting to propagate an additional laser line in the visible region at 500 to 600 nm. By using the backscattered return signal from 308 and either 338 or 353 nm, the ozone concentration profiles can be obtained. The backscattered data from 338 or 353 nm is a measure of the Rayleigh (molecular) scattering, and the visible return at 500 or 600 nm provides a measure of the Rayleigh and Mie (aerosol) scattering return. From this data, a density profile of the atmosphere from 10 to 50 km can be calculated and a temperature profile can be extracted from the density profile.

A more precise lidar determination of the tropopause height derived from the Rayleigh and Mie lidar backscattering signals converted to temperature profiles would improve the inversion methods for passive temperature instruments. There is also an important correlation between the tropopause height and total ozone, which can be measured simultaneously using a spaceborne lidar system. For example, when the tropopause height is low, there is little exchange between the tropopause and the stratosphere, and when there is a high tropopause or no tropopause, a jet stream occurs.

In the stratosphere the distribution of ozone is strongly affected by the advection of ozone and energy, which together with vertical motions influence the temperature distribution. The photochemistry of ozone is highly temperature dependent. The motions, in turn, are strongly influenced by radiative sources and sinks of thermal energy, while ozone is the principal absorber of solar radiation in the stratosphere. Chemistry, radiation fields, and dynamics are all closely coupled in the stratosphere. The synergistic lidar measurement of aerosols, temperature, and density along with the ozone profiles will aid in understanding the complex interactions of these processes on ozone concentration.

The XeCl fundamental at 308 nm, and the first Stokes shift in hydrogen at 353 nm, can be used to obtain ozone concentration profiles using the DIAL technique. Since the demands for the laser transmitter are virtually identical for the measurement of ozone profiles or column content, there is no advantage in simplicity in just measuring the column content.

Measurement Simulations

Simulations for ozone profile observations have been calculated using the lidar system parameters listed in Table 15.

of the laser and telescope FOV was unity over the range of 50 to 0 km altitude. The receiver was assumed to have an aperture of 1 m diameter and an overall efficiency of 10 percent. For these preliminary estimations, no attempts were made to include wavelength-dependent parameters such as quantum efficiency, etc. The photon returns, as a function of altitude and range from the observing platform, are shown in Figure 39 for all of the wavelengths that can be easily obtained from the 308 nm output of the XeCl laser by stimulated Raman shifting in hydrogen; and the backscattered return for the 308 nm wavelength, which is absorbed by ozone, is

Table 15. Lidar System Parameters Used for Ozone Simulations

	Day	Night
System Altitude	700 km	700 km
Receiver Clear Diameter	1.0 m	1.0 m
Laser Pulse Energy	1.0 J	1.0 J
Laser Wavelengths	308 nm, 353 nm	308 nm, 353 nm
System Optical Efficiency	10%	10%
Vertical Sampling Resolution	1 km	1 km
Optical Bandwidth	0.2 nm, 0.001 nm	0.2 nm
FOV	0.1 mr, 1 mr	0.1 mr
Albedo	0.1, 0.8	0.8

The basis for the ozone DIAL simulations is the U.S. Standard Atmosphere and the ozone profile is shown in Figure 37. Also required is an aerosol distribution model; that used in these simulations corresponds to a particularly clean atmosphere. It is shown in Figure 38. Scattering cross sections conforming to a Deirmendjian Haze L model were used and these are listed together with the other relevant cross sections in Table 16.

The lidar equation was used to evaluate the magnitude of the return signal. The transmitted beams were each assumed to have an energy of 1 J/pulse and to have a divergence such that the overlap

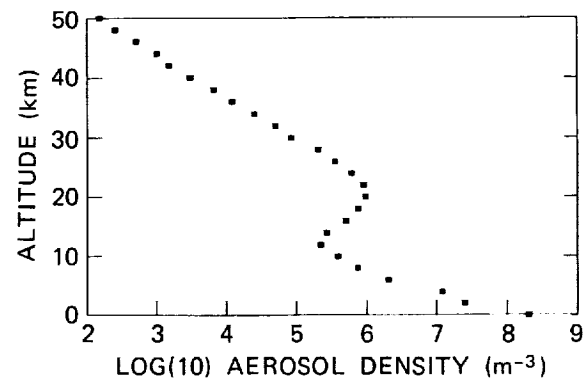

Figure 38. Composite aerosol distribution (Stanford Research Institute model).

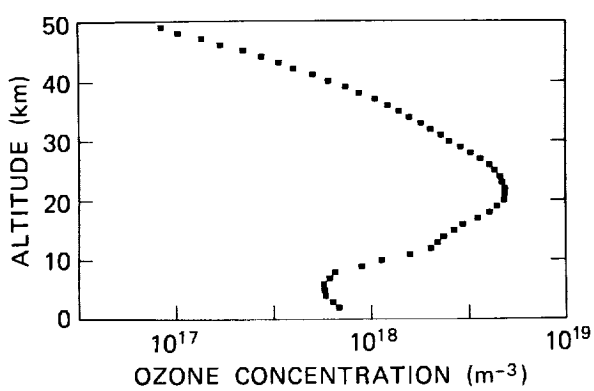

Figure 37. U.S. Standard Atmosphere ozone profile.

shown on an expanded scale in Figure 40. In order to estimate the precision of the measurement, the magnitude of other sources contributing to the observed signal must be considered. By far, the largest of these is the background caused by scattering of solar radiation.

Procedure For Estimating Solar Background

Each of the simulation calculations at wavelengths of 1,064 nm and less requires estimates of

Table 16. Scattering Cross Sections

Scatterer	Wavelength	
	308 nm	353 nm
Ozone	1.28×10^{-19}	2.00×10^{-22} cm^2
Rayleigh	5.54×10^{-27}	3.21×10^{-27} cm^2
Haze L	1.35×10^{-10}	1.10×10^{-10} cm^2

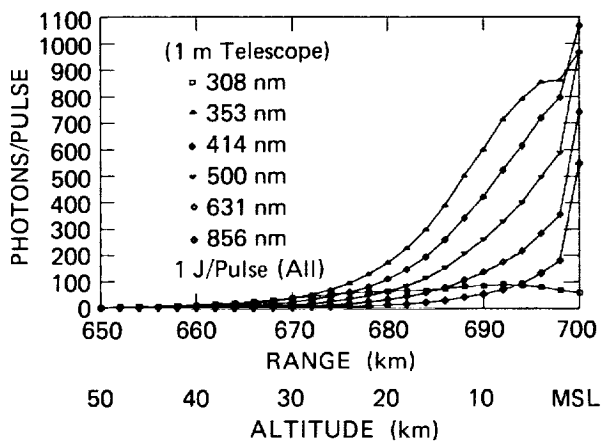

Figure 39. Multiwavelength lidar: signal returns (composite aerosol, Haze Model L).

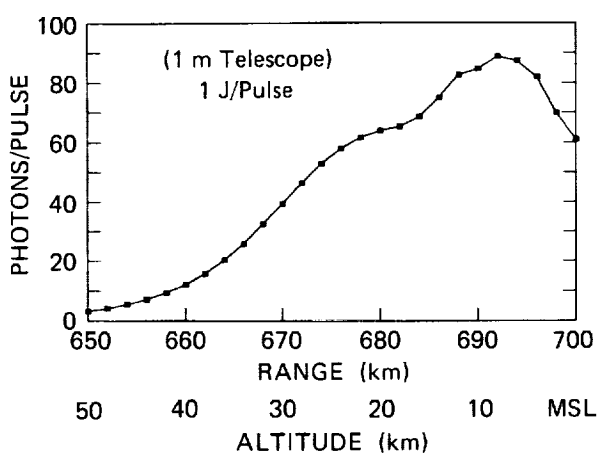

Figure 40. Ozone lidar: signal returns at 308 nm (composite Haze Model L).

backscatter solar radiance. The backscattered solar radiance is directly proportional to the wavelength-dependent solar irradiance. Values given by Thekaekara (1974) may be used for the solar irradiance (I_o) and they are listed in Table 17 for several selected wavelengths.

To a first approximation, it can be assumed that the attenuation by the atmosphere is balanced by the scattered sky radiance. For scattering at the surface, we assume Lambertian scattering such that

$$I(\lambda) = I_o(\lambda)\ \alpha \cos\Theta/\pi$$

where α is the albedo and Θ is the solar angle from zenith. Ignoring any wavelength dependence of the albedo, the typical albedo values for some representative surface conditions are shown in Table 18.

The magnitude of the received background solar radiation is given by:

$$S_{BG} = I(\lambda)\Omega A2\ (\Delta R/c) \int \eta\ (\lambda)\ d\lambda$$
$$\approx I(\lambda)\Omega A2\ (\Delta R/c)\ \eta\ (\lambda)\ \Delta\lambda$$

Note: Ω is the solid angle subtended by the telescope. For small angles,

$$\Omega \approx \pi\ \phi^2/4$$

where ϕ is the full plane angle of the telescope FOV. Thus, the level of background solar radiation detected by the lidar receiver increases with the square of the telescope FOV.

An Example:

Sun at zenith, $\Theta = 0°$, over land, $\alpha = 0.2$, and at 500 nm

$$I(500) = 1{,}947 \times 0.2 \times 1/\pi$$
$$= 124 \text{ mW m}^{-2} \text{ nm}^{-1} \text{ sr}^{-1}$$

Table 17. Solar Irradiance

Wavelength λ (nm)	Irradiance I_o (mW m^{-2} nm^{-1})
308	653
353	787
414	976
500	1,211
532	1,213
631	1,300
724	1,570
760	1,773
856	1,836
1,064	1,947

Table 18. Typical Albedo Values

Surface	Albedo (α)
Fresh Snow	0.9
Cloud	0.8
Old Snow	0.5
Sand	0.25
Soil	0.2
Ocean	0.1

For a telescope with the following characteristics,

FOV 1 mr	$\Omega = 7.85 \times 10^{-7}$ sr
Diameter 1.25 m	$A = 1.25\ m^2$
Range Element 1 km	$\Delta R = 1{,}000$ m
Bandpass 0.1 nm	$\Delta\lambda = 0.1$ nm
Throughput 10 percent	$\eta(\lambda) = 0.1$

the level of solar background actually counted by the detector is 16,000 photons per pulse per range bin. This is unacceptably high for virtually all measurements. There are only two parameters in the receiver system that can be changed to ameliorate this situation. Either the telescope FOV can be reduced or the spectral bandpass of the filter system can be reduced.

The latter solution is not applicable to all lidar systems since some may require a large bandpass to obtain the desired information. Clearly, the only universal solution is to reduce the FOV of the telescope. However, the telescope FOV should normally be somewhat larger than the laser spot size in order to ensure overlap of the FOVs of both the transmitter and receiver systems. In reducing the ground spot size of the laser, the question of whether the laser will still meet eye safety requirements must be addressed.

The computer model follows the error analysis given by Russell *et al.* (1979) and allows variation of the lidar system parameters such as receiver FOV, laser pulse energy and repetition rate, and spectral bandpass of the filter. The position of the sun and the surface albedo can also be varied. For the sun angle, two limiting conditions were used with the sun at zenith for worst-case daytime measurements, and at the horizon for nighttime measurements. The number of pulses that can be averaged to improve the SNR is limited by the horizontal resolution required and by the repetition rate of the laser. While the excimer laser is capable of operation at high repetition rates, up to 1 kHz, the system is limited by the power available on the platform and by lifetime considerations for the laser components. It has been assumed that a rate of 10 Hz will meet these operational restraints. Thus, for a horizontal resolution of 250 km, with a ground-track velocity of 7 km s^{-1}, the maximum number of pulses that can be averaged is 350. This causes severe limitations for stratospheric measurements but does not constrain the tropospheric measurements.

Figures 41 to 45 show the calculated error and the inverted ozone profiles for a number of different conditions, as marked on the figures. As can be seen from these simulations it is difficult to obtain precise concentration measurements above about 30 km for the 250 km horizontal resolution due to the velocity of the satellite and the low pulse rate of the laser. However, good measurements are possible in the lower stratosphere and in the troposphere. For the nighttime measurements the uncertainty is signal limited, and thus only methods to increase either the laser pulse energy or repetition rate will improve this measurement. The incorporation of very narrow bandwidth filters could enable daytime measurements with good SNR, but this increases the complexity of both the laser transmitter and receiver filter.

LIDAR SCANNING

By scanning, greater geographic coverage (left/right of orbit plane) can be obtained between successive orbits, but with the concomitant loss of data along the track for a fixed laser pulse rate.

There is a great desire to enhance the global coverage of LASA measurements through scanning,

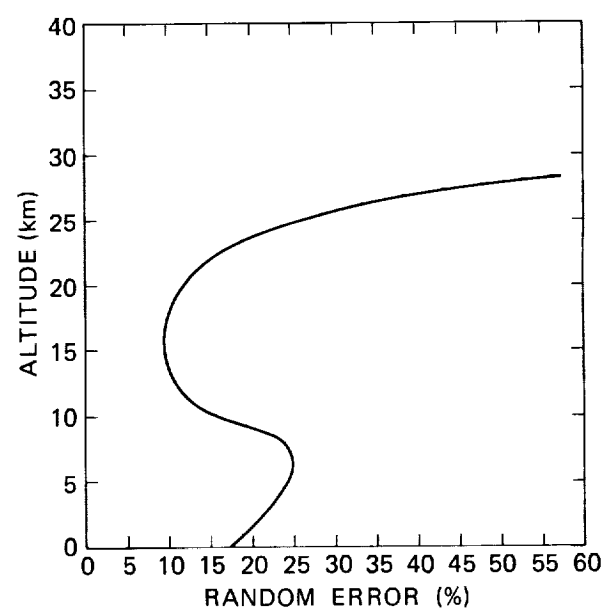

Figure 41. Ozone DIAL precision. Random error only. Does not include systematic errors due to large $\Delta\lambda$ for the two DIAL wavelengths. Calculations performed for: telescope area = 1.23 m^2, FOV = 0.1 mr, solar zenith angle = 0, 1,000 shots, throughput = 10%, albedo = 0.8, filter width = 0.1 nm, Δz = 2 km, pulse energy = 1 J at 308 nm and 0.1 J at 353 nm.

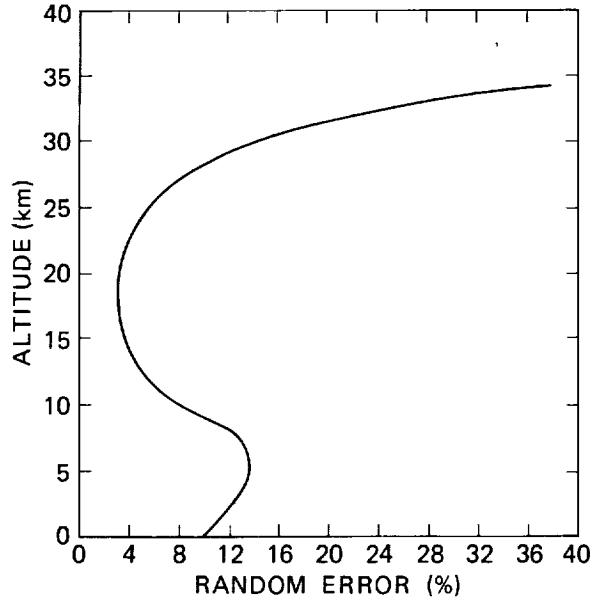

Figure 42. Ozone DIAL precision. Parameters as in Figure 41 except filter width is 0.001 nm.

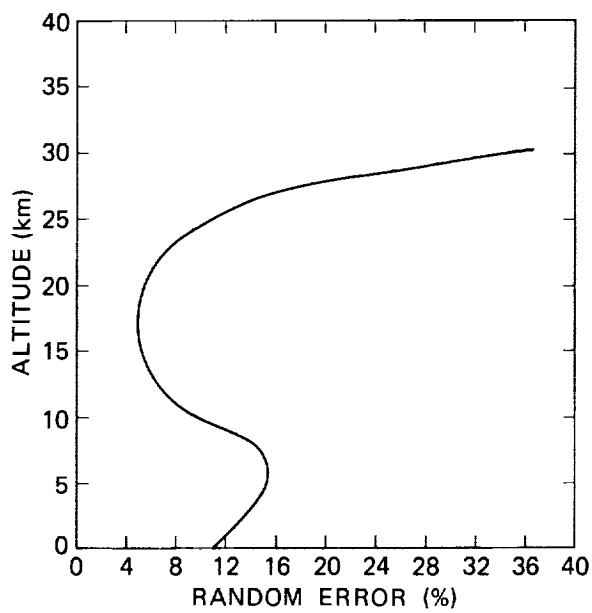

Figure 43. Ozone DIAL precision. Parameters as in Figure 41 except albedo is 0.1.

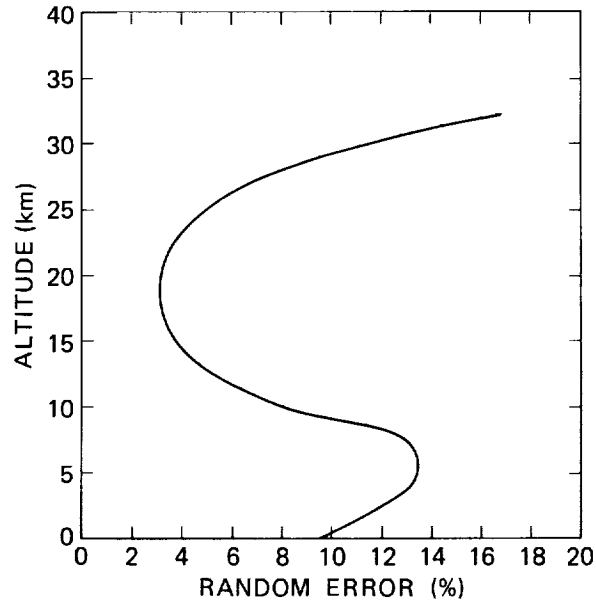

Figure 44. Ozone DIAL precision. Parameters as in Figure 41 except nighttime observations with albedo 0.1 and filter width 0.2 nm.

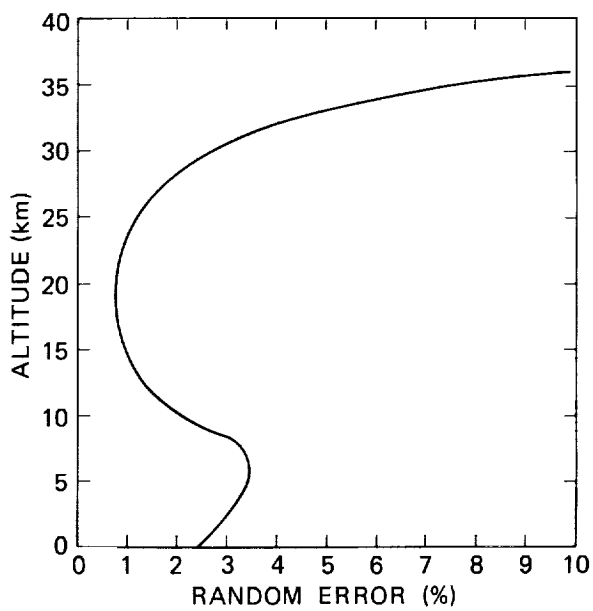

Figure 45. Ozone DIAL precision. Parameters as in Figure 41 except nighttime observations with albedo 0.1, filter width 0.2 nm, and Δz = 5 km.

but there will be space, weight, and power limitations on the Eos initial orbiting configuration (IOC). A scanning mode will require these changes:

- Provisions to compensate for the momentum changes induced by moving parts of the scanning device.
- Provisions to accommodate the additional instrument packages required for a LASA scanner.
- Provisions for increased power demand for a LASA scanner.
- Increased pulse rate commensurate with increased ground coverage.

A further consideration is this. A nadir-looking lidar with a FOV of 0.1 mr from 700 km orbit maps out a 70 m wide ribbon swath across the globe.

Because of limited available power for the lidar from the Eos platform and because of lifetime consideration for laser components, one is limited to a pulse repetition rate of about 10 Hz. Therefore, one cannot consider total global coverage from a lidar experiment unless a coarse average over a large area is taken. Essentially, the lidar provides for a series of detailed sets of atmospheric measurements across the globe with wide swath gaps between the ribbons of lidar data. The addition of a scanning arrangement would fill the large gaps between the swaths obtained by the nadir instrument; the larger area covered, however, would have to assume a large-area horizontal homogeneity for chemical species for the expanded area to provide an accurate representation of global profiles. Essentially, one is averaging the same number of laser shots required for a single profile over a larger area of the globe. The use of scanning would require more laser energy, because the slant path encounters more atmospheric absorption and scattering, and would entail a greater R^2 loss than the use of nadir viewing.

SYNERGISTIC SCIENCE

One of the fundamental objectives of Eos is to integrate to the fullest extent instrument systems to contribute complementary and/or mutually reinforcing data sets to the various disciplines.

Because of the highly interdisciplinary nature of Eos, this challenging goal can best be met if it is incorporated in the initial planning efforts.

To this extent, the LASA Panel has identified several areas of synergistic measurements, whereby one particular laser package can satisfy other measurement needs within LASA or where data sets mutually obtained by LASA, and by passive sensors or active sensors operating at wavelengths beyond infrared, strengthen the individual measurement sets by their complementary nature.

A few examples demonstrating the synergistic potential of LASA measurements are listed below:

- The LASA water vapor DIAL system could be used to make measurements – in addition to its primary function of obtaining water vapor profiles – of cloud-top heights, PBL heights, stratospheric aerosols, and tropospheric aerosols. This is possible because the information content of the "off-line" pulsed laser used in the DIAL measurements of water near 0.73 μm is also near optimum for measurements of aerosols, cloud distributions, and aerosol properties in the troposphere and stratosphere. Frequency doubling of the off-line laser output into the 0.365 μm wavelength region provides the desired second wavelength for the two-wavelength tropospheric and stratospheric aerosol measurements. There are many advantages in conducting simultaneous measurements of water and aerosol/cloud distributions in atmospheric investigations with a lidar system. The small-scale (vertical resolution, $\Delta z < 100$ m, and horizontal resolution, $\Delta x < 10$ km) atmospheric structure can be determined using the off-line lidar returns at a 10 Hz repetition rate, while the on-line lidar returns are being acquired for the larger-scale water vapor measurements ($\Delta z < 1$ km and $\Delta x < 100$ km).
- The measurement of water vapor will assist radiation studies when combined with other optical depth measurements of aerosols and clouds. Investigation of the atmospheric energy budget requires both passive and active techniques to observe seasonal and interannual variations in cloud properties, aerosols, radiation, liquid water, and water vapor. It is the complementary aspect of the LASA DIAL measurements to the data provided by passive remote sensors that permits a more complete understanding of important atmospheric processes on a global scale. While passive water vapor measuring devices provide global coverage, they are limited in spatial resolution and information content from lower atmospheric regions, and they depend on inversion techniques for obtaining water vapor concentration.
- Measurement of PBL height using LASA, along with passive microwave measurements of atmospheric moisture using the Eos High-Resolution Multifrequency Microwave Radiometer (HMMR), would provide an improved measure of moisture distribution with height. These measurements together would also allow for an estimate of moisture in the PBL. It is generally assumed that most of the moisture in the atmosphere (80 to 90 percent) is trapped within the PBL. Passive measurements of total atmospheric moisture, along with the height of the PBL together with the above assumption, are sufficient to derive the approximate moisture concentration in the PBL. Moisture concentration near the Earth's surface has generally been used as one term in the bulk aerodynamic approach to estimating surface moisture fluxes. Clearly, surface moisture flux is an important term in the hydrological cycle.
- The measurement of aerosol optical characteristics and distributions can provide needed information for interpretation of measurements with passive satellite systems. Aerosol measurements with lidar will assist in removing aerosol-related artifacts from passive measurements of surface reflectance and atmospheric radiance. In particular, these

measurements can assist in the interpretation of data from Eos passive instruments such as MODIS and HIRIS. The combination of aerosol profile information with water vapor profiles obtained from HMMR at low vertical resolution (>3 km) and from LASA at high vertical resolution (<1 km) greatly enhances the science content of each independently.

- Carefully planned ground-based correlative measurements would yield valuable ancillary information to combine with the lidar aerosol backscattering measurements. These data can be used to construct reliable models for converting the aerosol backscatter to other desired radiative parameters such as aerosol extinction and optical depth. This procedure has already been used with good success in the case of correlative measurements of the stratospheric aerosol for the SAM II and SAGE satellite measurements.
- Clouds often interfere with passive observations of the Earth's surface or the retrieval of atmospheric parameters. For example, thin cirrus clouds may often be present and obscure Earth imagery, leading to errors in the observation of surface characteristics. Also, clouds are not always entirely transparent to microwave radiation. Small but significant residual errors may therefore arise, due to clouds, in the retrieval of atmospheric and surface parameters from passive microwave observations. The addition of lidar measurements to detect and quantify cloud presence could be useful in improving passive observations. These measurements may also be used to calibrate cloud-top heights obtained indirectly from infrared temperature determinations.
- The measurement of temperature profiles with LASA will provide information that will substantially enhance the interpretation of data from passive instruments as well as complement the data from other active experiments. The lidar will provide direct measurements of the temperature across given atmospheric layers without the need to use inversion techniques to retrieve the temperature profile, as required by passive sounders. This will allow comparisons of the measurements using two independent techniques. The high accuracy and vertical resolution of the lidar measurement will also supplement the passive sounding experiments by providing the shape of the temperature profile, which can then be used as a first guess by the passive systems.
- The measurement of ozone with LASA can be used to help recalibrate passive ozone column-content instruments. The multiwavelength lidar concept will simultaneously provide for density and temperature profiles in the 10 to 50 km altitude range, along with the ozone concentrations.

As Eos moves from concept to implementation, the LASA Panel envisions that considerable additional efforts will be devoted to better define the mutual interdependence of instrument packages. These ongoing efforts will guarantee that all data obtained from Eos are consistent in space and time so that they can be integrated into a mutually supportive data set to the benefit of all.

III. LASA SCIENCE: ICE-SHEET DYNAMICS AND SURFACE ALTIMETRY

LIDAR ALTIMETRY APPLICATIONS

The lidar altimeter provides precise range measurements to the Earth's surface by acquiring data on laser pulse time-of-flight and reflected pulse energy. The primary scientific need is for topographic mapping of polar ice-sheet surfaces. Altimetry data on terrain and ocean surfaces will provide additional useful data sets for the 90 percent of each orbit that lies outside the ice-sheet regions. When cloud cover obscures the Earth's surface, the altimeter will provide an accurate measure of cloud-top altitude. Analysis of the amplitude distribution of the altimeter pulse will also provide information on the surface roughness within the laser footprint for studies of glacier and sea-ice roughness and bare terrain microtopography.

Measurements of ice-sheet topography to the precision provided by lidar altimetry are not possible with radar altimeter instruments. Radar altimeters have a pulse-limited footprint that is kilometers in extent and is biased over the ice-sheet surface by the presence of crosstrack slopes (Griffiths, 1981). In addition, the radar altimeter depends on multiple pulse averaging because of target-induced speckle modulation and the consequent low SNR for an individual pulse measurement. The optical wavelength of the laser altimeter permits even a relatively small transmitter to provide a submilliradian beam divergence and beam-limited footprint of less than 100 m. This, together with a short, high-power pulse and freedom from speckle modulation, results in high-accuracy range measurements for individual laser pulses. The lidar altimeter also has the capability of a relatively large range gate, which will provide measurement of discontinuities in range (e.g., ice-shelf boundaries) with the full horizontal resolution provided by the altimeter repetition rate.

Over terrain features the small footprint, beam-limited geometry, and short-pulse measurement provide additional useful data sets. Most benefit is obtained when the precise laser-altimeter data are used for reference and intercomparison with wide survey topographic-mapping data from photographic and radar instruments. For certain types of terrain where precise knowledge of topography, and absolute roughness, and dynamic phenomena is required, lidar altimetry would provide the only space-based measurements with the appropriate vertical and spatial resolution. Examples of these types of terrain include volcanic areas, desert sand sheets, crustal flexure regions, impact craters, and flood plains. In addition, a unique application for the laser altimeter is found in the assessment of tropical biomass by the measurement of forest canopies and timber volume (Nelson *et al.*, 1984). Here, the short, beam-limited laser pulse can penetrate to the bare Earth, a measurement not possible with photographic techniques.

MEASUREMENT OBJECTIVES

A discussion of the science role of a lidar altimeter in ice-sheet measurements published by Zwally *et al.* (1981) documents the special needs of a laser altimeter for ice-sheet measurement. The principal requirements are for a small (70 m) footprint on the ice-sheet surface, a high SNR for accurate individual pulse (no averaging) measurements, a moderately high pulse repetition rate of at least 20 Hz over the ice sheets, and highly accurate pointing knowledge for each laser-pulse data point. The combination of the 70 m footprint requirement and the 700 km altitude of the Eos platform results in a requirement for a 0.10 mrad divergence angle.

The pointing requirement results from the mapping of angular offsets with respect to nadir into range measurement biases. Extremely accurate knowledge of altimeter attitude (to the arcsecond level for each laser pulse) is needed in order to compute altimetry angular offset from nadir. The scale factor relating altimetry range error to laser pointing uncertainty for a flat target surface is 3 cm/arcsec for a 700 km orbit altitude. Sloping target surfaces aggravate the effect of pointing error on altimetry accuracy. In addition to laser altimeter attitude, it is very important to know spacecraft position relative to Earth coordinates. The horizontal position of each laser-pulse footprint on the Earth's surface must be known to an accuracy of the order of 10 m. This can be accomplished by incorporating a global positioning system (GPS) receiver in the LASA instrument electronics package. Additional refinement of vertical position knowledge to the 10 cm level required for altimetry data can result from use of ground-based laser-ranging measurement to a retroreflector array located on the spacecraft. Laser-range measurement during flight by one or more of the existing stations of the Laser Tracking Network can define the spacecraft orbit to the centimeter level. The Geodynamics Laser-Ranging System (GLRS), described in the next chapter, ranging to a number of ground-based retroreflectors, can also provide a powerful solution to orbital parameters. Analysis of altimetry data to locate orbital crossing points provides the final step in reduction of spacecraft position errors.

Over the oceans, the laser altimeter will also provide a high-resolution verification of range

measurement for other more general survey instruments. In particular, the reduced dependence of optical range on the unknown column content of atmospheric water vapor suggests calibration of the radar altimeter with laser data. The short pulse and the small footprint of the laser altimeter can also be very useful in resolving ocean wave structure. Vertical resolution of 10 cm or better coupled with a 70 m footprint size results in data unavailable with radar altimeters.

SYNERGISTIC SCIENCE

One of the best synergisms for laser altimeter data is derived from simultaneous operation of laser and radar altimeters. In the case of the radar altimeter, it is assumed that the device available for flight on the Eos platform would be a derivative of the pulse compression 13.6 GHz radar altimeter first flown on Seasat. The relatively large footprint (several kilometers) of this device has the advantage of always including the satellite nadir point in its FOV. In ice-sheet altimetry, the laser data would define surface topography to high precision every 350 m along the nadir track, remove the surface-slope ambiguity characteristic of radar altimetry, and provide the only altimetry data in regions where the surface slopes are too large or changing too rapidly for the radar altimeter.

Over ocean areas, the radar altimeter has a clear advantage in providing accurate, all-weather, wide-coverage measurements of sea-surface topography. Bursts of high repetition-rate laser data (approximately 100 m spatial resolution) over ocean areas could, however, serve to calibrate the radar altimeter data by removing uncertainties in the microwave propagation delay due to atmospheric water vapor. At present, the lack of precise knowledge of the water vapor content contributes up to several tens of centimeters in range error, but only at microwave frequencies where there is significant water vapor effect on refractive index.

ALTIMETER INSTRUMENT DESCRIPTION

The lidar altimetry technique consists, in essence, in the precise measurement of the time of flight of the laser pulse from the transmitter to the surface and then back to the satellite detector. The timing precision should give an equivalent range resolution of 1 cm. Altimetry output data include pulse time-of-flight and transmitted and received pulse energy for each laser shot. The ratio of received and transmitted energies provides information on atmospheric transmission and target albedo variations.

The instrument design parameters (large aperture size and large laser pulse energy) assumed for the simulations described in the previous chapter were considered necessary for atmospheric lidar investigations. This results in an excess capability for altimetry that can be used to ensure that each individual laser pulse results in a high SNR range measurement. No averaging of sequential pulses is necessary or, in fact, desired. This is especially important for the ice-sheet topography data where a relatively small portion of each orbit offers an opportunity for data acquisition. Repetition rates of at least 20 Hz for laser operation are required to resolve kilometer scale horizontal structure on ice-sheet surfaces.

A block diagram showing the interrelationship of components in the altimeter mode of operation of the LASA instrument package appears in Figure 46. Two lasers are used in this concept for redundancy.

It may be advantageous to consider a simple form of crosstrack scanning for laser altimeter measurements. In general, the relatively low repetition rates of laser devices, even the 20 Hz of a burst-mode operation, are not sufficient to support scanning data acquisition. This is because the rapid movement of the satellite nadir point at approximately 7 km/sec requires obtaining all data along the nadir track in order to obtain sufficient horizontal resolution. If a sacrifice of along-track resolution is possible, the crosstrack data could provide additional information to resolve the surface-slope ambiguity of the radar altimeter over ice sheets. A major problem with crosstrack scanning beyond 1.5° is the degradation in precise range measurement due to pulse spreading. Any proposed use of scanning must also be approached cautiously because of the increased demands placed on the measurement of altimeter pointing attitude as the instrument optical system is in constant motion. Further studies are required to determine if the scientific benefits from scanning outweigh the degradation in horizontal resolution and range precision.

MEASUREMENT SIMULATIONS

The set of altimeter instrument parameters assumed here for simulation studies is included as Table 19. These parameters are significantly different, and in some respects more demanding on LASA design, from those given in Chapter II. Also note that the LASA maximum laser pulse energy of 1 J is not necessary for altimeter operation, and a transmitted energy value of 100 mJ has been assumed. This would conserve laser lifetime, conserve electrical power, and make possible the maximizing of laser repetition rate in a burst mode that may be required over the ice-sheet surfaces.

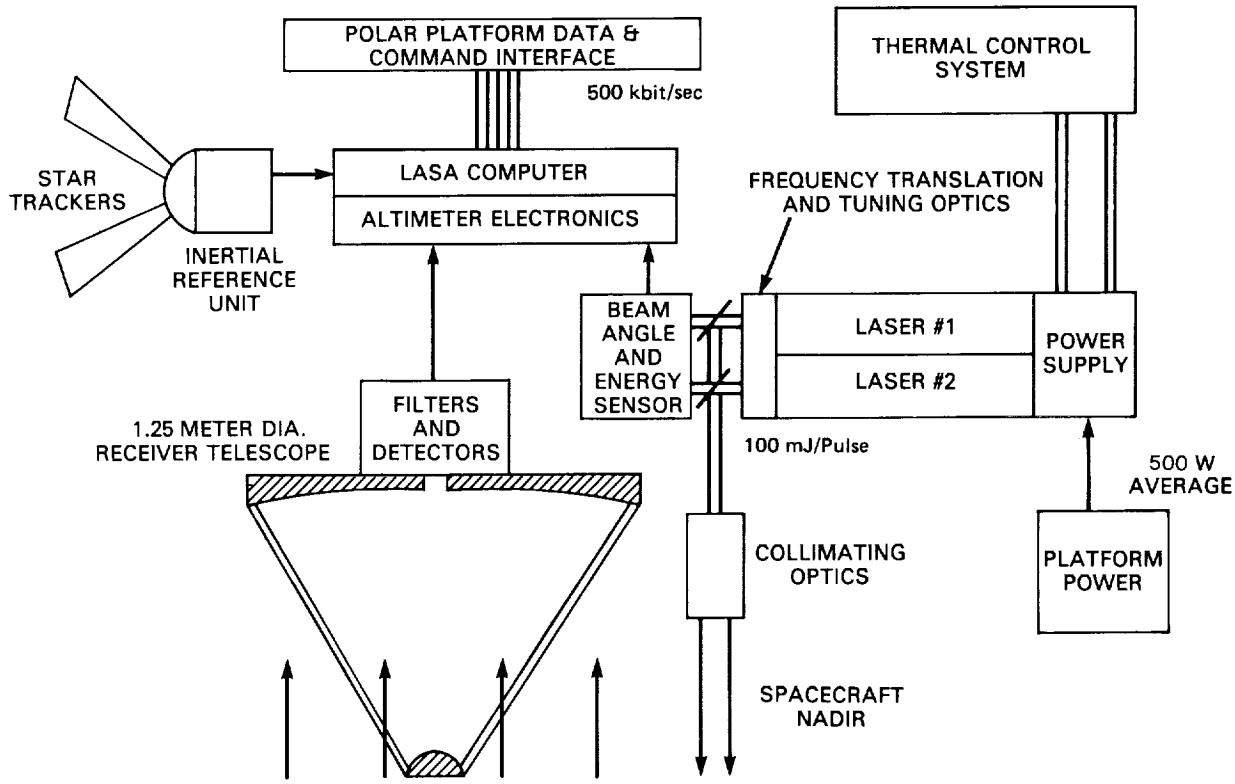

Figure 46. LASA atmospheric sounder and altimeter concept.

Table 19. LASA Altimeter Parameters

Parameter	Value
Laser Energy	100 mJ/pulse
Repetition Rate	20 Hz burst mode, 1 Hz to 5 Hz continuous
Laser Pulsewidth	5 ns
Laser Divergence	0.1 mrad
Receiver Optical Efficiency	0.38
Receiver Telescope Diameter	1.25 m
Optical Bandpass Filter	5 Å
Detector Quantum Efficiency	0.25 at 0.50 μm, 0.25 at 0.75 μm, 0.60 at 1.00 μm
Detector Bandwidth	50 MHz

Altimetry operation at three laser wavelengths of 0.5 μm, 0.75 μm, and 1.0 μm is indicated in this table. They represent the practical range of values that would provide good ice and snow reflectance, and are long enough in wavelength that atmospheric transmission is adequate. A plot of snow and ice reflectance from O'Brien (1975) is included as Figure 47. Note that reflectance begins to fall off near 1 μm wavelength and goes rapidly to near zero at 1.5 μm. These three laser wavelengths are also practical choices based on current and foreseeable laser technology. The wavelengths of 1.0 μm and 0.5 μm are close, respectively, to the fundamental and frequency-doubled wavelengths of the solid-state Nd:YAG laser and its derivatives. The 0.75 μm wavelength represents the spectral region where water vapor DIAL measurements are possible and the tunable, vibronic crystal lasers of Alexandrite, emerald, titanium-doped sapphire, and others are practical choices. Detector quantum efficiency is a

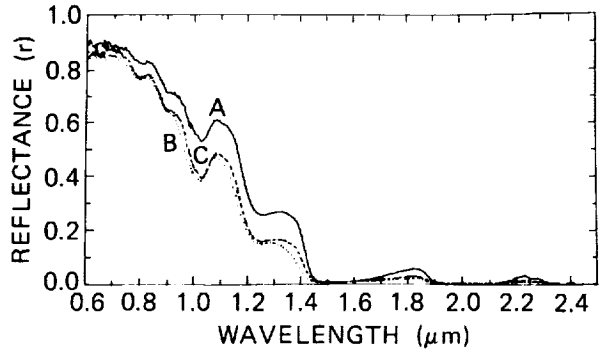

Figure 47. Reflectance (r) of old snow (relative to $BaSO_4$) versus wavelength. Curve A – original old cold snow, density = 0.347 g/cm³; Curve B – wet melting snow, density = 0.403 g/cm³; Curve C – refrozen snow, density = 0.403 g/cm³.

variable among these wavelengths. In the 0.5 μm to 0.75 μm region a photomultiplier tube is currently the best choice and provides nearly noiseless gain with a quantum efficiency of about 0.25 at 0.5 μm up to 0.4 at 0.75 μm. Near 1.0 μm the Si avalanche photodiode (APD) is the detector of choice. Its quantum efficiency is high, approximately 0.6, but the detection process suffers from excess noise in the APD and in its matching to a low-noise preamplifier. Detector performance at this wavelength is best specified by NEP, assumed here to be about 3×10^{-14} W/Hz$^{1/2}$.

A final consideration specific to the needs of the laser altimeter is choice of laser pulsewidth. The assumption in Table 17 of a 5 nsec full-width half-maximum (FWHM) laser pulsewidth is based on the use of a Q-switched solid-state laser and is necessary in order to provide the required range resolution in the altimetry processing electronics. A 5 nsec pulse represents a range resolution increment of 0.75 m. Actual range precision can be much better than this because of timing measurements made to a small fraction of the pulsewidth. The use of such a short pulse stands in contrast to the needs of atmospheric remote sensing, where much less vertical resolution is required.

Laser-altimeter data quality is determined primarily by the strength of backscattered laser radiation from the target surface, but is also affected by pulse-to-pulse variability, dynamic range considerations, and pulse spreading. The basic time-of-flight or range measurement deemed necessary for altimetry is, in essence, a threshold measurement. Only those pulses which trigger the discriminators enter into the data stream. This effect acts to suppress background noise and detector noise up to the point where they and their pulse-to-pulse variability have a significant probability of triggering the time-of-flight measurement. The laser-altimeter concept described above is based on a very high SNR environment so that each individual pulse can be depended upon for a unique range measurement. Thus, the altimetry performance analysis is primarily one of verifying that an adequate SNR is present at most times, and describing those circumstances that can lead to marginal detector SNR.

Target reflectance specification is a first step toward calculation of received signal strength. For discrete targets, as found in reflection of laser pulses from the ice-sheet surface, ocean surface, or terrain features, the specification of target backscatter is conveniently described by the term r/Ω where r is target reflectance (hemispherical) and Ω is the solid angle of backscatter. For a Lambertian (diffuse) target backscatter at normal incidence, $\Omega = \pi$. The ice-sheet surface is well modeled by such a Lambertian reflectance and has values of r/Ω in the range of $0.4/\pi$ to $0.8/\pi$, dependent on laser wavelength and snow/ice composition and age. Soil and vegetation are somewhat more variable and lower in reflectance with r/Ω estimated in the range of $0.1/\pi$ to $0.4/\pi$. The ocean surface is a special case since it exhibits a specular rather than a Lambertian reflectance. This is especially true near normal incidence (nadir-viewing) where a mirror-like reflectivity is one component of the backscatter. Fresnel reflectance of ocean water from 0.5 μm to 1.0 μm is only about 0.02 but the solid angle of backscatter can be significantly smaller than a Lambertian surface. Ocean backscatter is typically concentrated into a specular reflection of 10° to 30° width. Actual width of the backscatter pattern is determined by the orientation of the smallest wave slopes within the laser footprint. These slopes act as mirror surfaces and are distributed in tilt angle in accordance with wave and wind statistics. Recent airborne laser measurements and a full explanation of these phenomena are presented by Bufton *et al.* (1983). The range of variability of ocean surface backscatter is taken from these measurements to be $0.1/\pi$ to $0.3/\pi$ within a few degrees of nadir.

Cloud tops are diffuse targets that require characterization in terms of a backscatter function $\beta\Delta Z$, where β is backscatter coefficient in $m^{-1}\ sr^{-1}$ and ΔZ is scattering pathlength in the cloud. Typical values of $\beta\Delta Z$ for thick cloud layers can be derived from the β and extinction (E) values reported by Cato *et al.* (1967). They are in the range 0.01 to 0.1 for the LASA range of wavelengths.

It should be obvious that the presence of cloud cover will disrupt laser altimetry data and at the same time enable the measurement of cloud-top height. Some thin cloud layers will permit continued altimetry operations at reduced SNR margins. This is the case for thin cirrus layers. Cirrus cloud models show that mid-latitude and polar regions have 40 percent to 50 percent cirrus cloud cover at all times, while the equatorial region has an 80 percent incidence of cirrus. Typical cirrus cloud thickness is about 1 km and 75 percent of all cirrus is less than

2 km thick. Cirrus layers are almost invariably the highest layers (5 to 15 km) and are, thus, a factor in attenuation of laser radiation for both the altimetry and cloud-top data sets. An analytical and empirical model for cirrus transmission is reported by Kneizys *et al.* (1983). The total path loss for the two-way propagation path through cirrus, as calculated from this model, is $T_A^2 = \exp(-0.28\ L^2)$, where L is cirrus layer thickness in kilometers. Polar stratospheric clouds have also been shown by Hamill and McMaster (1984) to be a significant factor in the polar night where sufficiently low stratospheric temperatures lead to a high incidence of a broad, optically thin cloud layer.

A more serious degradation of two-way optical transmission in the 0.5 μm to 1.0 μm altimetry wavelength region is imposed by molecular scattering, and both scattering and absorption by lower-tropospheric aerosols. The transmission models developed for these effects by the Air Force Geophysics Laboratory (AFGL) represent a convenient way of parameterizing the effects of atmospheric loss on altimeter performance. There is little variability in molecular scattering loss versus season or latitude in the altimetry wavelength region, and total two-way extinction is small, especially at the long wavelength end (1.0 μm) due to the inverse fourth-power Rayleigh scattering. Aerosol extinction is significant in the atmospheric surface layer. In the analysis presented here, the AFGL Rural, Tropospheric, Maritime, and Urban aerosol models were used. These models are fully documented by McClatchey *et al.* (1970) and Shettle and Fenn (1979). Table 20 lists values of two-way atmospheric transmission for each of these models under clear (C) and hazy (H) conditions and the three altimetry wavelengths under consideration. The small effect of molecular scattering is included in each transmission value.

For nadir-viewing altimetry operation, the lidar or link equation for received laser pulse energy E_R can be written

$$E_R = E_T \frac{A_R}{Z^2} T_O T_C T_A^2 \ (r/\Omega) \qquad (1)$$

where E_T = transmitted laser energy, A_R = receiver area, T_O = receiver optical transmission, T_C = cirrus cloud transmission, T_A^2 = atmospheric molecular and aerosol transmission, $[\exp(-2X_T)]$, X_T = total atmospheric extinction, and r/Ω = target backscatter.

Calculations of E_R were performed for high (H), typical (TYP), and low (L) values of r/Ω from Table 21 for each of the four target surfaces: ice and snow, ocean surface, soil and vegetation, and cloud top. The ratio of E_R to the quantity $h\nu/q$ (energy per photoelectron) yields the magnitude of the laser backscatter signal in photoelectrons. In this expression, $h\nu$ is energy of one photon at frequency ν and q is detector quantum efficiency. At 0.5 μm and 0.75 μm, the altimetry detector is assumed to be a photomultiplier tube. At 0.5 μm a quantum efficiency of 0.25 is assumed, while at 0.75 μm a quantum efficiency of 0.4 is possible. These values lead respectively to energies of 1.6×10^{-18} J/photoelectron and 6.6×10^{-19} J/photoelectron. At 1.0 μm, the Si APD detector has quantum efficiency of at least 0.6, which results in 3.3×10^{-19} J/photoelectron. Tables 22, 23, and 24 present the expected number of photoelectrons per laser pulse and the signal-to-background ratio E_R/E_B. Each table is produced for one of the three proposed altimeter wavelengths and includes the results of calculations for clear and hazy

Table 20. Two-Way Nadir-Viewing Atmospheric Transmission

Aerosol Model	Visibility	Laser Altimeter Wavelength					
		0.5 μm		0.75 μm		1.0 μm	
		X_T	T_A^2	X_T	T_A^2	X_T	T_A^2
Tropospheric	C	0.21	0.66	0.090	0.84	0.039	0.93
	H	0.39	0.46	0.22	0.64	0.12	0.79
Maritime	C	0.28	0.57	0.16	0.73	0.13	0.77
	H	0.88	0.17	0.73	0.23	0.81	0.20
Rural	C	0.38	0.47	0.21	0.66	0.13	0.77
	H	0.95	0.15	0.65	0.27	0.43	0.42
Urban	C	0.44	0.41	0.26	0.60	0.18	0.70
	H	1.44	0.056	1.07	0.12	0.75	0.22

X_T = Total atmospheric extinction
T_A^2 = Two-way atmospheric transmission, $\exp(-2X_T)$

Table 21. Target Backscatter Properties

Target Type	Target Reflectance	Laser Altimeter Wavelength					
		0.5 μm		0.75 μm		1.0 μm	
		R_T	r/Ω	R_T	r/Ω	R_T	r/Ω
Ice and Snow	H		$0.8/\pi$		$0.7/\pi$		$0.6/\pi$
	TYP	25	$0.7/\pi$	23	$0.6/\pi$	16	$0.5/\pi$
	L		$0.6/\pi$		$0.5/\pi$		$0.3/\pi$
Ocean	H		$0.3/\pi$		$0.3/\pi$		$0.3/\pi$
	TYP	2	$0.1/\pi$	3	$0.1/\pi$	4	$0.1/\pi$
	L		$0.02/\pi$		$0.02/\pi$		$0.02/\pi$
Soil and Vegetation	H	8	$0.5/\pi$	8		5.2	
	TYP	6.5	$0.23/\pi$	7	$0.24/\pi$	6.5	$0.25/\pi$
	L	5.5	$0.1/\pi$	6.1		7.3	
Cloud Top	H	25	0.10	23		14.5	
	TYP		0.01		0.01		0.006
	L	19	0.001	19		11	

R_T = Daytime radiance (mW/m²-sr-Å) at solar zenith angle = 60°
r/Ω = Target backscatter factor

conditions for each of the aerosol models deemed applicable to altimetry data for each target. Note that better altimetry performance is indicated as the wavelength increases. This is a result of the increase in number of photons for a given E_R as wavelength increases and small improvements in atmospheric transmission (despite a reduction in target backscatter cross section) at 1.0 μm. In nearly all cases, the number of signal photoelectrons (SPE) is quite large. The only significant reduction in received photoelectrons below 500 occurs under hazy conditions with maritime or urban aerosols at 0.5 μm wavelength.

Calculations have also been made for received optical energy (E_B) resulting from daytime background radiance of the various target surfaces. For these calculations of energy, a time interval of 15 nsec was assumed. This is appropriate for detection of the full backscattered (undistorted) laser pulse and is three times the laser pulsewidth. The values of E_B are calculated from,

$$E_B = R_T R_O F_B A_R 15 \times 10^{-9} \text{ sec}, \qquad (2)$$

where R_T = target radiance (W/m²-sr-Å), R_O = receiver FOV (sr), F_B = filter bandpass (Å), and A_R = receiver area (m²).

Values of R_T from Wolfe and Zissis (1978) are listed in Table 21 as a function of wavelength and target type. The other parameters are given in Table 19. In Tables 22, 23, and 24, the ratio of E_R/E_B is included to show the margin of laser backscatter signal strength over the background of a solar-illuminated target. Note that most ratios are on the order of 100 to 300 and quite consistent at the three wavelengths. The only exceptions are ratios of 10 to 15 for altimetry detection of daytime cloud tops. Even in these more marginal cases, the SNR is adequate to permit an altimetry threshold setting that will eliminate the mean background photoelectron level from triggering the time-of-flight and energy measurement electronics. Background-induced quantum noise $(E_B)^{1/2}$ will also be dominated by laser signal quantum noise. The amount of background radiance from moonlit clouds for nighttime operations is about 10^{-6} less than the daytime values.

For the quantum-noise-limited photomultiplier tubes, the noise level is simply the square root of the number of signal photoelectrons, $(E_R)^{1/2}$. In the case of the Si APD, the NEP estimated from state-of-the-art devices is 3×10^{-14} W/(Hz)$^{1/2}$. This leads to a noise equivalent energy (NEE) of 3.2×10^{-18} J for the assumed 50 MHz detection bandwidth and 15 nsec interval, or about 10 photoelectrons. Hence, a value of 10 photoelectrons must be added to E_R before the square root is taken to calculate noise. With the strong laser backscatter of several hundred to several thousand photoelectrons, predicted in Tables 22, 23, and 24, this effect of detector noise is negligible.

Such strong laser backscatter for individual pulses means that altimetry signal processing can be done with pulse-current waveforms, and photon

Table 22. SPE and E_R/E_B for 0.5 μm Altimetry Wavelength

Target Type		Aerosol Model							
		Tropospheric		Maritime		Rural		Urban	
		C	H	C	H	C	H	C	H
Ice and Snow	SPE	6,900	4,600	5,600	2,100	4,600	1,500	4,000	550
	E_R/E_B	210	170	190	130	180	100	160	60
Ocean	SPE	940	620	810	240	690	210	—	—
	E_R/E_B	380	290	350	190	320	180	—	—
Soil and Vegetation	SPE	2,100	1,500	—	—	1,600	490	1,300	180
	E_R/E_B	260	220	—	—	230	130	210	77
Cloud Top	SPE	290	210	—	—	—	—	—	—
	E_R/E_B	12	10	—	—	—	—	—	—

Table 23. SPE and E_R/E_B for 0.75 μm Altimetry Wavelength

Target Type		Aerosol Model							
		Tropospheric		Maritime		Rural		Urban	
		C	H	C	H	C	H	C	H
Ice and Snow	SPE	18,000	13,000	15,000	4,800	14,000	5,600	13,000	2,600
	E_R/E_B	230	190	200	120	200	120	190	85
Ocean	SPE	2,900	2,300	2,600	800	2,300	940	—	—
	E_R/E_B	280	250	270	150	250	160	—	—
Soil and Vegetation	SPE	7,100	5,300	—	—	5,600	2,300	5,000	1,000
	E_R/E_B	290	250	—	—	260	170	250	110
Cloud Top	SPE	920	700	—	—	—	—	—	—
	E_R/E_B	14	12	—	—	—	—	—	—

counting may not be necessary. The major source of difficulty in acquisition of altimetry data is likely to be the dynamic range necessary to accommodate variability in E_R. Two sources of expected variability in E_R are target reflectance variations from pulse to pulse and atmospheric transmission fluctuations due to aerosols or thin clouds. Atmospheric turbulence and target-induced speckle noise will be negligible for telescope apertures of 0.5 m or larger. It is beyond the scope of this report to quantify E_R variability, but this study needs to be done.

As mean atmospheric attenuation increases, or for operation at the low end of backscatter variability, the smaller number of received signal photoelectrons results in increased range error. This effect is readily quantified by use of Poisson statistics for the rate of emission of both signal and background photoelectrons. It is shown by Abshire (1978) that the rms theoretical ranging precision ΔR for an optimum matched filter receiver for N_S signal photoelectrons and a laser pulsewidth ΔT is given by

$$\Delta R = (c\Delta T/2\pi)/(N_S)^{1/2} \qquad (3)$$

For 100 photoelectrons this expression yields a ΔR of 1.2 cm (0.08 nsec). This precision will be further degraded by the presence of background photoelectrons according to

$$\Delta R = (c\Delta T/2\pi)/\{N_B + N_S - [N_B (N_B + 2N_S)]^{1/2}\}^{1/2} \qquad (4)$$

This increases ΔR to 2.3 cm (0.15 nsec) when N_S and N_B are both at the 100 photoelectron level

Table 24. SPE and E_R/E_B for 1.0 μm Altimetry Wavelength

Target Type		Aerosol Model							
		Tropospheric		Maritime		Rural		Urban	
		C	H	C	H	C	H	C	H
Ice and Snow	SPE	33,000	28,000	28,000	7,200	28,000	15,000	25,000	7,800
	E_R/E_B	290	260	250	130	250	180	250	130
Ocean	SPE	6,600	5,600	5,600	1,400	5,600	3,000	—	—
	E_R/E_B	220	200	210	100	210	150	—	—
Soil and Vegetation	SPE	17,000	14,000	—	—	14,000	7,500	13,000	4,000
	E_R/E_B	340	330	—	—	310	240	310	170
Cloud Top	SPE	1,300	1,100	—	—	—	—	—	—
	E_R/E_B	15	14	—	—	—	—	—	—

(i.e., a unity SNR). Practical laser-ranging receivers are usually within a factor of ten of these theoretical results. Their additional errors result from timing jitter in both detector and processing electronics and possible biases due to laser transverse mode structure. By minimizing these practical difficulties, it should be possible to obtain rms range precision under 10 cm rms for a 5 nsec laser pulse.

A more dramatic increase in altimeter range uncertainty ΔR (than that due to low signal levels or strong background) results from pulse spreading since both Equations (3) and (4) are proportional to ΔT. The interaction of a finite laser beamwidth δ, an angular offset ϕ from nadir, and a surface slope S can produce significant spread ΔT_i beyond the nominal laser pulsewidth ΔT. This spread can easily be estimated from the expression derived from the geometry illustrated in Figure 48.

$$\Delta T_i = (2/c) \tan (\phi + S) Z\delta \qquad (5)$$

where c is the speed of light and Z is the slant range to the surface. Note that surface slope can either add a pulse spread or reduce it depending on slope polarity with respect to the angular offset from nadir. For the LASA laser altimeter, $Z = 7 \times 10^5$ m, $\delta = 1 \times 10^{-4}$ rad, $\phi < 10^{-2}$ rad, and, for ice-sheet altimetry, $S \leq 10^{-2}$ rad, 82 percent of the time. As a result, $\Delta T_i \leq 9.3$ nsec and the original laser pulse of 5 nsec is spread by a factor of two. This will require, according to Equation (3), a factor of four increase in the number of signal photoelectrons to achieve the same range precision.

When the angular offset ϕ is not known exactly (i.e., there is satellite attitude error) the uncertainty $\Delta\phi$ maps directly into a range error $\Delta R_i = \Delta T_i c/2$. This effect can be calculated from Equation (5) with $\Delta\phi$ substituted for δ. The work of Zwally *et al.* (1981) documented these angular uncertainty effects on range error as a function of S for various $\Delta\phi$ values. Their results are repeated in Figure 49 and show that LASA attitude knowledge must be kept to about 5 arcsec rms for 10 cm precision or better altimetry measurements of the ice-sheet surfaces.

The range measured to the Earth's surface from a space-based laser altimeter exceeds the actual range due to a slowing (propagation delay) of the optical pulse by the refractive index of the atmosphere. The amount of this delay depends on meteorological conditions and is about 2.4 m at nadir for the two-way atmospheric path from space to sea level and return. The delay is also an inverse

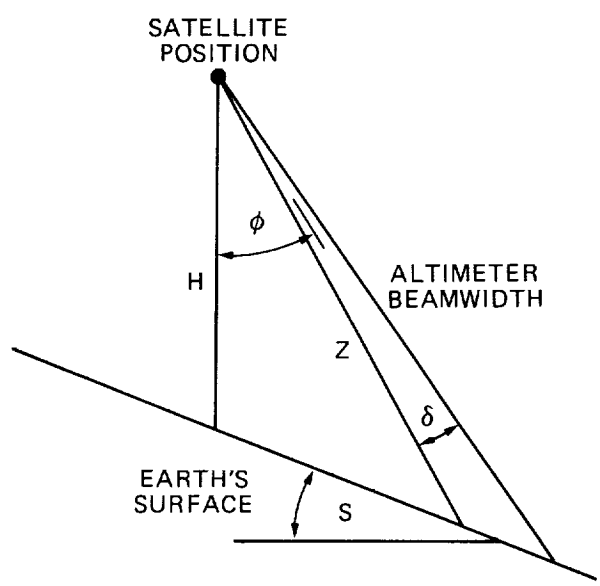

Figure 48. Geometry for laser altimeter ranging error in off-nadir pointing.

function of wavelength. Hopfield (1972) points out that the propagation delay is simply the integral over $(n-1)$ along the propagation path where n is the local atmospheric refractive index (proportional to atmospheric density). For vertical observations, the integral over atmospheric density is just the surface pressure. Thus, at nadir the propagation delay is independent of surface temperature and temperature structure in the atmosphere. Marini and Murray (1973) report a formula for range correction to account for the propagation delay. It is given approximately by

$$\Delta R = 0.002357(0.9650 + 0.0164/L^2)P_s \quad (6)$$

where L is laser wavelength in micrometers, P_s is surface pressure in millibars, and ΔR is range correction in meters. At 0.5 μm wavelength, ΔR is 2.46 m and decreases to 2.34 m at 1.0 μm. The derivative of Equation (6) with respect to surface pressure yields a range correction sensitivity of 2.3 mm/mb. Thus, a 43 mb uncertainty in P_s would result in a 10 cm range error. This illustrates that P_s must be known or modeled to about 2.5 percent in order to keep the uncertainty in atmospheric propagation delay less than the required range precision.

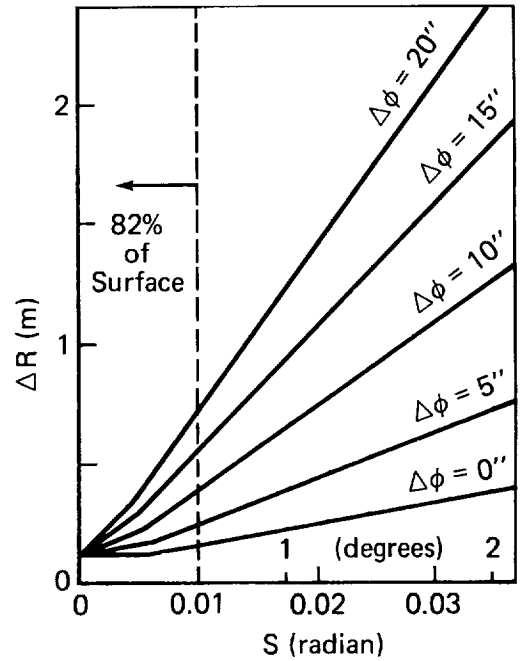

Figure 49. Laser ranging error (ΔR) versus surface slope (S) for various values of satellite pointing error (Δφ).

EXAMPLES OF LASER-ALTIMETER DATA

Laser-altimeter data useful for determination of ice-sheet topography will necessarily require a stable space platform, careful correction for laser-pointing angle and orbital position, and an accumulation of multiple data sets over months of time with many opportunities for orbital-track crossing points. Approximately 1 year of space-based observations will be required in order to provide an adequate data product for the polar ice sheets. It is not possible to perform quick, suborbital mapping of ice-sheet areas. Fortunately, the time constant of the ice sheet and other surface topographical processes is sufficiently slow that a gradual accumulation of high-precision data is possible. At present, only demonstration data sets of laser altimeter operation from aircraft are available. They serve to illustrate the type and quality of data that need to be accumulated.

Figure 50 is an example of a continuous profile of laser-altimeter data acquired over the sea ice in the 1970s from the NASA C130 aircraft. These data were acquired with a laser-geodimeter ranging device that is the cw analog of the pulsed laser altimeter planned for LASA. This data set illustrates centimeter-level range precision from an aircraft platform and demonstrates the need for correction of low-frequency biases or drift in altitude due to aircraft motion. The typical ice-sheet surface roughness with peak-to-peak variations of a few meters

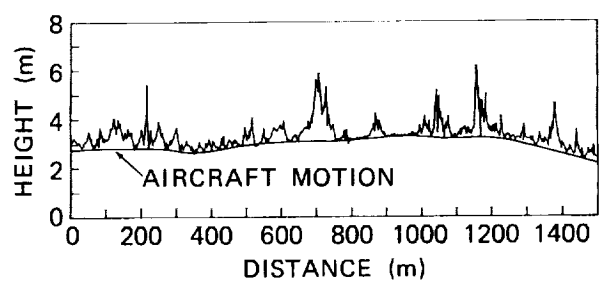

Figure 50. Continuous profile laser altimetry over sea ice in the 1970s.

and horizontal scales of tens-to-hundreds of meters is evident in the figure. The planned laser footprint size of 70 m for the LASA altimeter would integrate over some of the fine-scale structure seen here and would resolve the large-scale structure. Sea-ice roughness would be revealed by a slight spreading of each LASA altimeter laser pulse.

Figure 51 is an example of aircraft laser-altimetry data on a profile crossing the California coast just south of Big Sur. In this case, the laser-altimeter instrument was a pulsed Nd:YAG system constructed for cloud lidar observations and operated on the NASA ER-2 aircraft in 1983. The significance of this data set is the 10 cm resolution in range measurement with over 1,000 m change in surface topography as the aircraft flight-track crossed the coastal mountain range. Over the ice sheets, the same vertical resolution is required and

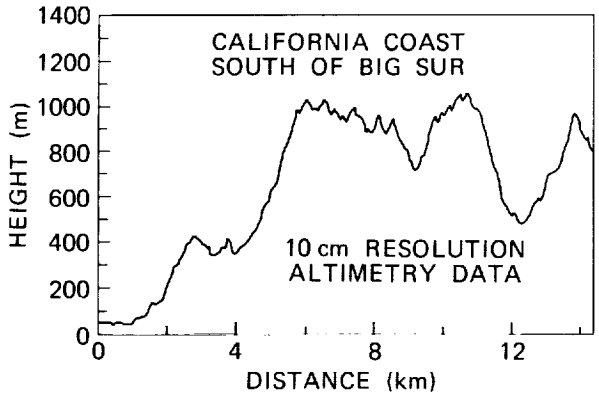

Figure 51. Altimetry mode data, Goddard Space Flight Center (GSFC) ER-2 cloud lidar system, October 10, 1983.

total vertical excursions can reach several kilometers. During this laser profile, the altimeter instrument maintained a high SNR measurement on each laser pulse as it constantly followed large excursions in the mean surface height. All data were acquired from an aircraft altitude of 25 km, beyond a significant portion of the Earth's atmosphere. The NASA ER-2 cloud lidar system that made these measurements is shown in Figure 52. It is a forerunner of the space-based LASA altimeter by virtue of its autonomous operation, compact size, and ability to withstand reduced atmospheric pressure (4 psi) and wide variations in the thermal and vibration environment. This cloud lidar is functionally identical to the instrument required for ice-sheet measurements, with the exception of no correction for platform pointing angles or position.

A further example of airborne data acquisition with a pulsed laser altimeter is shown in Figure 53. These data were acquired from a relatively low altitude, 300 m, by the NASA Airborne Oceanographic Lidar (AOL) system in the terrain-mapping mode (Nelson *et al.*, 1984). The significance of this data set lies in the high repetition rate (400 Hz) of pulse measurements while maintaining a 10 cm-level range precision. Note the returns from both the top of the deciduous tree canopy and the forest floor. This illustrates the use of laser altimetry for an assessment of tree height relevant to biomass determination and the ability of the small, high SNR laser pulses to penetrate to the Earth's surface for a "bare-Earth" range measurement.

The evolution of laser-ranging technology toward shorter laser pulses and higher resolution

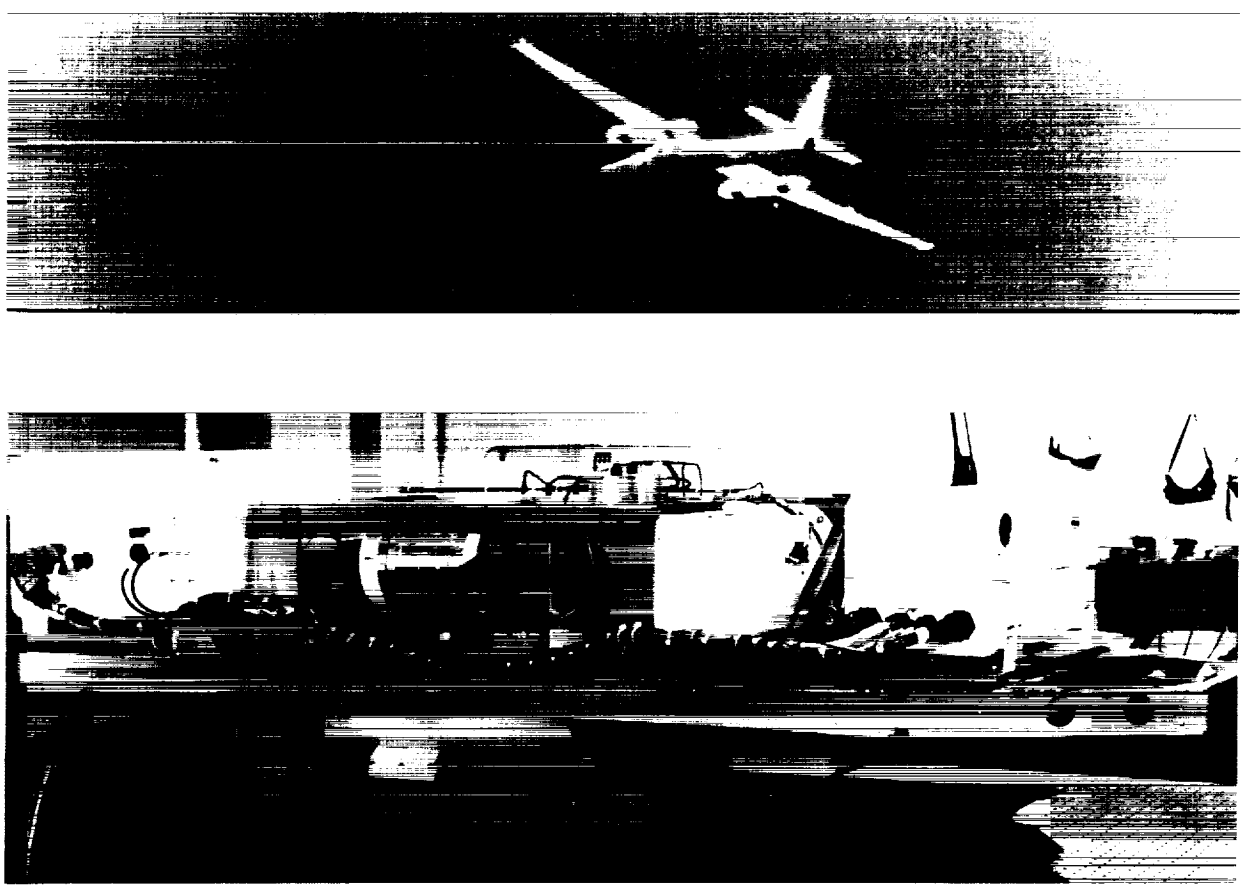

Figure 52. ER-2 lidar experiment.

ORIGINAL PAGE IS
OF POOR QUALITY

ORIGINAL PAGE IS
OF POOR QUALITY

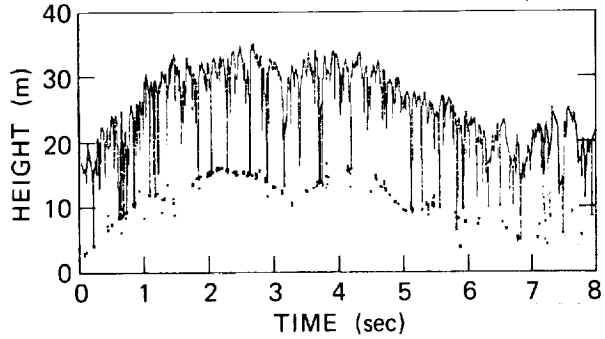

Figure 53. Airborne laser altimeter data (terrain backscatter).

receivers has resulted in the present achievement of 30 psec pulses and millimeter-level range precision. The addition of two-color capability (simultaneous range measurement at two laser wavelengths) permits measurement of atmospheric dispersion over the range path to high precision. This in turn yields an accurate measure of surface pressure for vertical propagation paths. Recent laser-altimetry measurements of the ocean surface from an airborne platform (Abshire *et al.*, 1985) have demonstrated this technology and precision in the field. A summary of their technology, method, and data is presented in Figure 54. The key features of the instrumentation are a cavity-dumped Nd:YAG laser and a streak-camera receiver. These data serve as an extreme example of high-resolution laser altimetry from a remote platform.

A final example of laser-altimeter data presented in Figures 55 and 56 is the space-based data provided by the Apollo Lunar Laser Altimeter program. The data coverage illustrated in Figure 55 shows the beginnings of a topographic map of the lunar surface obtained in the Apollo 15, 16, and 17 missions. Data in Figure 56 show the laser altimeter and a radar altimeter working together to map a portion of the lunar surface in the Apollo 15 mission. Range precision in all the laser data was 1 m. These data have been of extreme importance in lunar geological and geophysical studies (Kaula *et al.*, 1974), particularly in high-resolution studies of

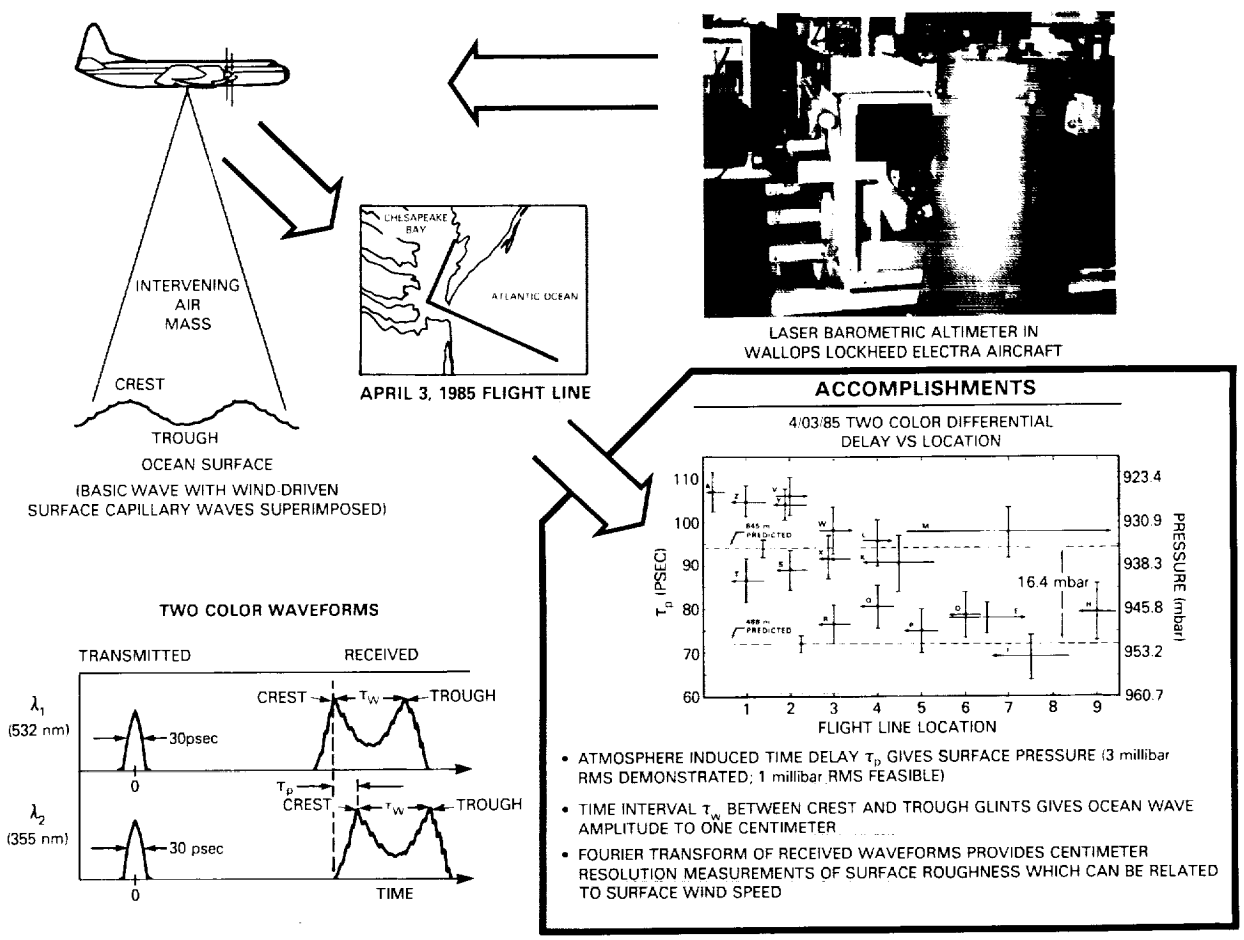

Figure 54. Office of Aeronautics and Space Technology/Goddard Space Flight Center (OAST/GSFC) demonstration of two-color picosecond pulse laser altimetry measurements of atmospheric surface pressure and sea state.

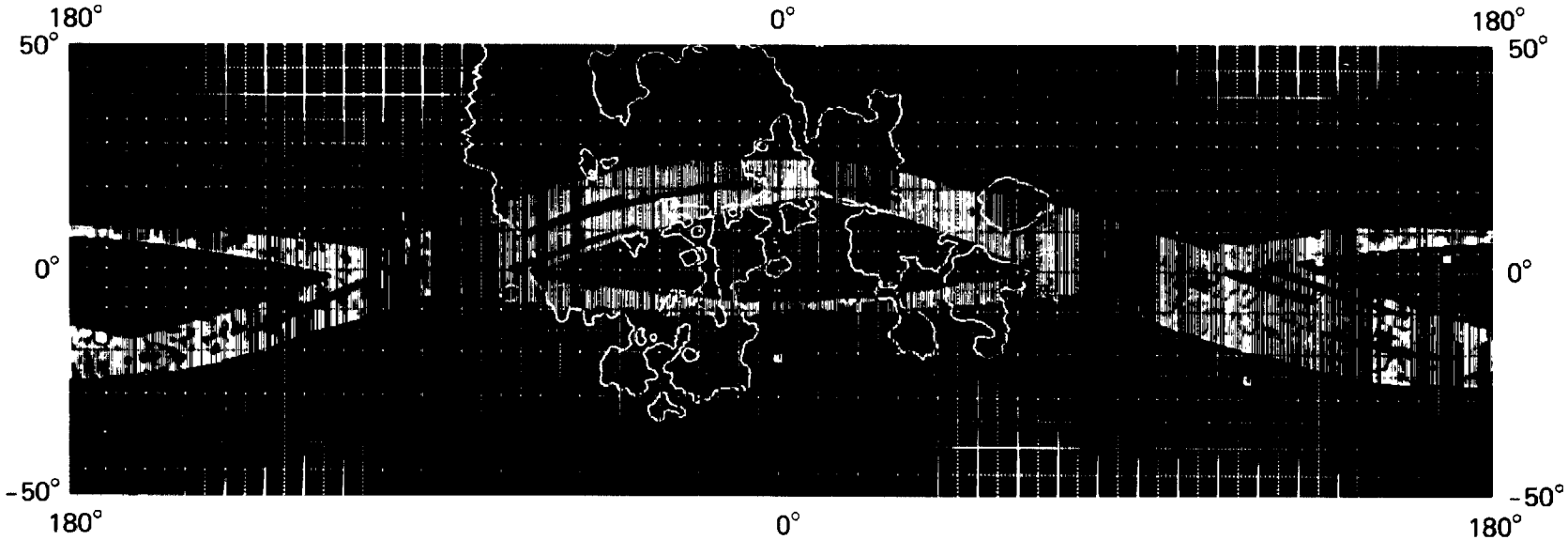

Figure 55. Topographic map of lunar surface obtained in Apollo 15, 16, and 17 missions.

ORIGINAL PAGE IS
OF POOR QUALITY

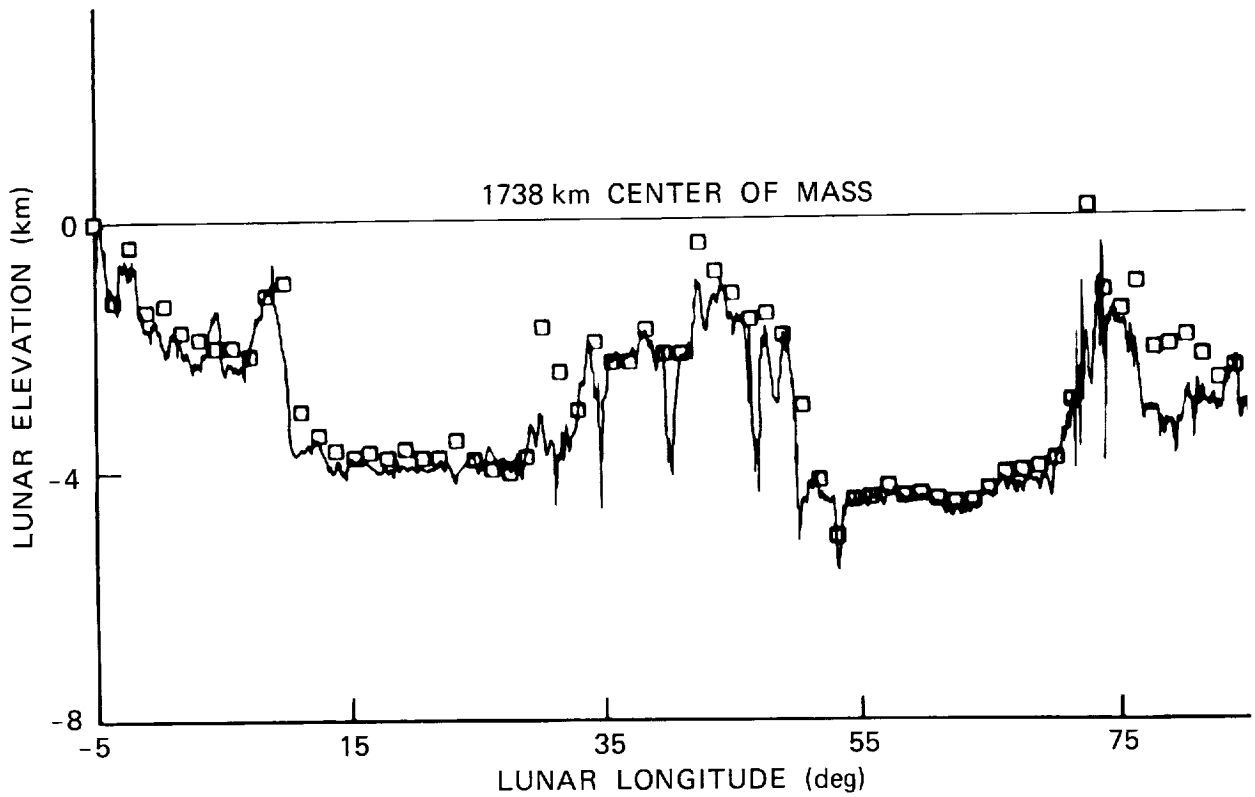

Figure 56. Maria Crisium and Serenitatis; the squares represent the laser altimeter measurements.

lunar-basin topography. These results, both simulations and actual observations, illustrate the capability of a space-based altimeter instrument, demonstrate the technical maturity of laser altimetry, and foreshadow the unique scientific results possible with the LASA altimeter.

IV. LASA SCIENCE: GEODYNAMICS AND LASER-RANGING APPLICATIONS

INTRODUCTION

Historically, two principal space technologies have emerged as the primary sources of data that support crustal dynamic studies – ground-based satellite laser ranging (SLR) and very long baseline interferometry (VLBI). In the SLR technique, ultrashort laser pulses are reflected off orbiting satellites and measurements of their time of flight are analyzed to yield centimeter-precision range information. Utilizing SLR data from a global network of ground-based stations and accurate models of the Earth's geopotential field to propagate the orbit of a high-altitude satellite such as the Laser Geodynamics Satellite (LAGEOS), the relative positions of the stations have been determined with centimeter accuracies. In the passive VLBI approach, the incoherent emission of radio stars is observed simultaneously at two widely separated ground locations. Cross-correlation analysis of the signals observed at the two sites yields a differential time delay proportional to the component of the baseline between the two stations in the direction of the astronomical source.

Comparative measurements of baselines between sites separated by thousands of kilometers, utilizing both techniques, have shown agreement to within a few centimeters (Kolenkiewicz *et al.*, 1985). Table 25 gives the results of these measurements and comparisons for some sample baselines. For the 22 baselines considered, the rms difference about 0 was 5.2 cm and the mean difference was 1.0 ± 1.1 cm. Repeated measurements of baselines across fault lines over several year time intervals have yielded highly accurate values for the relative velocities of the tectonic plates, that are on the order of a few

Table 25. SLR and VLBI Baselines and Their Differences: Ordered by Length (cm)

From	To	Length	SLR	VLBI	SLR – VLBI
Westford	Pasadena*	405,702,200+	3	7	−4
	Owens Valley	392,972,500+	83	77	6
	Goldstone	390,059,500+	76	76	0
	Fort Davis	313,863,600+	10	16	−6
	Platteville	275,321,900+	14	18	−4
Fort Davis	Quincy	184,183,700+	85	79	6
	Owens Valley	150,127,300+	80	76	4
	Pasadena*	138,369,700+	73	63	10
	Goldstone	129,433,300+	100	98	2
Platteville	Owens Valley	122,172,600+	61	67	−6
Fort Davis	Monument Peak*	119,828,300+	84	76	8
	Platteville	105,568,500+	89	85	4
Quincy	Monument Peak*	88,360,100+	80	79	1
	Pasadena*	68,574,300+	28	32	−4
	Goldstone	63,970,200+	98	94	4
Owens Valley	Monument Peak*	51,088,100+	1	8	−7
	Quincy	38,206,700+	79	71	8
	Pasadena*	33,604,200+	82	79	3
Goldstone	Monument Peak*	26,365,300+	71	76	−5
	Owens Valley	25,828,900+	76	78	−2
Pasadena	Monument Peak	21,828,200+	80	80	0
	Goldstone*	17,137,400+	82	79	3

*Baselines crossing tectonic plate boundary

centimeters per year. Table 26 lists some baseline rates that have been measured using ground-based SLR techniques.

Because of the high cost of fabricating and operating the SLR and VLBI ground stations and the scientific imperative to monitor as many baselines as possible, new fixed stations are rarely built; rather, various sites are occasionally occupied by a limited number of mobile systems. Nevertheless, because of the high fabrication and operational costs of these options, data taking is still necessarily limited to a small number of sites. The density of sites is not adequate to provide the spatial and temporal resolution desired, for example, by scientists studying regional crustal deformation and strain.

The retroreflectors can also be attached to ice sheets to monitor their horizontal and vertical movements. The system would also be capable of providing additional data for gravitational field studies. These, in turn, yield information on the Earth's internal mass distribution, moments of inertia, and solid earth and ocean tidal components (NASA, 1983). An example of solid earth scientific results derivable from laser-ranging data is shown in Figure 57, which gives a time history of the "wobble" in the Earth's pole as determined by years of ground-based ranging to the LAGEOS satellite. Figure 58 illustrates the variation in length of day as measured by SLR and its high correlation with independent estimates of atmospheric angular momentum after corrections for known gravitational effects have been made. The system would also permit centimeter-level knowledge of the Eos coordinates in an Earth-based reference coordinate system in support of other Eos missions such as altimetry. The GLRS instrument also has potential as a centimeter-accuracy altimeter for terrain profiling, biomass (tree height) studies, ice-sheet thickness, and marine geoid and sea-state (wave height, period, and direction) measurements. Based on recent aircraft experiments (Abshire *et al.*, 1985), it also looks feasible to relate sea surface roughness to surface wind velocity with precisions greater than currently available from radar altimeters.

Table 26. Preliminary Observations of Tectonic Plate Motion*

Measurement Baseline	Laser Results	Geological Record
North America to Pacific	4 cm/yr ± 1 cm/yr	2 cm/yr
North America to South America	−1 cm/yr ± 4 cm/yr	−1 cm/yr
North America to Australia	−1 cm/yr ± 2 cm/yr	−3 cm/yr
Australia to Pacific	−7 cm/yr ± 1 cm/yr	−6 cm/yr
Australia to South America	6 cm/yr ± 3 cm/yr	2 cm/yr
South America to Pacific	5 cm/yr ± 3 cm/yr	5 cm/yr

*From 3 years of laser tracking of LAGEOS

A Geodynamics Laser-Ranging System (GLRS) instrument on the Eos platform would invert the current SLR measurement scheme. The sophisticated laser-ranging and optical-tracking equipment would be placed on the satellite and would range to inexpensive passive retroreflectors on the ground. This would permit orders-of-magnitude greater density of sites to be installed at selected locales throughout the world and provide, in combination with ground-based systems, a truly global, centimeter-accuracy, geodetic data base for the study of plate tectonics and regional crustal deformation and strain. Most importantly, the spaceborne laser-ranging system offers a permanent on-call surveying capability that can be scheduled for a variety of geophysical observations throughout the world. Thus, the operation of a laser-ranging instrument from Eos to ground-based retroreflectors would permit dramatic improvements in the temporal and spatial resolution with which geodynamic processes can be studied. The measurements would expand current capabilities to measure tectonic plate motion and provide unique opportunities to search for time variations in the plate velocities. Such a system could also provide a capability to observe the precursory geodetic motions believed to occur prior to the onset of large earthquakes and, in a broad sense, provide significant information on the evolution of the Earth.

In the retroranging or geodynamics mode, the GLRS instrument measures the times of flight between the instrument origin and an array of ground-based retroreflectors. This mode is illustrated in Figure 59 for ranging to a number of passive targets distributed in the vicinity of the San Andreas Fault in Southern California. In the altimetry mode, GLRS measures the time of flight between the instrument origin and a diffuse scattering surface such as the ocean, a cloud top, an ice sheet, tree canopy, or solid terrain. In the geodynamics or retroranging mode, the total data set of individual range measurements from Eos to the ground array can be processed to yield the three-dimensional relative coordinates of each target with centimeter accuracies

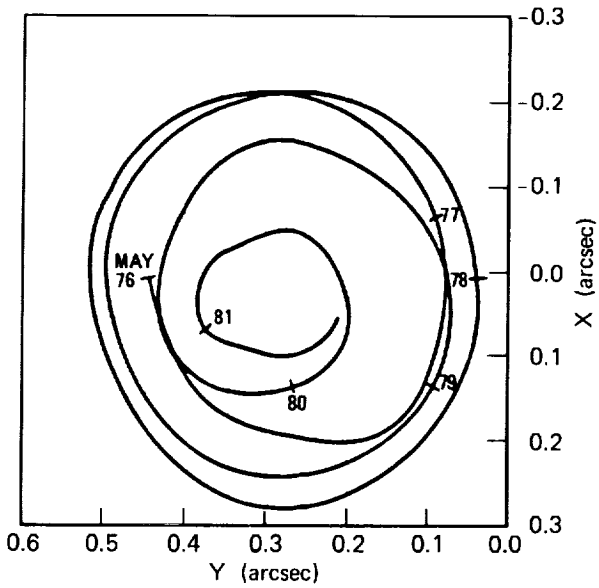

Figure 57. LAGEOS polar motion measurements.

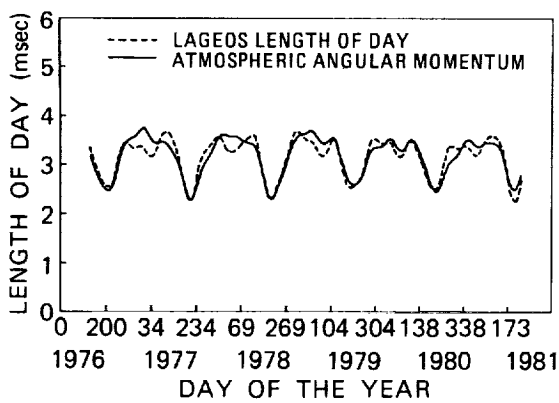

Figure 58. Comparison of atmospheric angular momentum with LAGEOS variations in length of day.

(Kahn *et al.*, 1980). If selected targets in the global array are collocated with known fiducial monuments in an Earth-based geodetic coordinate system, such as ground-based SLR or VLBI sites, then the absolute positions of all of the targets are known in that reference system. This permits centimeter-accuracy geodesy on a global scale. By resurveying the target sites at periodic intervals on subsequent orbits, relative motions can be observed. These relative motions might be indicative of tectonic plate or ice-sheet movement, or the buildup and release of strain in the Earth's crust (e.g., in regions of earthquake risk).

The system can be upgraded at a later date to utilize two laser wavelengths and picosecond resolution streak camera receivers when the latter units reach a space-qualifiable status. This would permit

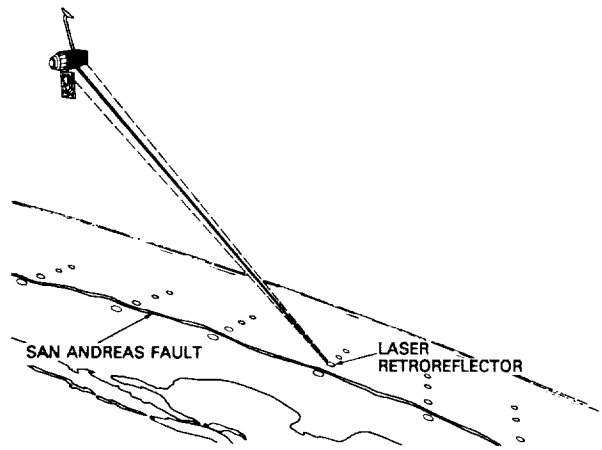

Figure 59. Spaceborne geodynamics laser-ranging system.

a substantial reduction in the atmospheric refraction error, which limits the absolute range measurement accuracy in geodynamics studies to between 5 and 15 mm for a single wavelength system (Abshire and Gardner, 1985). This technology would also permit the measurement of surface pressure over oceans with submillibar accuracies (Gardner *et al.*, 1983; Abshire and Kalshoven, *et al.*, 1983). Table 27 summarizes the capabilities of the basic GLRS instrument in its two modes of operation (retroranging and altimetry) and its upgraded versions. In the system descriptions that follow, the discussion is limited to the basic instrument configuration.

MEASUREMENT OBJECTIVES AND STRATEGY

As discussed in the LASA science issues section, the geodynamic measurement objectives focus primarily on major questions in plate tectonics. The major objectives include:

- Measurement of crustal deformations in the vicinity of seismically active zones at tectonic plate boundaries at spatial scales of 25 to 500 km.
- Determination of the contemporary relative velocities between tectonic plates and tectonic plate interior deformation using a globally distributed set of targets located hundreds to thousands of kilometers apart.
- Measurement of spatial and temporal variation in crustal movements associated with regional scale processes (e.g., earthquake-related processes, land subsidence).

Additional measurement objectives include, among others, terrain mapping, geoid determinations, and precison orbit determination for Eos.

Table 27. Applications of the GLRS Instrument on Eos

Basic Instrument: Ranging Mode	Basic Instrument: Altimeter Mode	Two-Color Upgrade	High-Performance: Atomic Clock Upgrade
Precise Orbit Determination	Centimeter-Precision Altimetry	Submillibar Accuracy Surface Pressure Over Oceans	Subnanosecond Global Time Transfer
Centimeter-Precision Global Geodesy	Ice-Sheet Thickness	Improved Ranging and Altimetry Measurements	Long-Term General Relativity Experiments
Tectonic Plate Motion	Marine Geoid		
Regional Crustal Deformation and Strain	Sea State (Ocean Wave Height and Frequency)		
Earthquake Prediction			
Polar Wobble			
Earth Rotation Rate			
Gravitational Field Studies			
Earth Internal Mass Distribution and Moments of Inertia			
Earth and Ocean Tidal Components			
Ice-Sheet Movement			

The multiple objectives of the geodynamics laser-ranging measurements are satisfied by a strategy that involves ranging to grids of cube-corner retroreflectors arranged with various intersite separations and undertaking resurveys at selected epochs for different locales on the Earth. In the vicinity of a major fault zone where significant strain is accumulating and earthquake occurrence is likely, a greater density of sites and more frequent surveying is required.

In California, the San Andreas fault system marks the boundary between the North America and Pacific plates. Retroreflectors would be placed at sites separated by several tens of kilometers with the intersite separation increasing slowly with distance from the fault. Resurveying of the sites several times a year should be adequate for monitoring strain accumulation and plate motion during times between major seismic events if no significant temporal variability is noted. When significant temporal variability and change in the rate of strain accumulation are detected, more frequent resurveying would be required to study the possibility of a forthcoming earthquake or a seismic deformation process. Surveys would be made on a weekly basis, or more often in certain cases. Similarly, frequent observations would be made subsequent to an earthquake to study how stress changes diffuse into a plate interior. Such studies would contribute to the knowledge of the driving mechanisms for plate motions and earthquakes and the rheology of the subsurface layers of the Earth.

Other candidate locations for high-density grids can be found in the major fault zones in Japan, New Zealand, the Mediterranean, East Africa, the Caribbean, the west coasts of South America, China, and elsewhere.

Away from major fault zones, regional crustal deformations and plate interior deformations will be studied by placing targets at distances ranging from 10^2 to 10^3 km. An average strain rate as small as one part in 10^8 per year, produces a baseline change of 1 mm/yr for a 100 km baseline and 1 cm/yr for a 1,000 km baseline. Thus, yearly resurveys would be appropriate on these baselines. A worldwide network of sites would be desirable, but specific candidate locations for intraplate deformation studies include most of the United States (across the western Cordillera and such physiographic provinces as the Basin and Range, the Colorado Plateau, the Rio

Grande rift, and the Appalachian belt), the rest of North America, Europe, and most of the regions mentioned in the preceding paragraph.

The data obtained from both short- and long-baseline measurements will be used to develop kinematic models of tectonic plate motion. One of the basic science objectives of the measurement program will be to compare these tectonic plate models based on contemporary geodetic data, with existing models based primarily on long-time-scale geologic data.

One of the major advantages of spaceborne geodetic surveying is that rescheduling of observations on selected sites can quickly respond to the needs of the scientific community. This has already been discussed with reference to preseismic and postseismic observations. In general, however, the duty cycle for the ranging observations to cube-corner reflectors is low. Thus, the laser is also available for terrain profiling over continental structures (e.g., mountain belts), over oceans (for mapping both plate tectonic and oceanographic features), and over ice sheets.

The ability of a GLRS instrument to determine spacecraft ephemeris at the centimeter level in the retroranging mode greatly enhances the absolute accuracy of any collocated higher-power altimeter by removing the meter-level uncertainties in spacecraft position. An upgraded dual-wavelength version of GLRS can provide remote surface pressure measurements over oceans as well as parameters related to sea state such as wave amplitude, frequency, and direction (Gardner *et al.*, 1983; Abshire *et al.*, 1985).

Other important geological and geodetic applications of GLRS include the monitoring of lake levels, providing survey control in remote regions of the Earth or for large-scale engineering projects (highways, pipelines, etc.), and monitoring ground subsidence caused by oil or water withdrawal. Under certain circumstances, data from the basic GLRS instrument may also be used in the study of polar motion, variations in length of day (Earth rotation rate), solid earth and ocean tidal components, atmospheric angular momentum, and gravitational field studies. The inclusion of an accurate atomic time standard permits the real-time transfer of time at the subnanosecond level between widely separated clocks eliminating the need for portable clock trips between stations. Such time transfer experiments are also fundamental to experimental verifications of the General Theory of Relativity (Alley, 1983).

A block diagram of the proposed instrument is given in Figure 60. The system consists of three major subsystems: (1) a navigation and attitude determination subsystem; (2) a high-speed, high-accuracy optical-tracking subsystem; and (3) a centimeter-accuracy laser-ranging subsystem. Functional engineering prototypes of the laser-ranging and optical-pointing subsystems, shown in Figure 61, have been designed, fabricated, integrated and tested successfully under an Advanced Laser Ranging project funded by the Office of Aeronautics and Space Technology during the period 1975 to 1983 (Degnan, 1984). Some additional development will be required in selected subsystems, notably the laser transmitter, to achieve fully space-qualified status for the system prior to deployment on the Eos platform.

Navigation and Attitude Determination Subsystems

The navigation and attitude determination subsystem consists of the following components: navigation computer, Inertial Reference Unit (IRU), a GPS receiver, and twin standard NASA star trackers. Updated estimates of spacecraft position, at the few-meter level, are provided periodically by the onboard GPS receiver. The spacecraft position between updates can be obtained by integrating the equations of motion using a simple geopotential field as is currently done in ground-based ranging to satellites. The laser beam divergences planned for GLRS are on the order of tens of arcseconds and illuminate areas on the order of 100 m at the ground. Thus, the few-meter absolute positional accuracy of GPS and the few-arcsecond absolute angular accuracy provided by the star trackers should permit open-loop pointing to the "grapefruit-sized" ground retroreflectors. Nevertheless, the GLRS concept provides for an acquisition sequence if the system fails to detect range returns in the open loop mode. Furthermore, following acquisition of the ground retroreflectors, real-time knowledge of the spacecraft position can be improved to better than a meter by applying a Kalman filter estimation algorithm to the laser range data. An optional monopulse tracker, which determines the location of the image of the return pulse in the receiver focal plane, can be used to generate pointing error commands which keep the target image in the center of the transmitter and receiver fields-of-view.

The requirement for accurate real-time spacecraft position and attitude information is not unique to GLRS. Such information is required by LASA as well as by several passive sensors being considered for inclusion on the Eos platform. Thus, the proposed navigation and attitude determination subsystem can be shared by many instruments.

Optical-Pointing Subsystem

Ground target locations are stored in the computer memory. New target positions or operational instructions can be added via telemetry as required. Knowledge of the spacecraft and target positions and spacecraft attitude permits calculation of azimuth and elevation pointing angles in the

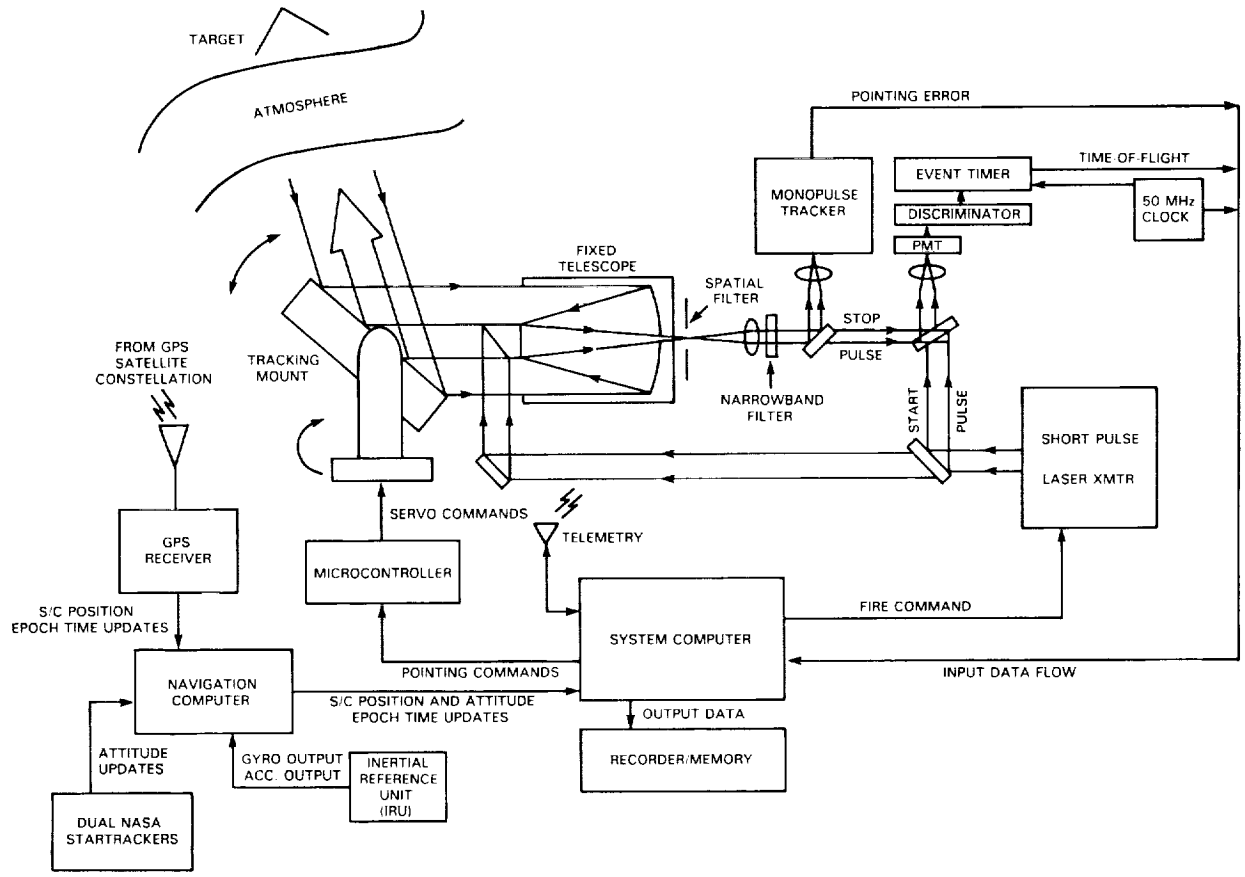

Figure 60. Centimeter-accuracy GLRS spaceborne laser ranging/altimetry.

instrument coordinate system. When a target is within the operating angular range of the instrument (i.e., within 70° of nadir), the system computer enables the firing of the subnanosecond pulse laser transmitter at the desired repetition rate (nominally 10 Hz).

During the pass over the target grid, the instrument typically ranges in a preprogrammed fashion to a given target three times, each for a three-second period: once at low-to-medium elevation on approach, once at high elevation, and once at a medium-to-low elevation as it exits the grid. This procedure, illustrated in Figure 62, strengthens the overall geometry of the measurement and leads to improved baseline accuracies. The optical-pointing subsystem requirements for GLRS are, therefore, somewhat unique. Since the time spent over the target grid is on the order of 10 minutes for suggested Eos altitudes, the pointing subsystem must be capable of slewing rapidly between widely separated ground targets and settling into an arcsecond-level tracking mode within a few seconds of time.

The computational burdens can be greatly reduced through the use of an intermediate microprocessor-based, all-digital controller to drive the optical tracking mount. The GLRS computer provides updates every second or so to the controller in the form of angular position, velocity, and acceleration commands. The controller, in turn, provides detailed commands to the drive motors at rates up to 512 Hz. A prototype of this system was also developed earlier and met all functional design goals including a 200°/sec maximum slew rate, a 500°/sec^2 maximum angular acceleration, and arcsecond tracking accuracy (Zagwodski and White, 1986). In these tests, the microprocessor-based controller drove a 12.5 by 7.5 inch elliptical beryllium flat mirror, which is representative of the telescope receiver aperture required by the GLRS experiment. The small receiver aperture is a consequence of the large lidar cross section (4×10^6 m^2) of the ground retroreflectors. Although the retroflectors are only several centimeters wide, their large lidar cross-section results from their highly directional reflectance, which returns the intercepted signal beam along the incident beam path.

Laser-Ranging Subsystem

The prototype laser transmitter consists of a mode-locked, Q-switched, Nd:YAG laser oscillator, double pass Nd:YAG amplifier, and KD*P

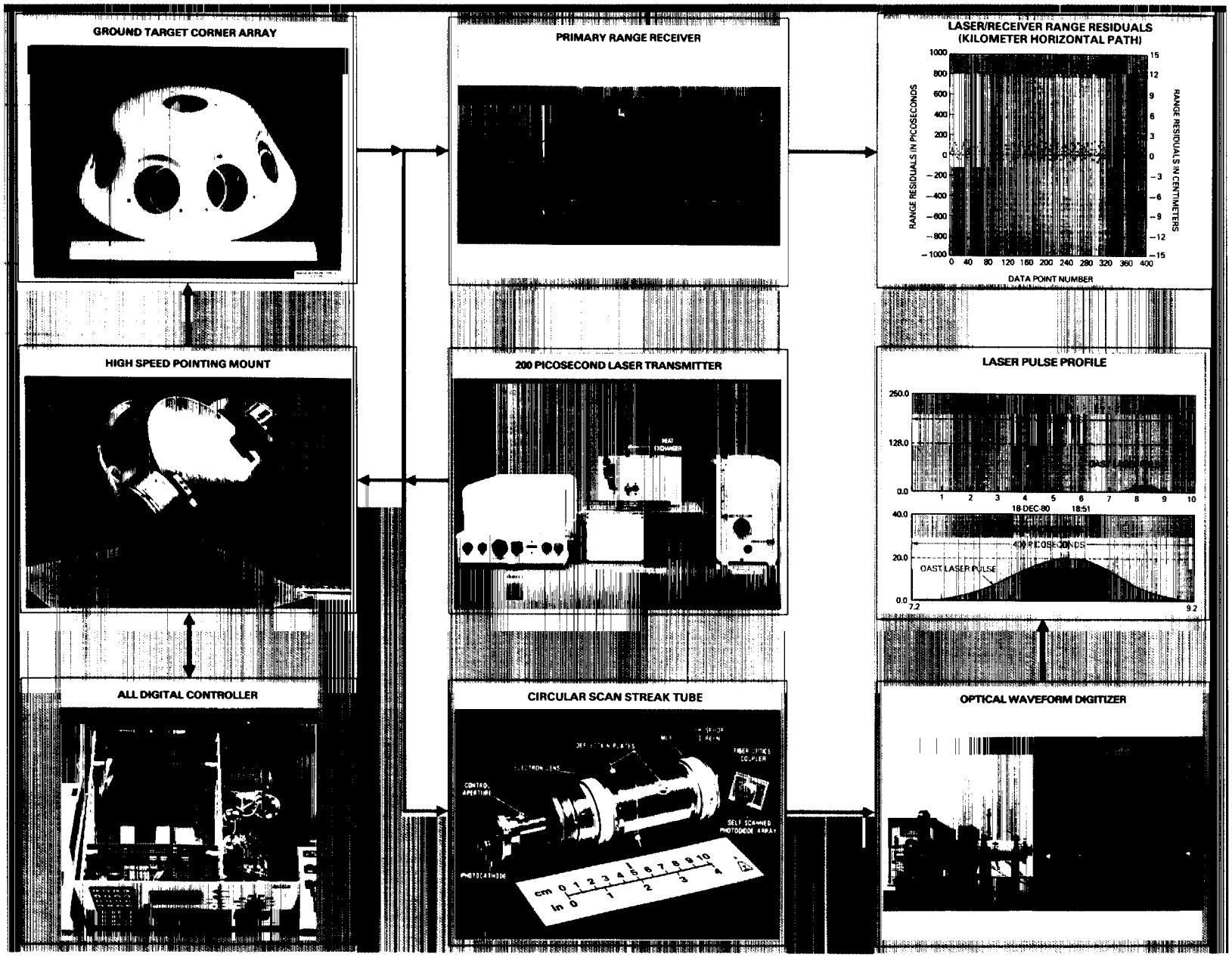

Figure 61. Prototype hardware for spaceborne laser ranging.

ORIGINAL PAGE IS
OF POOR QUALITY

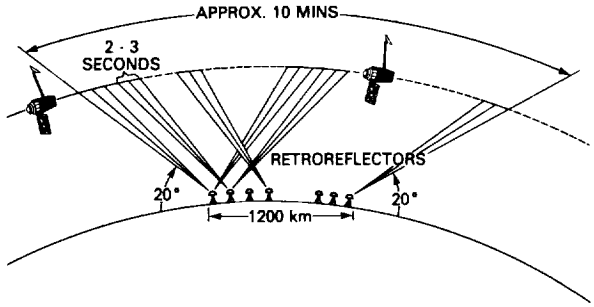

Figure 62. Sequence of events as spacecraft passes over a network to accomplish the ranging mission.

frequency doubling crystal, which produces a single 200 picosecond (ps) pulse containing 10 mJ of energy at a wavelength of 0.532 μm. The prototype laser can be operated at repetition rates up to 20 Hz (Degnan, 1984).

Referring to Figure 60, a small fraction (<1 percent) of the outgoing laser pulse is deflected by beam splitters into the range receiver to start the time-of-flight measurement. The remainder is directed to a high-speed, arcsecond-accuracy optical-pointing mount, which directs the beam at the desired ground target. The pulse propagates through the atmosphere to a passive retroreflector (or altimetry surface). The reflected energy from the target travels back through the atmosphere and is reflected from the pointing mirror into a fixed 7-inch diameter Cassegrain collecting telescope, which images the return onto the photocathode of a high-gain, microchannel plate/photomultiplier tube (MCP/PMT). The range receiver, described in more detail elsewhere (Degnan, 1985), measures signal amplitudes and pulse time of flight. The principal elements of the laser range receiver are a narrow-band (1 nm) spectral filter, a high-speed microchannel plate photomultiplier with a 450 ps impulse response, a low time-walk constant fraction discriminator, and a 20 ps resolution event timer. The signal amplitude information is used to correct for small signal-dependent biases introduced by the discriminator.

Representative GLRS Configuration and Characteristics

Table 28 gives a list of the system components and abbreviations to be used in subsequent figures. Figures 63 through 66 give various views of a representative package. The package includes all of the necessary components with the exception of the GPS receiver. It also includes a redundant transmitter head to double the expected lifetime of the instrument. Note that packaging of the dual laser transmitters and the dual NASA Standard Fixed-Head Star Trackers (FHST) requires essentially the full use of the space available on the 36″ × 69″ optical bench. The FHST are mounted on the optical bench with the same orientation to each other and the coordinate planes as they are when mounted on the optical bench of the Modular Mission Spacecraft (MMS) Modular Attitude Control System (MACS). Table 29 lists the baseline GLRS instrument electrical components along with their weights, operating prime power requirements for a 10 Hz or 1 Hz system, and operating temperature limits. Table 30 gives the standby and operational prime powers required by the system as a function of repetition rate and choice of system computer. Figure 67 shows a representative orbit for a combined geodynamics and ice altimetry mission. Ice altimetry is performed for North and South latitudes in excess of 60°. Geodynamics is performed primarily over tectonically active areas near the plate boundaries. Since the Eos platform will be over the ocean a large fraction of the time and geodynamic processes have a long time scale, the geodynamics application has a very low duty cycle, which helps to conserve laser lifetime. Figure 68 gives the average power per orbit consumed by GLRS as a function of laser repetition rate and duty cycle. The duty

Table 28. GLRS Optical Bench Components

IRU	— Inertial Reference Unit	SHA	— Shutter Housing Assembly
T	— Telescope	P	— Pump
BA	— Beam Aligner	PS	— Power Supply
FHST	— Fixed-Head Star Tracker	CR	— Corner Reflector
LA	— Laser	CP	— Cold Plate
SH	— Shutter	SS	— Sun Shade
RD	— Range Detector	PMA	— Pointing Mirror Assembly
AS	— Angle Sensor (Tracker)	OB	— Optical Bench
AT	— Attenuator	KM	— Kinematic Mount
FL	— Filter	DPTD	— Dual Peak Timing Discriminator
BE	— Beam Expander	LS	— Calibration Light Source
M	— Motor	PFN	— Pulse Forming Network
HX	— Heat Exchanger		

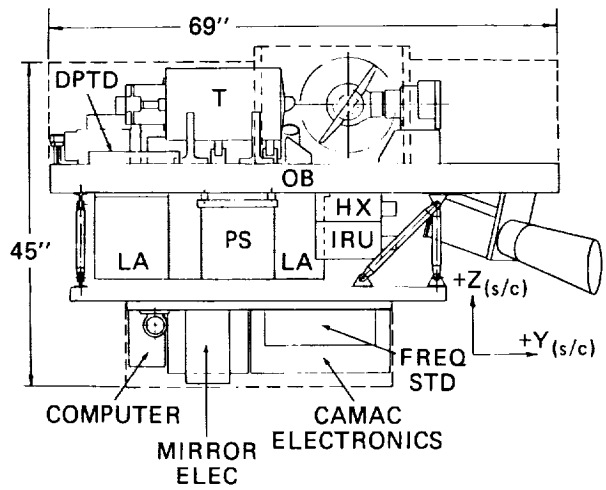

Figure 63. GLRS instrument package view towards $-X_{(s/c)}$.

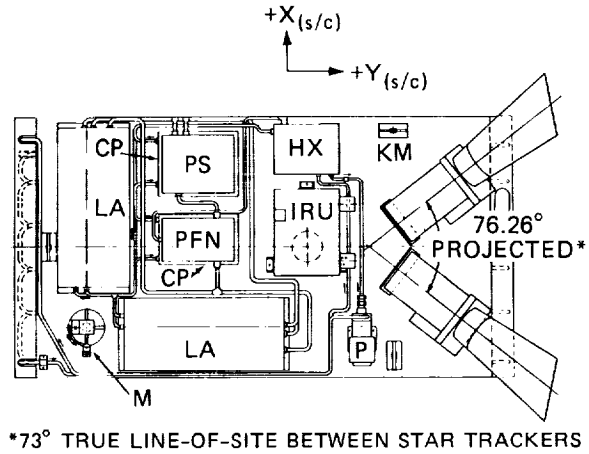

Figure 65. GLRS instrument package view towards $+Z_{(s/c)}$ (upper plate).

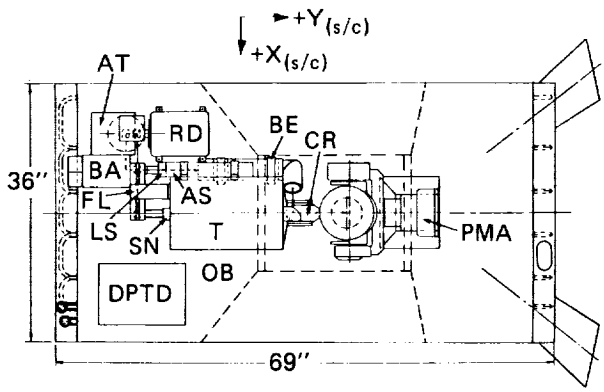

Figure 64. GLRS instrument package view towards $-Z_{(s/c)}$.

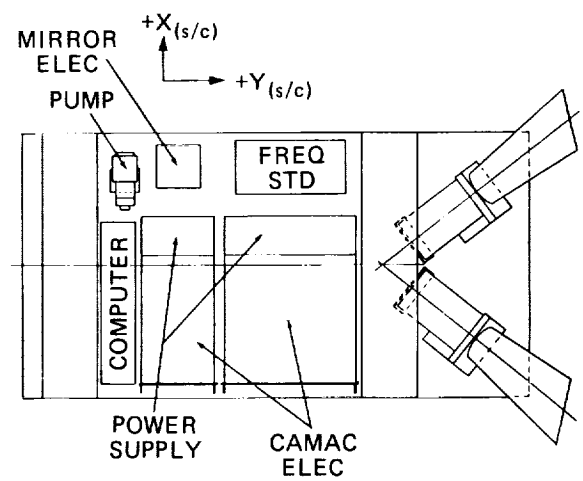

Figure 66. GLRS instrument package view towards $+Z_{(s/c)}$ (lower plate).

cycle for a typical geodynamics/ice altimetry mission is about 2 percent, during which the total standby power is about 118 W and the peak is 789 W. This corresponds to an average power of about 132 W per orbit at a 10 Hz rate. Table 31 summarizes the physical and operating characteristics of GLRS.

DEMONSTRATION EXPERIMENTS AND PERFORMANCE SIMULATIONS

Ground-Based Satellite Laser Ranging

The GLRS instrument is unique among other proposed laser instruments in that laser ranging between the Earth and artificial satellites was first accomplished in 1964 (Plotkin *et al.*, 1965) and the experimental techniques have been highly refined and improved over the years. Today, a worldwide network of over 20 stations routinely ranges to LAGEOS, which is in a 6,000 km high orbit (Degnan, 1985; Cohen and Smith, 1985). The assumed Eos orbital height of only 700 km implies an order-of-magnitude reduction in the range and, hence, four orders-of-magnitude increase in signal level relative to current ground measurements if all other factors remain constant. This permits the use of relatively low laser energies (tens of millijoules), small optical telescopes (7 to 10 inches), modest transmitter divergence cone angles (few tenths of a milliradian), and relatively small and inexpensive ground targets.

Ranging Subsystem Performance

Ground tests of the combined transmitter/range receiver over kilometer-length horizontal ranges

Table 29. Baseline GLRS Instrument Electrical System Components

Components	Wt. (lb)	Operating Power (W)	Operating Temperature Limits (°C) Max/Min
Optical Bench			
Laser Power Supply	40	121/12.2*	50/10
Laser XMTR (2)	108	182/18.3*	25/15
PFN	15	54/5.5*	50/10
**DRIRU	35	21	55/15
Laser Cooling System	28	31	50/0
Range Detector	9	8	30/10
Angle Tracker	5	2	35/5
Two Axis Gimbal Assembly	27	19	50/0
**Fluid Loop Pump	4	9	50/0
**Star Trackers (2)	42	36	45/−5
**DPTD	3	16	30/0
	316	499/178***	25/15
Support Module			
Pulse Amp AV7T	4.6	0.25***	55/−20
Pulse Amp AV8B	4.5	0.25***	55/−20
Sample Hold	3.5	0.10***	70/0
Dual ADC	1.5	0.06***	50/0
RF Attenuator	4.0	0.06***	55/−20
**Event Timer	8.8	12 (1 W standby)	50/0
**Frequency Standard	22.0	24	61/−28
Power Supply	25.0	15 (1 W standby)	50/0
Elect./Mech. Drive Circuits	6.6	0.28***	50/0
****Computer	28.0/2.0	170/20	55/−54
Computer I/F Electronics	2.6	11	50/0
Mirror Electronics	13.0	17	50/0
Digital I/O Circuits	4.6	16	50/0
Matched Filter	4.8	0	85/−54
PM Power Tap	1.5	15	50/0
**Fluid Loop Pump	4.0	9	50/0
	139/113	290/140****	50/0

*10 Hz laser/1 Hz laser
**on continuously
***2% duty cycle assumed
****Norden PDP 11/34 M/Norden LSI-11 M computer

typically yield subcentimeter precisions. The sample data presented in Figure 69, obtained with a modern range receiver similar to that being proposed for GLRS, have a single shot rms value of 5 mm. Figure 70 shows typical results obtained in ground-based field experiments to the LAGEOS satellite, carried out in 1981 with an earlier and inferior receiver configuration, which demonstrated a single-shot precision on the order of 1 to 2 cm. If one forms 50-point averages to reduce the random errors, the rms scatter of the average points about the LAGEOS orbit is reduced to about 3 mm with peak-to-peak variations of less than ±8 mm. Thus, the performance of the ranging subsystem has been demonstrated over slant ranges almost 10 times greater than will be encountered by the GLRS instrument on Eos.

Typical signal levels encountered in the LAGEOS experiments have varied from about three photoelectrons to several tens of photoelectrons. Figure 71 shows that the average signal level expected from the GLRS instrument, based on the

Table 30. GLRS Standby and Operational Prime Powers

Optical Bench Components		Subsystem Support Module Components 290/140 W*	
Standby Power (82 W)		**Standby Power (36 W)**	
Star Trackers	36 W	Frequency Standard	24 W
IRU	21 W	Pump	9 W
Discriminator	16 W	Event Timer/Power Supply	3 W
Pump	9 W		
Additional Power for Ranging (417/96 W)**		**Additional Power for Ranging (254/104 W)***	
Laser System	388/67 W**	Computer	170/20 W**
Two Axis Gimbal	19 W	Electronics	60 W
Sensors, Etc.	10 W	Event Timer/Power Supply	24 W

*Norden PDP 11/34 M/Norden LSI-11 M computer
**10 pps laser/pps laser

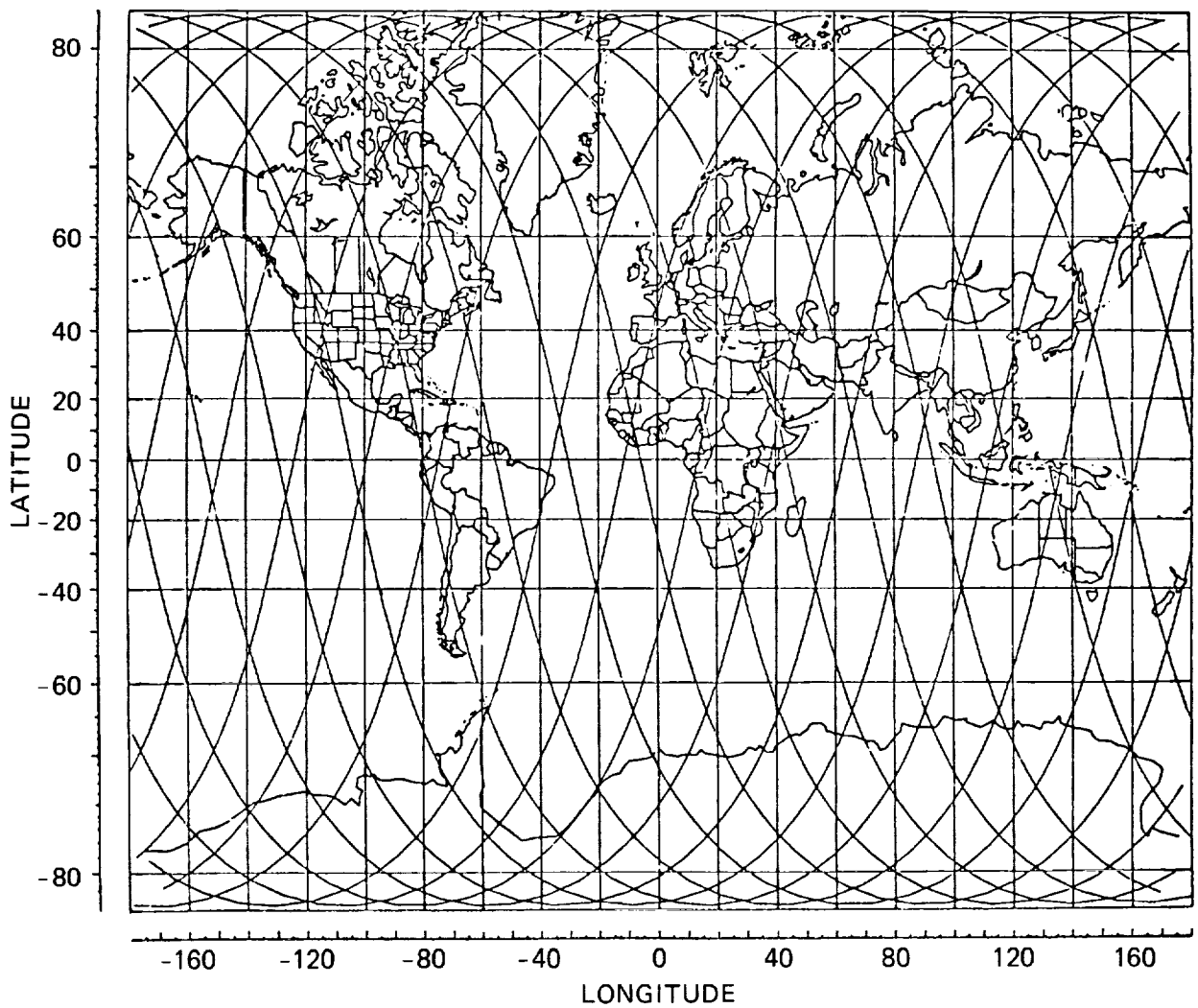

Figure 67. Typical twenty-four hour coverage provided by a sun-synchronous satellite at 700 km altitude.

demonstrated performance of the prototype instrumentation, falls within the same range even if one uses a relatively wide (15 X diffraction limit) transmitter beam divergence of one arcminute (0.3 mrad). The calculation assumes a 700 km orbit and a target cross section of 10^6 (an order-of-magnitude less than LAGEOS). At this altitude, the beam diameter on the ground at nadir is 210 m.

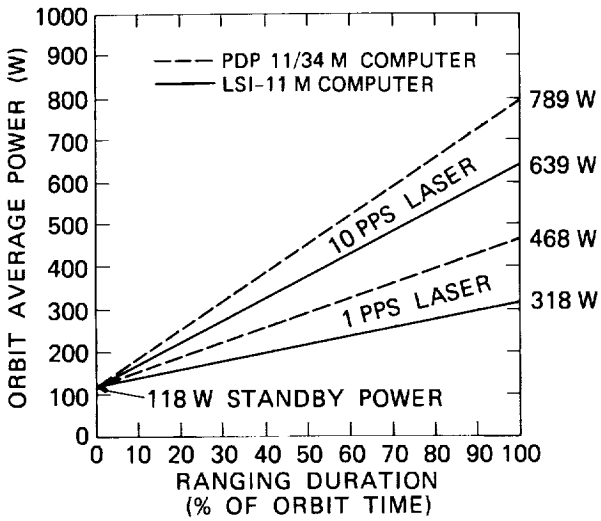

Figure 68. GLRS orbit average power consumption versus ranging duration and laser repetition rate.

Optical-Pointing Subsystem Performance

Figure 72 displays the measured rms tracking accuracy of the prototype pointing system. Except

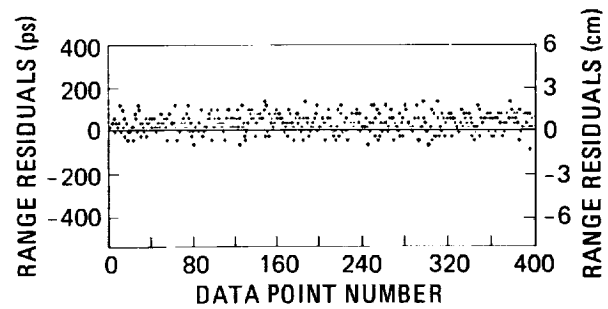

Figure 69. Ranging subsystem performance over 1 km horizontal path. The single-shot standard deviation is 5 mm.

Table 31. Characteristics of GLRS* on Eos

Instrument Component	Component Measure
Instrument Volume	55.4 ft^3 (1.6 m^3)
Instrument Envelope	69″ × 36″ × 45 ″ (can be reconfigured)
Instrument Mass	306 kg (includes redundant laser head)
Telescope Diameter	7 in (18 cm)
Laser Energy Per Pulse	10 mJ
Laser Pulsewidth	200 ps
Repetition Rate	10 Hz
Instrument Peak Operating Prime Power	789 W
Instrument Standby Prime Power	118 W
Orbit Average Power	485 W (for representative combined geodynamics and ice altimetry mission)
Operational Lifetime	Two to three years for representative combined geodynamics and ice altimetry mission
Operating Temperature	15°C to 25°C (determined by actively range mode-locked laser transmitter)

*Ranging or altimetry modes

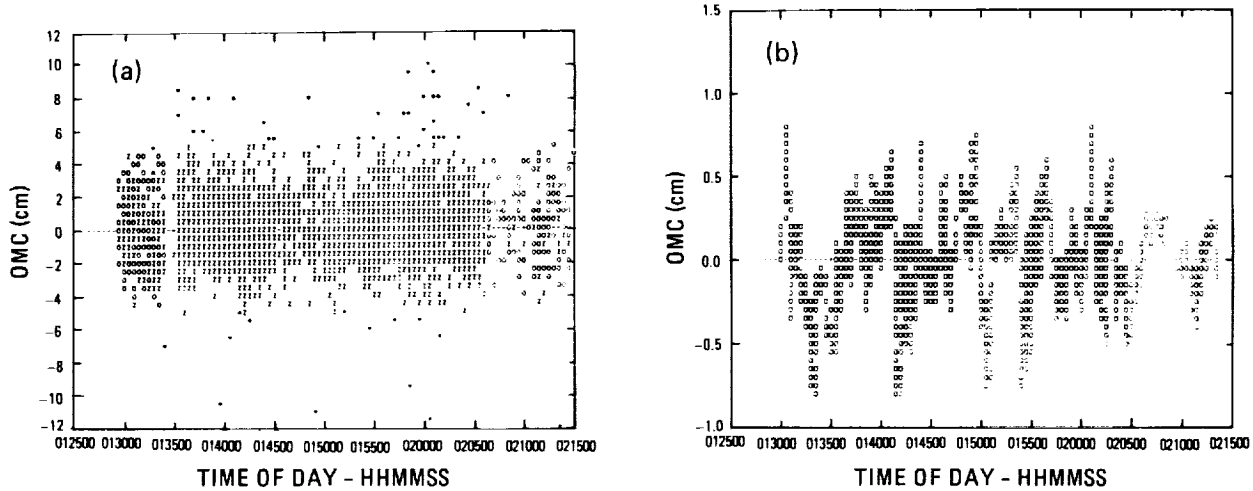

Figure 70. Centimeter-precision LAGEOS range data obtained on October 20, 1981 at 01:29 GMT. (a) Short arc orbital fit of single shot data, observed minus calculated (OMC) range single shot rms: 1.68 cm, number of measurements: 3808, edited: 101 (2.6%); (b) Short arc orbital fit of normal point data (50 pt. average), OMC normal point rms: 0.30 cm.

near the maximum tracking rate of 2°/sec, the tracking jitter is at the subarcsecond level in both the pitch and roll axes. Figure 73 is a plot of the time required by the pointing subsystem prototype to slew between targets and settle with arcsecond accuracy as a function of the angular separation between the targets. From the figure, we see that only 0.7 sec is required for a typical GLRS slew angle of 20°. A more complete written description of the full range of pointing system test results is in preparation (Zagwodski and White, 1986).

Performance Simulations for Eos

As pointed out previously, retroranging data from the GLRS instrument can be used in a number of scientific, engineering, and general surveying applications. Simulations performed to date, however, have been directed primarily to the estimation of crustal strain and strain rate. This application is particularly well suited to the laser retroranging technique because the principal error contribution is a gravity error. The latter error can be largely removed in estimating changes in baseline length from a fixed orbit. Simulations indicate that centimeter-level changes in baseline length can be observed within a 6-day data-taking session.

The results to be discussed are preliminary and are based on some recent simulation results combined with extrapolation from a very extensive study carried out previously (Kahn *et al.*, 1980). It is

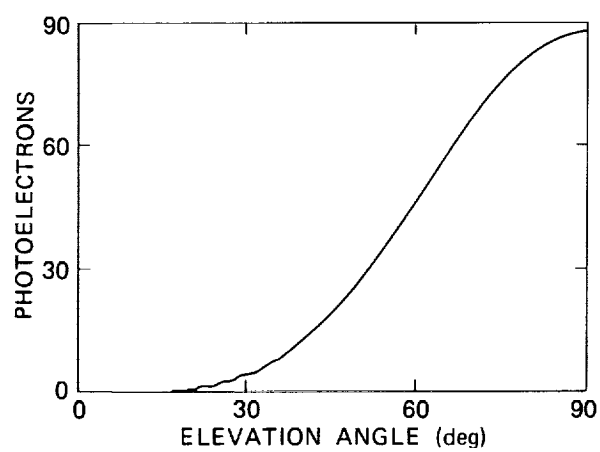

Figure 71. Expected average signal for Eos orbital height of 700 km and 60 arcsec transmitter beam divergence.

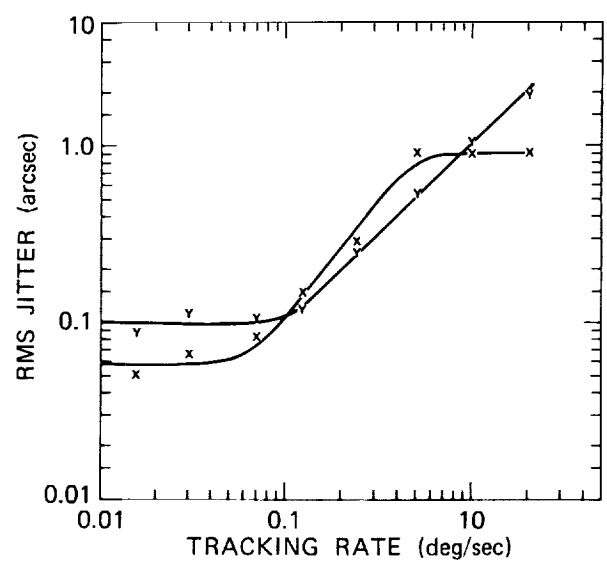

Figure 72. Roll (x) and pitch (y) tracking jitter.

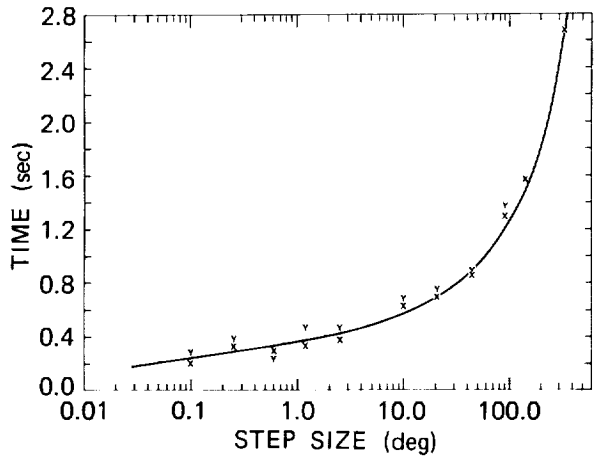

Figure 73. Roll (x) and pitch (y) axes step times.

assumed in the simulation that 150 retroreflectors are distributed over Southern California with 50 km spacings and that cloud cover obscures the targets 50 percent of the time. Table 32 gives the baseline accuracy as a function of baseline length for an Eos platform at an altitude of 700 km and in a near-polar orbit of 100° inclination. As one can see from the table, an absolute measurement accuracy of 3 cm is achieved over baselines of about 1,200 km in length. Gravity uncertainty is the dominant error source. In a long-duration mission, it may be possible to reduce the gravity uncertainty to about 1 cm, and this possibility is currently being studied.

In spite of the effects of gravity uncertainty on the absolute measurement of baseline length, it is possible to detect subcentimeter changes in baseline length over 1,200 km baselines as illustrated by the precision numbers in Table 33. It is the changes in baseline length that lead to estimates of tectonic plate velocities and strain rates. Figure 74 shows the elongation rate precision for a 50 km baseline as a function of the measurement program duration T (Kahn *et al.*, 1980). For the calculation of elongation rate precision, a survey period T_s of 6 days was assumed, and an interval between surveys, the re-survey period T_R, of 6, 14, and 30 days was chosen. As can be seen from the figure, GLRS has the capability of determining elongation rates on individual lines to a precision of better than one part in 10^8 per year over a 2.5- to 3-year mission and one part in 10^9 over 10 years. In a region of strain accumulation, surveys on a network of retroreflector sites can be used to determine the components of the strain rate tensor to a greater level of precision (Cohen and Cook, 1979). The precision is not increased significantly by making more frequent measurements (i.e., reducing T_R), implying that the instrument can operate at a low duty cycle, thereby extending the mission lifetime without sacrificing the science objectives.

SYNERGISTIC SCIENCE

The measurements made by GLRS are complementary to those made using other techniques. The crustal movement measurements provide a densification of the existing network of ground-based SLR and VLBI sites. They would extend well beyond the

Table 32. Standard Deviation of Baseline Estimation Error*
(California Simulation Accuracy 700 km Orbit)

Baseline Length (km)	Noise (cm)	Gravity (cm)	Atmospheric Refraction (cm)	Measurement Bias (cm)	Solar Radiation Pressure (cm)	Drag (cm)	Root Sum of Squares (cm)
131	0.1	0.6	0.1	0	0	0	0.6
303	0.1	1.1	0.1	0	0	0	1.1
591	0.2	1.6	0.15	0	0	0	1.6
847	0.2	2.0	0.2	0	0	0	2.2
1,204	0.3	3.0	0.2	0	0	0	3.0

*Assumptions:

Orbit	
Mean Altitude	700 km
Inclination	100°
Observation Period	6 days
Cloud Cover	50%
Number of Retroreflectors	150 at 50 km spacing
Measurement Noise	±2 cm single pulse, 10 pulses/sec
Measurement Bias	0.3 cm
Gravity Uncertainty	Goddard Earth Model (GEM) 10 covariances (l, m = 22)
Atmospheric Error Model	2 parameter
Pressure Noise	±1.0 mbar
Bias	0.33 mbar
Temperature Noise	±1.4°C
Radiation Pressure	33% error
Atmospheric Drag	22% error
Area/Mass	0.0046 m^2/kg

Table 33. Precision in Determination of Changes in Baseline Length* (California Simulation Accuracy 700 km Orbit)

Baseline Length (km)	Noise (cm)	Gravity (cm)	Atmospheric Refraction (cm)	Measurement Bias (cm)	Solar Radiation Pressure (cm)	Drag (cm)	Root Sum of Squares (cm)
131	0.2	0.1	0.12	0.01	0.00	0.00	0.3
303	0.3	0.1	0.15	0.02	0.00	0.00	0.4
591	0.3	0.1	0.21	0.03	0.00	0.00	0.5
847	0.4	0.5	0.25	0.04	0.01	0.00	0.7
1,204	0.4	0.8	0.33	0.05	0.03	0.00	1.0

*Assumptions:

Orbit	
Mean Altitude	700 km
Inclination	100°
Observation Period	6 days
Cloud Cover	50%
Number of Retroreflectors	150 at 50 km spacing
Measurement Noise	±2 cm single pulse, 10 pulses/sec
Measurement Bias	0.3 cm
Gravity Uncertainty	GEM 10 covariances (l, m = 22)
Atmospheric Error Model	2 parameter
Pressure Noise	±1.0 mbar
Bias	0.33 mbar
Temperature Noise	±1.4°C
Radiation Pressure	33% error
Atmospheric Drag	22% error
Area/Mass	0.0046 m^2/kg

capabilities of conventional local surveys, which are very labor intensive and of limited utility over long baselines or in mountainous regions. The GLRS target grids should be designed to complement, rather than compete with, those that will be surveyed with highly mobile receivers operating on microwave signals from the constellation of GPS satellites. The altimetric measurements would provide high-resolution topographic mapping to complement the coarser data obtained from microwave altimeters. Gravity and magnetic data available from current sources and from the planned GRM satellite can be used in combination with GLRS data to provide a more complete picture of the geodynamics of the Earth than could be inferred from either data set taken by itself.

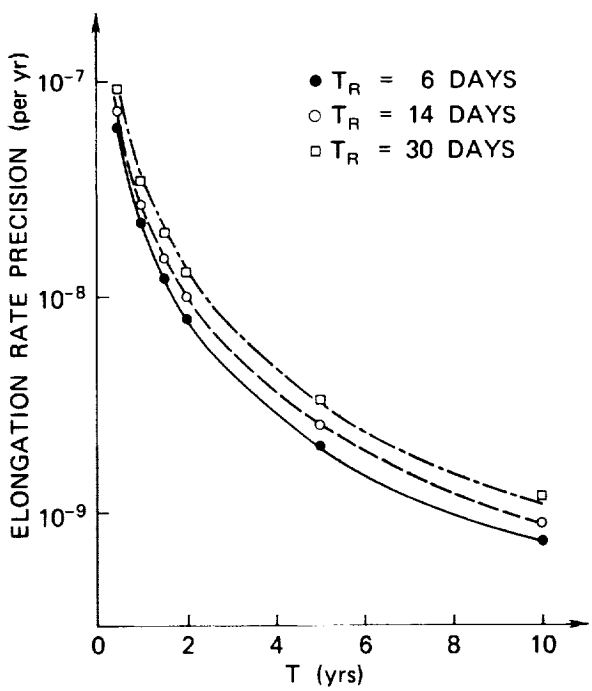

Figure 74. Elongation rate precision versus total measurement periods, where T = time period between first and last measurement (years), and T_R = resurvey period (days). Assumptions: Survey period (T_S): 6 days, baseline distance (D): 50 km, baseline precision: 0.25 cm.

The centimeter-accuracy ephemeris knowledge provided by GLRS also enhances the absolute measurement capabilities of other onboard altimeters, such as the high-power LASA laser altimeter or collocated microwave altimeters, by removing few-meter-level uncertainties in the satellite orbit.

The capability of the GLRS instrument for centimeter-level range precision on arbitrary slant paths to specific Earth targets can provide extremely important synergism with the LASA altimeter and its nadir-only, moderate-resolution range measurements. The GLRS range precision based on short-pulse laser and subnanosecond receiver technology is up to one order-of-magnitude better than that of the LASA altimeter. As such, it can provide occasional calibration of the LASA altimeter during simultaneous burst-mode tracking of the same ice-sheet, terrain, or ocean surface targets. The objective is removal of biases to the centimeter level in LASA altimeter data sets. The precise off-nadir pointing capability of GLRS can also provide cross-track or limited scanning to supplement nadir-only

altimeter data over ice sheets. For example, the use of GLRS to acquire range measurements to a small set of surface grid points on sequential orbits can provide significant improvement in knowledge of the spacecraft orbital position. This in turn is essential for removal of biases in LASA altimetry data in order to produce an accurate map of ice-sheet topography or land targets of high interest.

The conversion of GLRS time-of-flight measurement to a centimeter-accuracy, absolute geometric range with the basic, single wavelength GLRS instrument requires the application of atmospheric models to correct for atmospheric refraction effects. The inputs to these models are provided by surface measurements of atmospheric pressure, temperature, and relative humidity. In many seismically interesting regions of the Earth, such as Southern California, this data can be provided by existing meteorological stations. In other less-developed regions of the world, it may be necessary to augment the existing meteorological data through the use of a small number of automated meteorological stations located within the target grid. The use of atmospheric models presently limits the absolute range accuracy of the basic GLRS instrument to about 1 cm (Abshire and Gardner, 1985). However, vertical profile data on atmospheric pressure, temperature, and water vapor obtained by a collocated LASA or other atmospheric sounder instrument could be used to correct for the effect of atmospheric refraction and eliminate the need for ground-based meteorological stations.

Advanced versions of the GLRS instrument are currently under development. They utilize dual-wavelength transmitters and picosecond-resolution streak camera range receivers and will be capable of directly measuring the atmospheric delay and achieving few-millimeter absolute range accuracies (Degnan, 1985). Such an upgraded GLRS instrument would not require ancillary meteorological data. The upgraded system could also provide surface pressure over oceans with millibar accuracy (Abshire and Kalshoven, 1983; Gardner *et al.*, 1983). The feasibility of this technique has been firmly established by a recent aircraft experiment (Abshire *et al.*, 1985) in which surface pressure was measured with a resolution of 3 mb. The system also detected centimeter-level capillary waves that can be related to surface wind.

V. HERITAGE, CONCEPTS, AND LASER TECHNOLOGY ASSESSMENT

LIDAR HERITAGE

The development of the pulsed ruby laser in 1960 made it possible to use lasers to study the atmosphere and to determine range to a target. Historically, lasers made an extraordinarily rapid transition from their laboratory demonstration in 1960 to their application in lidar atmospheric measurements made in 1963. The following section provides a brief history of this development up to the present.

For lidar-ranging applications, measurements to Earth satellites equipped with retroreflector arrays rapidly became an important application of remote-sensing technology. As early as 1964, measurements of distance from a ground-based laser-ranging station to the Beacon-Explorer series of satellites were routinely accomplished with a high-power, long-pulse, low-repetition rate ruby laser. These early distance measurements achieved precisions of several meters. The following years produced a rapid improvement in ranging precision of two orders of magnitude to the present value of 1 to 2 cm. This was accomplished through development of improved, short-pulse Nd:YAG lasers, faster timing electronics, better satellite tracking mounts, higher repetition rates, and increased detection sensitivity to the level of the single photoelectron.

During this same period, the potential of the laser ranging capability to observe the atmosphere was also recognized. The earliest atmospheric lidar measurements utilized elastic backscatter of the laser pulse to range to clouds and aerosol layers. Early efforts explored high-altitude stratospheric and mesospheric layers. The influxes of meteoric and volcanic material were easily recorded and studied. More advanced lidar techniques were soon developed to include resonant fluorescence scattering from mesospheric sodium and potassium layers, for example, which provided feasible measurements of high-altitude dynamics. The differential absorption technique was applied to the measurement of water vapor by temperature tuning a pulsed ruby laser through the water absorption region near 0.6943 μm. Raman scattering was also applied to tropospheric water vapor measurements, nitrogen density measurements, and aerosol extinction measurements. At the same time, carbon dioxide lasers provided the means for coherent Doppler lidar wind measurements.

The original ruby lidar laser source emitted at 0.6943 μm. This was soon complemented by dye lasers that allowed measurements such as sodium resonance to be made. Neodymium:glass and YAG lasers also became available, emitting at 1.06 μm. Electro-optical crystals to double and triple these frequencies allowed routine operation at 0.53 and 0.3472 μm, among others, for many new applications. More recently, solid-state lasers have been used to pump various dyes to produce other wavelengths for various constituent measurements such as water vapor, nitrogen dioxide, and ozone. By the 1970s, these measurements were being made by various researchers throughout the world, mostly from fixed sites. The Apollo Program of lunar landings in 1969 and the early 1970s provided a unique opportunity to further the role of laser ranging in space applications. A laser-altimeter instrument was included in the complement of instruments in the Apollo Command and Service Module in lunar orbit. Successful operation of this first space-based, remote-sensing instrument was achieved on the three missions attempted: Apollo 15, 16, and 17. This laser-altimeter instrument was based on the solid-state, flashlamp-pumped, Q-switched ruby laser that is the forerunner of present-day Nd:YAG technology. The Apollo Program also resulted in the placement of several retroreflector arrays during the first lunar landing. This was a prime experiment on the first landing (Apollo 11). The result has been 16 years of continuous laser-ranging data for the Earth-to-Moon link and a major milestone in the progress of laser-ranging techniques and applications.

As lidar technology continued to progress and expand, airborne measurements began. Aerosol, cloud, and DIAL water vapor and ozone measurements were among the earliest airborne applications. Figure 75 depicts the evolution of altimetry and surface-ranging lidar, and Figure 76 depicts the evolution of lidar for atmospheric measurements from ground-based measurements in the 1960s to Eos in the 1990s. The high-altitude programs on the WB-57 and ER-2 aircraft have shown the feasibility of autonomous lidar operations and modular concepts important to space measurements. The Cloud Lidar System (CLS) has already flown on the WB-57 and ER-2 to map clouds. This has been done simultaneously with radiometers and other instruments aboard the ER-2 to provide synergistic data sets. A balloon-borne frequency-doubled dye laser system, operating at 0.282 μm and pumped by a frequency-doubled Nd:YAG laser, has autonomously measured stratospheric OH radical profiles using the resonant-fluorescent technique, and ozone via the DIAL technique. The Lidar Atmospheric Sensing Experiment (LASE) program is scheduled for flights beginning in 1988-1989. LASE will make DIAL measurements of water vapor and aerosols.

The obvious next step in lidar evolution is to show its feasibility in space, verifying on-orbit

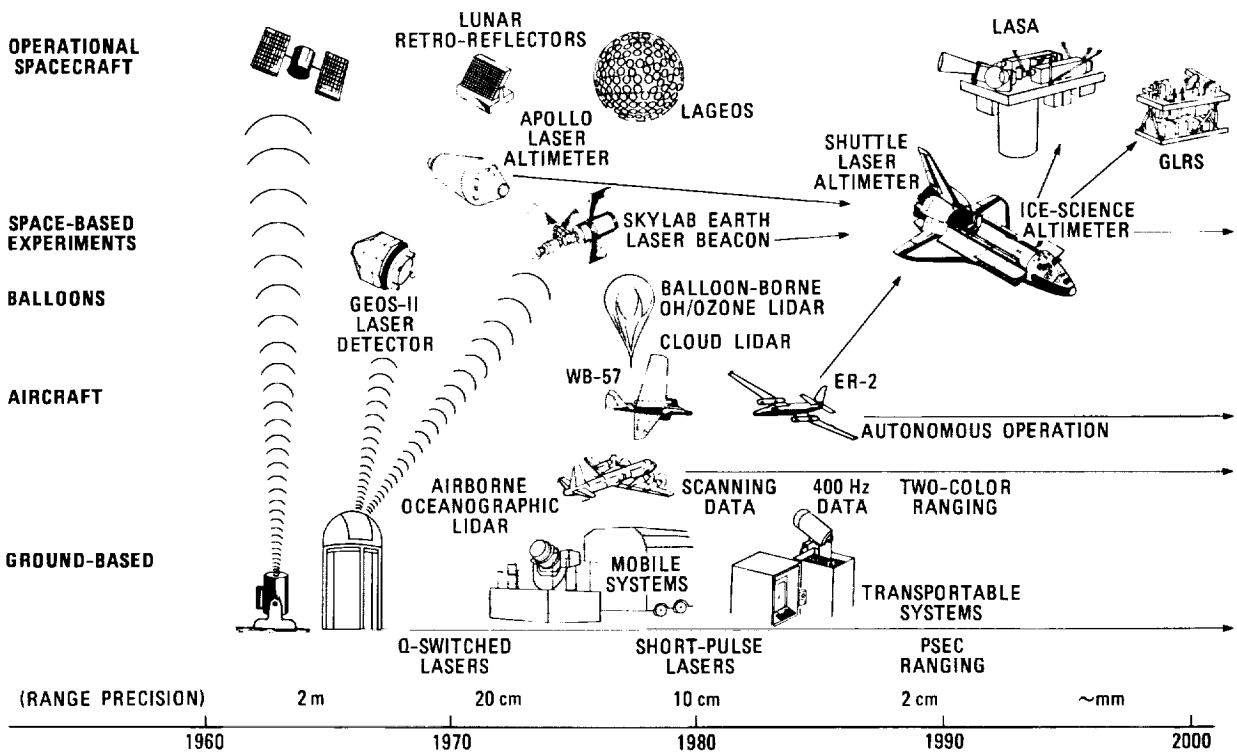

Figure 75. NASA laser-ranging evolution.

autonomous lidar operations, data acquisition, and data processing. An experiment called LITE (Lidar In-Space Technology Experiment) is being readied for flight aboard the Shuttle in 1990-1991. LITE will utilize three wavelengths at 1.06 μm, 0.53 μm, and 0.355 μm to measure clouds, stratospheric and tropospheric aerosols, tropopause height, the PBL height, and temperature profiles from cloud top to about 40 km. The above chronology provides the heritage for the LASA measurement objectives. The following sections of this chapter present the discussion of lidar instrument concepts and a discussion of their technological feasibility. The final section of this chapter shows the match between the capabilities of the lidar systems and the LASA science objectives.

INSTRUMENT CONCEPTS

Key technical criteria for an Eos-based lidar system with an orbit of 700 km and a 1-year to 2-year time period between servicing operations are: (1) high electrical "wallplug" efficiency (i.e., the laser and all its ancillary equipment should have a total efficiency >2 percent); (2) the laser system should be fault-tolerant and capable of pulsed operational lifetime $>10^8$ shots; (3) for several atmospheric sounder experiments, the laser must operate at high pulse energies in a narrow spectral band; and (4) the laser must be able to produce the wavelengths, pulsewidth, and frequency bandwidth required for a particular lidar measurement without compromising criteria (1) through (3). As a note of caution, one can find reported performances from a laser satisfying criteria (1) through (3) separately, but when the whole laser system is considered in a configuration for the LASA experiments including criterion (4), severe compromises may be necessary to meet Eos platform requirements.

The instrument requirements for atmospheric sounding and altimetry and for retroranging are significantly different and are, therefore, presented separately. As indicated in Chapter II, the atmospheric measurements will require a nadir-looking telescope of approximately 1.25 m diameter and a laser pulse energy range of 0.1 to 1 J. Figure 77 is a preliminary drawing of a concept for the atmospheric sounding and altimeter package (LASA). This conceptual view of LASA consists of a 1.25 m telescope and several tunable lasers. LASA would also include thermal control and signal conditioning electronics, as well as electronics for interfacing with the Eos data system.

Figures 63 through 66 depict a preliminary drawing of the retroranging package (GLRS). The retroranging package will consist of three major subsystems: (1) a navigation and attitude determination subsystem; (2) a high-speed, high-accuracy optical-tracking subsystem; and (3) a centimeter-

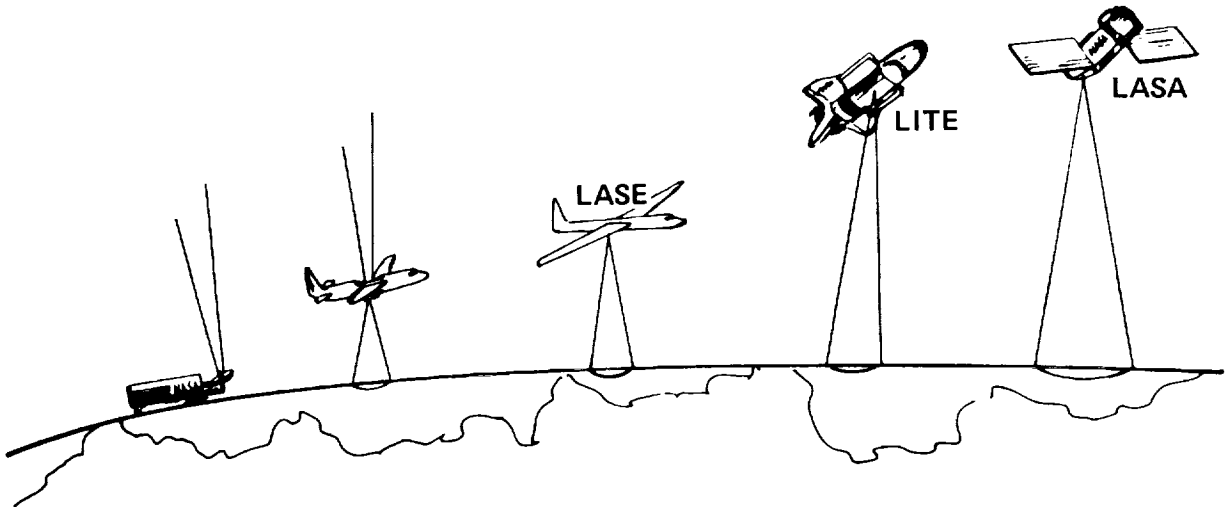

	FIRST MEAS.	λ's	LASER (Tunable*)	MEAS. SPECIES
GND Based 48 in.	1970	2	Ruby (694 nm, 347 nm)	Aerosols/Molecular Backscatter, Water Vapor
Aircraft Electra/990	1978	3	Ruby, YAG, YAG/Dye (1060, 720*, 694, 600*, 530, 347, 300* nm)	Aerosols/Water Vapor/ Ozone
LASE/ER-2	1988	3	Alexandrite (720*)	Water Vapor/Aerosols
LITE/Shuttle	1988	3	YAG (1060, 530, 355 nm)	Aerosols/Density/T
LASA/Eos	1994	$\geqq 3$	–	Aerosols/Clouds/Altimetry Density/Water Vapor/T

Figure 76. NASA lidar atmospheric measurements evolution.

accuracy laser-ranging subsystem. The optical subsystem includes a rapidly articulated telescope with 18 cm diameter aperture. The laser required for this application would have 10 mJ/pulse with a 10 Hz repetition rate.

There is a technology requirement for long-lifetime lasers (5×10^7 to 10^8 shots) with high reliability and a wallplug efficiency in excess of 2 percent. For example, a lidar system operating for 1 year at 5 Hz and a 25 percent duty cycle requires 4×10^7 shots. (Wallplug efficiency is the ratio of laser power at the specified wavelength and bandwidth to the input electrical excitation power. In this context, it excludes power requirements for subsystems such as coolers, calibration systems, power conditioning units, or other auxiliary subsystems for a lidar transmitter requiring electrical energy.) A major power drain for a space laser is the pumping mechanism to create the population inversion necessary for obtaining laser operation in either the gas, liquid, or solid-state laser media. For gas lasers, the conventional excitation mechanism is electrical discharge in the gaseous medium. Wallplug efficiencies of 3 to 5 percent are feasible. For solid-state laser materials, optical pumping with flashlamps is the conventional excitation mechanism. Wallplug efficiencies in pulsed Nd:YAG, the most advanced solid-state material, have been reported to be 1 percent at 1.06 μm.

In the following sections, an overview of the status of laser technology will be presented. The focus will be on those classes of lasers with potential to operate at moderate laser powers (approximately 0.1 to 1 J/pulse at 10 Hz repetition rate) for the Eos lidar experiments described in this document. Laser sources that appear to be too early in technology development for the Eos era are excluded, although it must be recognized that laser technology is emerging rapidly. Three different classes of lasers, in principle, have potential to serve as laser sources for LASA experiments: gas, liquid, and solid-state lasers. Eos platform requirements for overall wallplug efficiencies, lifetime, and other considerations (weight, volume, cooling) will eventually dictate

ORIGINAL PAGE IS
OF POOR QUALITY

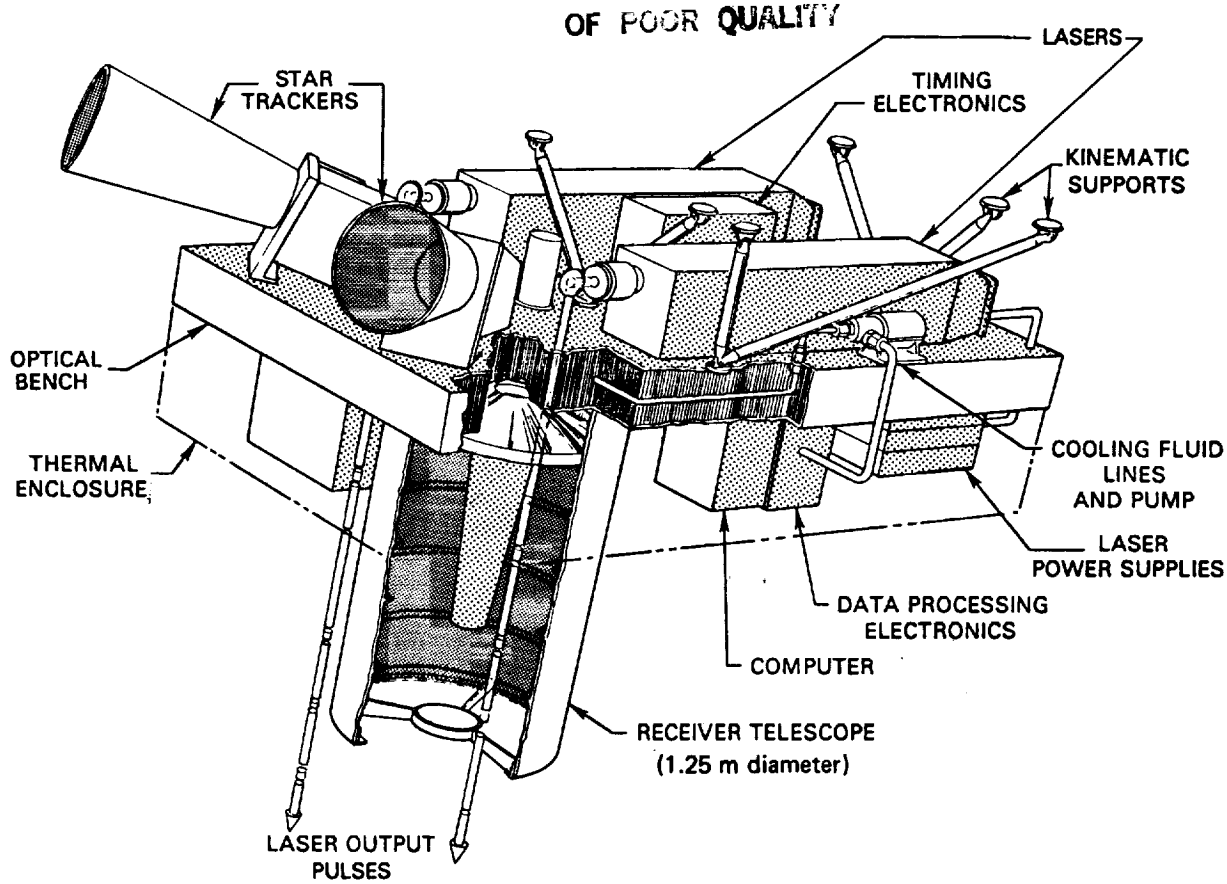

Figure 77. Preliminary drawing of the LASA package.

selection of those Eos laser transmitters that meet the scientific performance requirements of the experiments.

LASER TECHNOLOGY ASSESSMENT FOR ATMOSPHERIC MEASUREMENTS

The laser technology required to measure atmospheric structure and composition parameters differs from that required for altimetry and retroranging applications. Several of the LASA science objectives addressing atmospheric measurements use the DIAL technique. This technique utilizes laser radiation at two wavelengths, one situated at the specific wavelength of an atmospheric absorption feature and the second at a specified nearby "window" wavelength. To accommodate these requirements necessitates lasers which operate at the wavelengths of the absorption features and are accurately tunable remotely to specific lines. Wavelength tunability is required at very high precision for two reasons. Firstly, the accuracy of the DIAL determination of an atmospheric parameter is dependent upon the strength of the absorption feature. Laser sources used in these DIAL applications need to be selectively tunable to selected line strengths for measurements in different altitude bands of the atmosphere. Secondly, due to minute changes in system characteristics, these laser systems may need to be returned with great precision to their proper spectral positions. On the other hand, altimetry and retroranging applications simply require lasers which operate in any one of a number of atmospheric window regions in the visible or near-infrared. The only tunability required in the latter applications is that necessary to minimize atmospheric absorption. The altimetry and retroranging applications require, however, pulse durations on the order of 10 ps as opposed to the 10 ns required for any of the atmospheric measurements.

The current sources of tunable narrow-band radiation over the wavelength region of interest to the LASE experiments are:

- Liquid lasers
- Solid-state lasers
- Gas discharge lasers

Liquid Lasers

Dye lasers are liquid lasers that can be pumped with flashlamps or optical pumping with other laser sources. Typical energy conversion efficiencies for

dye lasers run from 5 to 40 percent, depending upon the dye material, the bandwidth, and the optical cavity configuration. Current flashlamp lifetimes have been demonstrated to 10^7 shots. Dye lifetimes are typically on the order of 10^5 shots, which means that even if laser pumping is used (e.g., excimer laser, which has a demonstrated lifetime of 10^8 shots), dye lasers will not be suitable for Eos without new developments that maintain the integrity of the dye scrubber and replenishment concepts that maintain the integrity of the dye lasing medium. Furthermore, the spectral purity required (better than 99.5 percent) cannot currently be met by high-pulsed-energy dye lasers.

Solid-State Laser Technology

Solid-state lasers use either crystalline lattice or glassy materials as the lasing substance. Solid-state lasers may be divided for the purposes of this discussion into two classes: non-tunable and tunable. The non-tunable lasers of interest are Nd:YAG and Nd:glass.

The Nd:YAG laser is a key technology for use by LASA experiments, both as a primary source for non-tunable applications and as a pump source for tunable wavelength energy sources. Its attractiveness is heightened by its ability to be pumped by long-life semiconductor lasers.

The high optical quality of the YAG crystal coupled with the high gain of the 1.064 μm transition has made Nd:YAG the solid-state laser of choice. It has been demonstrated that Nd:YAG can be pumped with pulsed and with continuous wave (cw) flashlamps, that it can be Q-switched and mode-locked and operate cw in a single axial mode. Efficient harmonic generation has been accomplished for both cw and pulsed Nd:YAG sources.

Progress in Nd:YAG has overshadowed the progress in other solid-state laser media. However, there have been efforts to develop other laser crystal hosts and other laser ions for various new wavelengths. Recent examples of new laser host and laser ion development programs include YLF, Alexandrite, and chromium-doped garnet lasers. At this time, it is not clear to what extent any of these new solid-state lasers will compete with the well-established Nd:YAG technology.

The Nd:YAG or Nd:glass laser sources operate at 1.064 μm and at 1.055 μm, and they meet the requirements of several LASA experiments not requiring tuning to specific absorption wavelengths. For other experiments, the fundamental laser frequency must be converted to the harmonic frequencies. At present, this can be achieved with second-harmonic generation at 50 percent energy conversion efficiency. For operation of the laser source at a high peak power with Q-switching, KDP (or KD*P) is usable as the nonlinear crystal. For harmonic generation at either lower power pulses or for harmonic generation of a cw source, KTP or $MgO:LiNbO_3$ crystals must be used. These nonlinear oxide crystals are stable and have long intrinsic lifetimes. However, processes at the surface, enhanced by intense radiation, may lead to shortened useful lifetimes. Fortunately, nonlinear devices using both $LiNbO_3$ and KDP have been operated in commercial laser sources for over 8 years and lifetime data have been accumulated. In addition, new nonlinear crystals such as BaB_2O_4 have been studied and show promise for harmonic conversion of the 1.06 μm source to the third and fourth harmonics. New, more rapid growth techniques have been discovered for KTP, which should yield higher quality and larger crystal cross sections. The accumulated experience and recent advances in nonlinear frequency conversion reduce the risks of applying this technology for LASA experiments.

Tunable solid-state lasers include Alexandrite, titanium-doped sapphire and Cr:GGGS. Titanium-doped sapphire and Alexandrite are the most advanced members of a recently developed class of tunable solid-state (vibronic) laser materials. Alexandrite is tunable in the near-infrared portion of the spectrum between 0.7 and 0.8 μm, and titanium-doped sapphire is tunable in the range 0.68 to 0.95 μm. Alexandrite lasers pumped by flashlamps have been demonstrated with energies up to several hundred millijoules. Titanium-doped sapphire has a short energy storage time, and can be pumped by a Nd:YAG laser operating at 1.06 μm and doubled to 0.532 μm. The long-term prospects for Alexandrite are uncertain due to relatively poor wallplug efficiencies. In addition, Alexandrite lasers cannot be directly pumped with currently available semiconductor lasers, and, if long lifetime is to be achieved, breakthroughs in flashlamp development or semiconductor laser technology must be realized.

The measurement of water vapor profiles and measurements of temperature and pressure in the atmosphere require the use of a laser transmitter tunable from 0.72 to 0.94 μm. In addition to Alexandrite and titanium-doped sapphire, CR:GGGS and related garnet crystals can also operate in the same infrared region. These lasers can be pumped either with flashlamps or in a few cases by the second harmonic of a Nd:YAG source. From an overall system viewpoint, second harmonic pumping should be considered because it is more efficient, and uses the modular approach of the semiconductor laser pump source.

Tunable solid-state laser systems configured with an "all solid-state laser" as the basic optical pump source and used to pump a variety of solid-state tunable crystals could provide multiple wavelengths covering a wide range of the electromagnetic spectrum and, in particular, the wavelength ranges needed by LASA experiments. This modular configuration has the potential to provide, either simultaneously or sequentially, a large number of

wavelengths to execute DIAL experiments from space.

Wavelength shifting of fixed-frequency laser emission also represents a technique to obtain tunable laser radiation. There are technologies for achieving wavelength shifting with reasonable efficiency. These include primary Raman shifting in gases and nonlinear crystals. Raman shifters can produce a number of output wavelengths, which are tuned from the input frequency by a multiple of the characteristic Raman shift of the converter material. Output frequencies can be lower (Stokes) or higher (anti-Stokes) than the input frequency, and efficiencies to the first or second Stokes lines can be quite high (10 to 40 percent). The most frequently used Raman shifters are H_2, D_2, and CH_4. Liquids and solids also exhibit useful Raman shifts but are subject to optical damage, and have seen limited applications.

Nonlinear crystals are also used for frequency doubling and tripling and sum and difference frequency generation. Most commonly used materials are KDP with deuterated and nondeuterated analogs (KD*P, KDA, KD*A, CDA, CD*A, ADP, AD*P, ADA, etc.). Others, including lithium niobate and potassium pentaborate have also found application. Frequency summing at high conversion efficiencies has also been observed, but is dependent on input pump power and optical beam quality. The phase-matching condition within the crystal requires that the propagation velocities of the three wavelengths maintain phase as they propagate through the crystal. The conditions for phase matching can be controlled by temperature, pressure, and orientation of the crystallographic axis.

An alternative approach for tunable laser sources that should also be further explored is the optical parametric oscillator (OPO). The parametric oscillator offers the potential advantages of high efficiency, excellent frequency control, wide tuning range, and high-gain amplification to high power levels. Research is underway to demonstrate improved parametric oscillator performance using the recently developed $MgO:LiNbO_3$ crystal.

Optical parametric oscillators are solid-state energy conversion devices that convert a photon at a given frequency to an output of two photons whose sum frequency equals the input frequency. Conversion efficiency depends on input energy and input bandwidths; to date, optical conversion efficiencies as high as 40 percent have been observed. Early experiments using lithium niobate were hampered by material damage problems, but newer crystals, including MnF-doped lithium niobate and urea, may yield satisfactory devices. Operation at the joule-per-pulse level at 5 Hz has not yet been demonstrated.

The development of AlGaAs laser diode arrays as pump sources for Nd:YAG and Nd:glass in a rod or slab configuration has progressed at a rapid rate over the past several years. At 0.532 μm, this laser system is attractive as a pump source for some of the tunable vibronic lasers. In particular, $Ti:Al_2O_3$ pumped by either a Nd:YAG or Nd:glass laser, which are in turn pumped by semiconductor diode arrays, appears to be an attractive "all solid-state" tunable laser system that incorporates many of the system performance characteristics necessary for spaceborne missions, particularly in efficiency and lifetime. (Wallplug efficiencies in Nd:YAG up to 10 percent at 1.06 μm have been projected.) Currently, there is an effort to increase the power of the $Ti:Al_2O_3$ laser at wavelengths needed for Eos LASA experiments to the order of 1 J/pulse at a 10 Hz repetition rate. Based on the rapid progress in the development of laser semiconductors, and with cognizance of historical 5-year development cycles, the economic use of semiconductor pump sources is projected to be available by the early 1990s.

Gas Discharge Lasers

Gas discharge lasers consist of carbon dioxide lasers and excimer lasers. Carbon dioxide lasers have the longest heritage of the gas discharge lasers. They operate on a number of fixed wavelengths in the 10.6 μm region in both pulsed and continuous modes. Output pulse energies in the multiple joule range have been achieved at wallplug efficiencies in excess of 5 percent. High energy and high average power carbon dioxide lasers are in wide use in industry for cutting, welding, drilling, engraving, etc. Extended lifetime (operation to 10^8 shots) has not been demonstrated. However, recent advances in catalytic conversion for room temperature materials hold promise for extended operation with a closed cycle system.

Figure 78 is a block diagram of a pulsed gas discharge laser system. It consists of a power source, a converter of power to high voltage, a primary capacitive energy storage device, and a high voltage, fast switch. Before the discharge is initiated, a separate source of preionization is used to provide a low level of conductivity to the laser gas to ensure a uniform glow discharge. Because the laser is a very inefficient energy converter, a means to remove the excess heat from the gas mixture is necessary as well as a means to circulate the gas mixture in order that each discharge occurs in a gas volume whose temperature and density are homogeneous. A gas cleanup system is required for high-power gas lasers to remove impurities and to regenerate any molecular component that may be chemically altered during the discharge. Finally, optical and electro-optical elements are needed to provide for lasing, frequency and bandwidth control, and beam routing. A particular advantage of gas lasers is that the gain medium has a high degree of fault tolerance compared to a solid-state gain medium, and excess heat is easily removed from a recirculating gas. However,

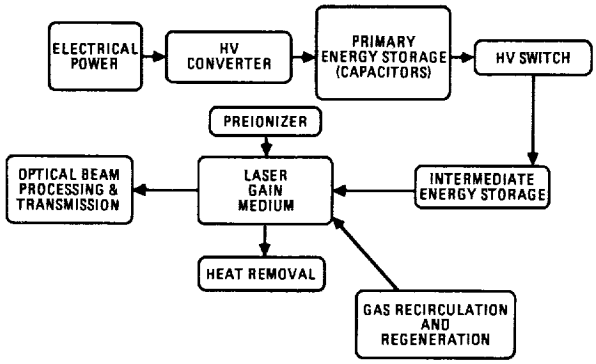

Figure 78. Pulsed gas discharge laser system components.

all of these items must be considered in the overall energy and reliability budget of a laser system.

Table 34 shows the number of accumulated shots versus time on all the electrical components and the gas mixture of the laser at various repetition rates. When data in Table 34 are compared to lifetimes of the laser components as a function of the number of shots contained in Table 35, it is apparent that high pulse energy, low repetition rate operation is necessary for a free-flying spaceborne lidar to meet the needs of adequate SNR and laser lifetime. Pulsed gas discharge laser electrical components can be operated reliably to the 10^8 to 10^9 shot region, if the components are carefully chosen and operated at derated voltage levels. Additionally, all high-voltage circuits should be immersed in oil or a high-pressure electronegative gas. Finally, incorporation of magnetic switches is necessary to achieve long operational life. Although the magnetic switch concept was originally developed for excimer lasers, its use can improve the performance of any high-voltage pulsed power circuit such as is required for carbon dioxide lasers.

Figure 79 shows the various means commonly used to preionize a gas discharge laser. For long-lived space operation, only X-ray preionization or radioactive isotopes are suitable. Further development of the X-ray sources is necessary for long unattended operation of a discharge gas laser from space. Figure 80 is a functional diagram of a tunable injection-locked gas discharge laser system. Other important lifetime issues for LASA lasers include: (1) damage of optical coatings from the high energy densities of the laser beam, (2) aging of the optical coatings leading to loss in reflectivity and in overall laser output efficiency, (3) reduction in the laser window transmission due to impurities formed in the discharge and deposited on the windows, and (4) degradation of the laser gain medium due to the production of impurities and the chemical transformation of the laser gas mixture.

Excimer Laser Technology

Excimer lasers are the newest of the gas discharge lasers, and operate with mixtures of noble gases and halogens; output wavelengths are dependent on the choice of halogen gas (e.g., ArF: 0.193 μm, KrF: 0.248 μm, XeCl: 0.308 μm). Energies in excess of 1 J/pulse and lifetimes in excess of 10^8 shots have been achieved, although a gas scrubbing system is required to inhibit impurity formation in the discharge to allow for space applications. Each excimer laser is directly tunable over a narrow bandwidth (1 to 2 nm), and efficient frequency conversion with Raman shifting in gases has been reported. Wallplug efficiencies are in excess of 2 percent.

Performance Characteristics of Excimer Lasers – The rare-gas halide excimer lasers have undergone considerable development in the last 9 years because they are the only lasers that provide high pulse energy and high average power output in the ultraviolet wavelength region. All the excimer lasers except XeF have continuous emission spectra that indicate an output tuning range of about 10 to 20 Å. Indeed, tunable, high-energy, narrow spectral output has been demonstrated for ArF, KrF, and XeCl in oscillator/amplifier systems.

Pulsewidth, Energy, and Efficiency – The XeCl laser at 4 percent has the highest demonstrated efficiency of any discharge excimer laser. To achieve this efficiency, a double discharge circuit is used. Standard discharge circuits typically produce 1 to 2 percent efficiency. The overall wallplug efficiency for a double discharge XeCl laser at high pulse energy and high average power in an oscillator/amplifier configuration can be engineered to be >1 percent with all ancillary equipment power included. The output pulsewidth of an excimer laser

Table 34. The Number of Accumulated Laser Shots on Components for a Continuously Operating Pulsed Laser System

	1 Hour	1 Day	1 Week	1 Month	1 Year	2 Years
10 Hz	3.6×10^4	8.6×10^5	6.1×10^6	2.4×10^7	2.9×10^8	5.8×10^8
100 Hz	3.6×10^5	8.6×10^6	6.1×10^7	2.4×10^8	2.9×10^9	5.8×10^9
1,000 Hz	3.6×10^6	8.6×10^7	6.1×10^8	2.4×10^9	2.9×10^{10}	5.8×10^{10}
10,000 Hz	3.6×10^7	8.6×10^8	6.1×10^9	2.4×10^{10}	2.9×10^{11}	5.8×10^{11}

Table 35. Pulsed Gas Discharge Laser Component Lifetime Issues

Components	Lifetime
HV Capacitors	10^9 shots – depends on the total charge stored, current density, voltage reversal, inductance, rep-rate, capacitor construction, etc.
HV Switches:	
Spark Gaps	10^5 to 10^7 shots – depends on charge switched, current density, rep-rate, etc.
Thyratrons	10^6 to 10^{10} shots – depends on di/dt, average current, type of tube, etc.
Solid State	Unlimited lifetime, but have low voltage and very slow current and voltage risetimes for most laser applications – used in the switched-mode power supply
Magnetic	Unlimited lifetime, but a primary switch is required
Flashlamps	10^5 to 10^7 shots – depends on charge, current density, rep-rate, etc.
Electrodes	10^8 shots – depends on gas mixture, discharge circuit, materials and preionization
Gain Media	10^5 to 10^8 shots – depends on gas mixture, laser construction, catalysts, gas recirculation and clean-up, fault tolerance, etc.

can be varied from less than a nanosecond to several hundred nanoseconds. However, for reliable and efficient operation of an excimer laser lidar system, a pulsewidth of 50 to 100 ns is normal.

Spectral Bandwidth and Beam Divergence – For an untuned excimer laser, the bandwidth is about 1 Å, and the divergence, which depends on the optical pulse duration, varies between 0.1 and 5 mrad. Control of these parameters, as well as wavelength, is achieved by using an oscillator/amplifier system. For example, injection-locked excimer laser systems have produced 1 J pulses with a spectral bandwidth of <0.01 Å with beam divergence of 100 mrad. The XeCl laser has also been operated on a single longitudinal mode with a bandwidth of 10^{-2} pm. Additionally, the excimer lasers can be continuously tuned with narrow spectral output over 10 to 20 Å ranges.

Repetition Rate and Gas Lifetime – Pulse repetition rates of 3 to 5 Hz are possible in a static gas system. Using laser gas recirculation and thermal heat exchangers, repetition rates up to the kilohertz range have been achieved without degradation of the pulse energy, of the laser efficiency, or of the beam quality, as long as the appropriate engineering criteria were adhered to. Maintenance-free operation of an XeCl laser at 1 J/pulse at a repetition rate of 100 Hz for 10^8 shots has been reported in a Defense Advanced Research Projects Agency (DARPA) study. Both the static and operational gas stability for an XeCl laser mixture are capable of lifetimes in excess of 10^8 shots if proper design features are maintained. However, the static and operational gas lifetimes for the excimer lasers containing fluorine are not as good, and presently require unacceptably large gas cleanup systems for long-term operation. Currently, for a space-based lidar, the XeCl laser is the most appropriate of the excimer lasers from an efficiency and lifetime point of view. In addition, some of the proposed lidar missions for LASA have the potential to be accomplished with the energies and wavelengths derivable from a tuned XeCl laser with frequency shifting. The fundamental wavelength of the XeCl laser is 308 nm.

Frequency Shifting – The high output power and high efficiency of excimer lasers allow the use of frequency shifting techniques to obtain an output in the visible part of the spectrum. The simplest of these techniques is stimulated Raman scattering. Because the wavelength shift is fixed in Raman scattering, tuning of the excimer laser also tunes the frequency shifted output. Table 36 lists the various wavelengths obtained from excimer lasers with several Raman-shifting gases. Multiple Stokes and anti-Stokes shifts are obtained from nonresonant stimulated Raman scattering. Conversion efficiencies to only the first Stokes shift can be as high as 60 percent. With a Raman oscillator/amplifier configuration that converts to the second and third Stokes shift, conversion efficiencies can be as high as 30

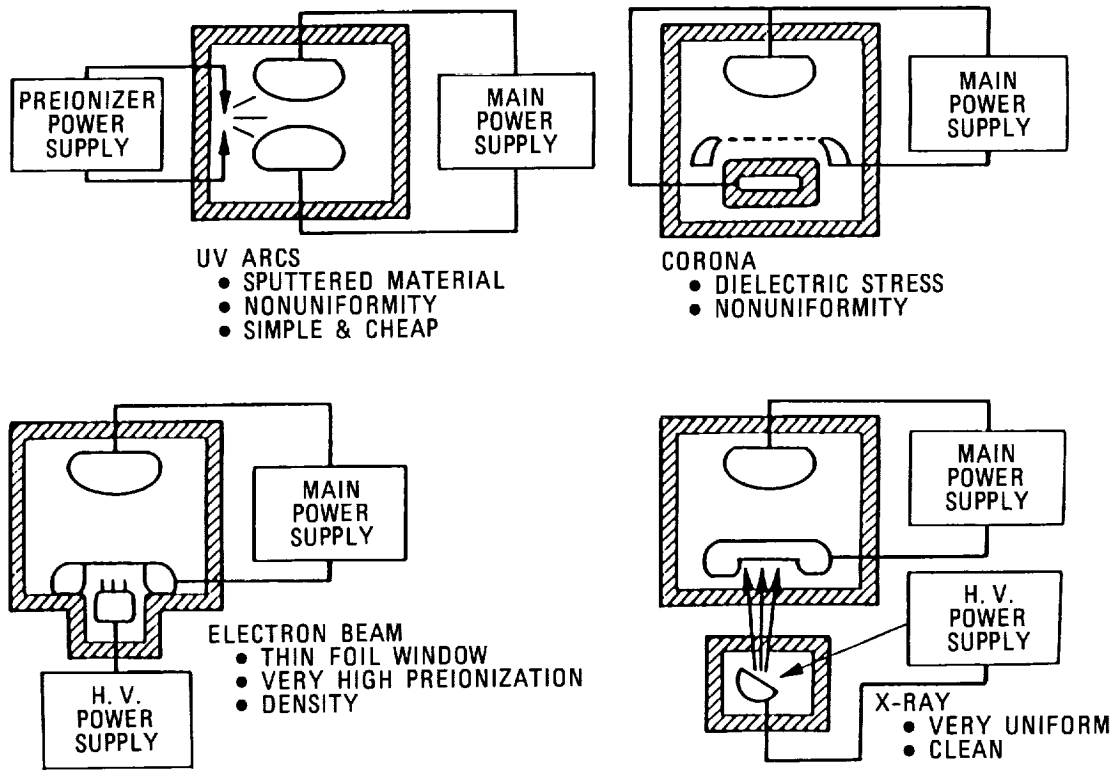

Figure 79. Preionization means.

percent. Since a gas Raman cell is a passive device (only beam optics and a gas cell are needed, no power is required) and in principle fault tolerant, it should be both a reliable and efficient method to generate a multiwavelength lidar for measuring atmospheric parameters. Other wavelength shifting methods include sum or frequency mixing with other sources, stimulated Brillouin scattering, and optical parametric oscillation. In particular, a urea OPO crystal would provide continuous shifting and tuning of the XeCl laser from 0.50 to 1.20 μm, with efficiency near 20 percent. However, it remains to be determined if suitable crystal material can be obtained to achieve this conversion at the joule-per-pulse energy level.

Continuous Wave Low-Pressure Carbon Dioxide Lasers

Continuous wave low-pressure carbon dioxide lasers can be used for DIAL measurements of water vapor. A significant effort in long-lifetime studies of sealed cw low-pressure carbon dioxide lasers has been reported (Willetts and Harris, 1985). Radio frequency-excited (RF), two-to-three watt sealed, 120 torr carbon dioxide waveguide lasers have been operated for $>10^4$ hours (Javan, 1980; Hochuli, 1984) as shown in Figure 81. The initial power reduction to steady-state is comparatively small, but after 4×10^3 hours, a drop to 70 percent power occurs. The RF excitation was produced with one internal electrode (Pt/Cu) and an external capacitively coupled Au/In electrode (Figure 82). Demonstration of a direct current-excited (DC) sealed carbon dioxide waveguide laser with 4.2×10^4 hour operation at 80 percent initial power (Figure 83) was described by Hochuli (1981). In this laser, special precautions were taken to shield the laser mirrors from sputtering. However, in RF-excited lasers the sputtering should be much less severe. A compact waveguide laser with external RF excitation using axially displaced steel or Pt electrodes is being developed (Figure 84). Lasers with this design have operated for >20,000 hours at power outputs sufficient for local oscillator or injection oscillator applications. A large number of cw sealed carbon dioxide lasers are available under commercial or contractor development. Some of these lasers demonstrate long lifetime (including shelf life), however, with considerable reduction in steady-state power. This may be acceptable for some applications, but not for LASA.

LASER TECHNOLOGY ASSESSMENT FOR SURFACE-RANGING MEASUREMENTS

The technology for LASA experiments that require nontunable laser energy is currently available. Nd:YAG is the most advanced of all solid-state laser

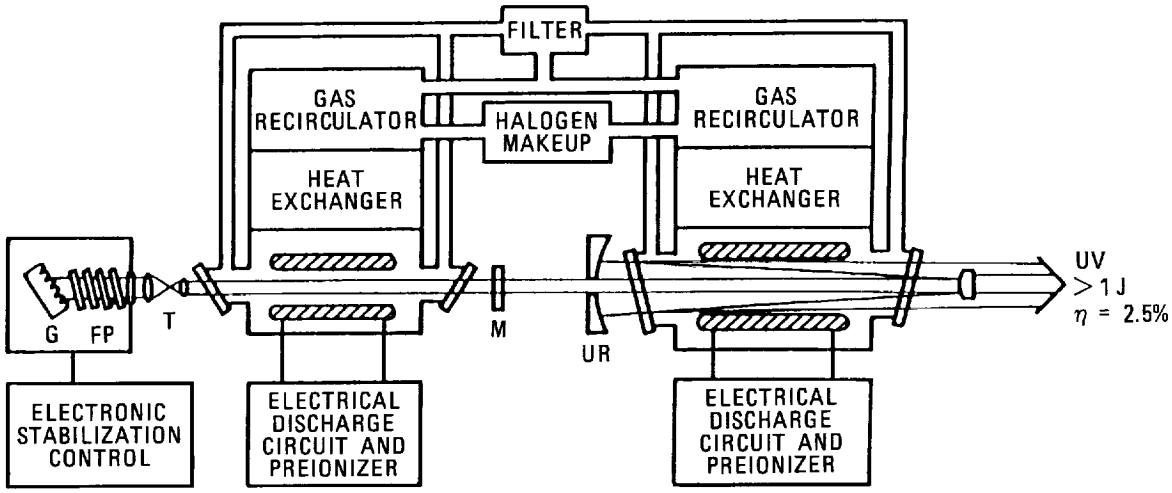

Figure 80. Functional diagram of a tunable injection-locked gas laser system.

materials, and is capable of running either in a pulsed or continuous mode. The capabilities of Nd:YAG have been discussed extensively in the previous section. Energy outputs in the range of 1 J/pulse at 1.06 μm are routinely achieved in laboratory systems. Frequency doubling to 0.532 μm has been accomplished with efficiencies greater than 50 percent, and 35 percent efficiencies are routinely obtained. This material also lases near 1.3 μm, although at lower output energies. Overall wallplug efficiency for pulsed systems at 1.06 μm is about 0.5 percent to 2 percent when pumped by flashlamps. High-quality material is available from a variety of commercial sources.

Nd:glass is also a well-advanced solid-state laser technology. Glass configured as a laser rod cannot handle the energy density that the YAG crystal can. However, a new slab configuration has yielded glass lasers of much higher power and repetition rates than YAG crystals. Neodymium laser emission in glass, as contrasted to the crystal form, is tunable over a narrow range (approximately 5 nm), thus, allowing its use as a source for parametric mixing to obtain wavelength tunability.

Table 36. Wavelengths Obtained from XeCl Excimer Laser Using Raman-Shifting Gases

Raman-Shifting Gas	Stokes-Shift Wavelength (nm)		
	1st	2nd	3rd
H_2	353	414	499
D_2	339	377	426
CH_4	338	375	422
N_2	337	359	392

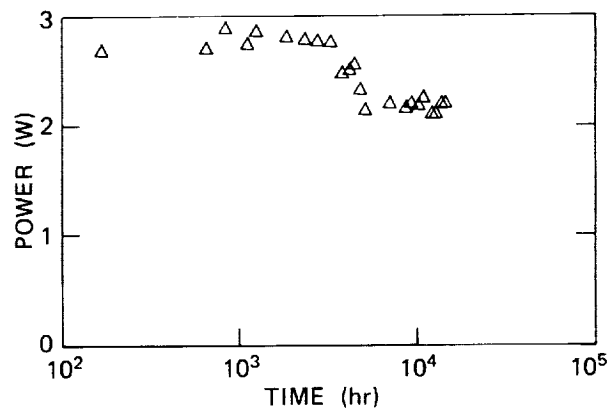

Figure 81. Lifetime study of RF-cw carbon dioxide waveguide lasers.

COMPARISON OF LASA OBJECTIVES WITH LASER CAPABILITIES

As seen from the previous sections, there are several laser sources which may be used to satisfy LASA scientific objectives. Each of these laser sources has attributes and performance characteristics which can apply to more than one of the many different LASA experiments, and, in many cases, can be applied to several scientific objectives. An analysis was conducted as to the applicability of current and future (emerging) laser technology for each LASA objective.

Table 37 shows of the applicability of current laser sources to the various LASA missions. As seen, depending on pulse energy requirements, a large fraction of the objectives can be satisfied with proper engineering of current laser technology. Some of the most stressing engineering issues (listed at the bottom of the table) still need to be

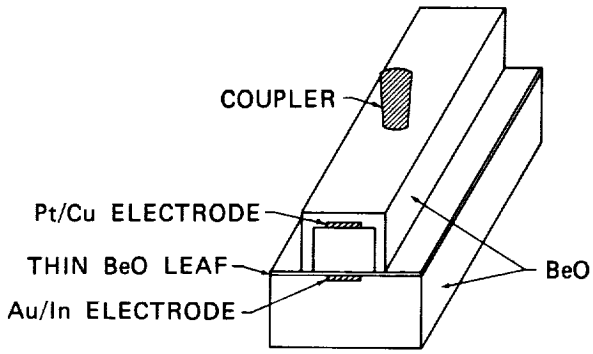

Figure 82. Channel structure of RF-excited carbon dioxide waveguide laser.

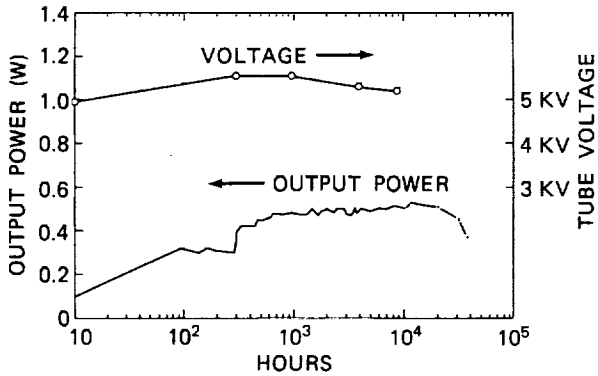

Figure 83. Lifetime study of DC-cw carbon dioxide waveguide laser. Characteristics of the laser: Laser G2A (refill), insulated 2L4.5 Ag 5 Cu cathode, 0.8 mm Pt PIN anode, 5.6 mm × 250 mm bore, 6 ma D.C., 50 cm³, He:CO_2:CO:Xe:H_2, 15:7:7:1.5:0.2; 20 torr (Hochuli, 1981).

addressed, in particular laser lifetime. In this regard, laser lifetime is ultimately limited to less than

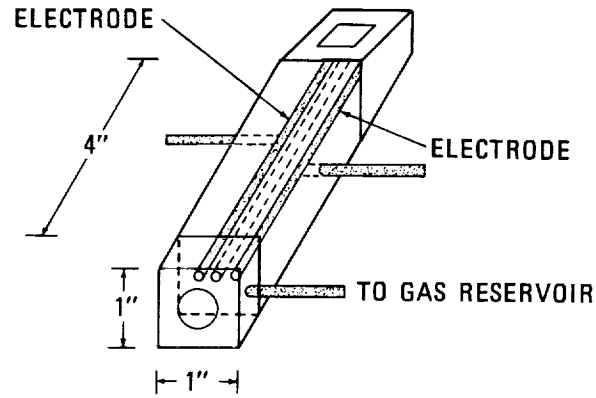

Figure 84. Integrated structure of RF-excited carbon dioxide waveguide laser.

a year by flashlamp technology for continuous operation at 10 Hz. Attainment of long lifetime is also an issue for electrical discharge lasers. The high pulse energy (>1 J/pulse) solid-state laser (Alexandrite) would consume high input power (of the order of 7 kW/laser).

Table 38 shows similar information for emerging laser technology. As seen, several new technologies may offer significant advantages for new laser sources, but issues involving energy conversion efficiency, tunability, and lifetime will still have to be addressed.

In summary, from an overall systems viewpoint, the laser transmitter should operate at the maximum overall efficiency for the longest possible duration. Tunability should be accomplished by efficient nonlinear conversion of the pump laser, followed by the pumping of the tunable source. As seen in Tables 37 and 38, several candidate lasers exist which should be seriously considered in any tradeoff study for a wide range of LASA objectives.

(continued)

Table 37. Comparison of LASA Objectives with Present Laser Technology

LASA Objectives	Present Laser Technology							
	Raman-Shifted Excimer 300 nm		Alexandrite 720 nm to 790 nm		Nd:YAG 1.06 μm & 0.53 μm		Carbon Dioxide Heterodyne 9.2 μm to 10.8 μm	
	Low*	High**	Low	High	Low	High	Low	High
1. Altimetry			X	X	X	X		X
2. Retroranging					X***	X***		
3. Cloud Height	X	X	X	X	X	X		X
4. PBL		X		X		X		X
5. Stratospheric Aerosol		X		X		X		X
6. Cloud Parameters		X		X		X		X
7. Tropospheric Aerosol		X		X		X		X
8. Water Vapor Column			X	X				X****
9. Surface Pressure			X	X				
10. Ozone Column	X	X						
11. Water Vapor Profile				X				
12. Pressure Profile		X†		X				
13. Temperature Profile		X†		X		X		
14. Ozone Profile		X						X****
Laser Issues:	Gas Lifetime‡		Low Efficiency, Crystal Availability		Flashlamp Lifetime		Carbon Dioxide Lifetime§	

*Low energy: ≤100 mJ
**High energy: ≥0.5 J
***Short pulse (<1 ns) Nd:YAG
****cw carbon dioxide (20 W transmitter power)
†Stratosphere
‡Requires gas scrubber
§Gas lifetime may be enhanced by use of catalytic system

Table 38. Comparison of LASA Objectives with Emerging Laser Technology

LASA Objectives	Emerging Laser Technology									
	$Ti:Al_2O_3$ 700 nm to 900 nm		Diode-Pumped Nd:YAG		OPO-Shifted Excimer		OPO-Shifted Solid-State Laser		Extended Lifetime Dye	
	Low*	High**	Low	High	Low	High	Low	High	Low	High
1. Altimetry	X	X	X	X			X	X	X	X
2. Retroranging			X***	X***						
3. Cloud Height	X	X	X	X		X	X	X	X	X
4. PBL		X		X		X		X		X
5. Stratospheric Aerosol		X		X		X		X		X
6. Cloud Parameters		X		X		X		X		X
7. Tropospheric Aerosol		X		X		X		X		X
8. Water Vapor Column	X	X					X	X	X	X
9. Surface Pressure	X	X					X	X	X	X
10. Ozone Column					X	X	X	X		
11. Water Vapor Profile		X				X		X		X
12. Pressure Profile		X				X		X		X
13. Temperature Profile		X				X		X		X
14. Ozone Profile						X		X		
Laser Issues:	Nd:YAG (2 X) Pumped, Power		Power, Diode Arrays Not Demonstrated		High-Efficiency Tunability		High Power		Spaceborne Liquid Difficulties	

*Low energy: ≤100 mJ
**High energy: ≥0.5 J
***Short pulse

VI. Eos COMMAND AND DATA MANAGEMENT SYSTEMS FOR LASA

This section deals with the command and data management systems required to support LASA and GLRS operation within the Eos mission. The baseline lidar system configuration includes capabilities for making measurements of stratospheric and tropospheric aerosols, cloud measurements, and selected DIAL features as described earlier in this document. For altimetry and ranging measurements, the same LASA laser transmitter and receiver instrument components will be used in the altimetry mode. Primary emphasis in altimetry is on time-of-flight measurements of the laser pulse and precise knowledge of laser pointing angles with respect to instrument nadir and precise knowledge of spacecraft orbital position. A suitable lidar might include one fixed-frequency laser with fundamental, second, and third harmonic outputs, and one or two tunable lasers for making the on-line and off-line DIAL measurements. The altimeter mode of operation would employ only one of these lasers, but would require additional data sets on laser beam pointing angle and spacecraft position. The GLRS instrument for geodynamic ranging is separate from the LASA instrument, but will have similar data management requirements to the LASA altimeter.

No assumptions have been made about the character of the onboard control and data management services that will be provided by the Eos platform to its resident instruments. Therefore, this analysis presents a worst-case approach to defining the data and control system requirements for the LASA systems.

DATA RATES

The estimated bit rate for science data generated by the system is based on the following assumptions:

- The highest estimated bit rate for science data generated by the system is desirable. Therefore, a five-channel receiver is indicated as well as a five-channel digitizer.
- The DIAL measurement capability requirement dictates an equivalent 12 or more bit dynamic range. While current technology (1985) makes 12 bits the practical limit, advances in high-speed analog-to-digital converter technology by the late 1980s could make converters with resolution in excess of 12 bits technically feasible. The altimetry mode of operation requires a digital timer with at least 26-bit time resolution, but a very low data rate – one digital timer word supplemented by waveform digitization over a short time interval centered on the surface return pulse. Total data rate requirement for altimetry is less than 500 kbit/sec including pointing angle, GPS, and housekeeping data.
- The altitude range of interest for Eos lidar systems extends from approximately 50 km down to the ground. This translates to a data-gathering period of about 400 ms.
- The minimum desired range-bin resolution is 15 m for all lidar (non-altimetric) measurements. This translates to a digitizer sampling rate of 10 million samples per second.
- The laser pulse repetition rate is 10 pulses/sec for all atmospheric studies and 20 pulses/sec for altimetry mode operation (surface topography studies). The altimetry pulse rate is twice that of the lidar, but it will occur only in a burst mode for a small percentage of each orbit. Even at 20 Hz, the altimetry data rate is less than that for lidar because no high data rate digitization is required. Based on these assumptions, the average data bit rate of the lidar system is given by the equation: Bit Rate $= B\ R\ T_{data}\ N\ S$ where B = number of bits per word (12), R = digitizer sampling rate (1×10^7 sec^{-1}), T_{data} = data period (4×10^{-4} sec), N = number of receiver channels (5), and S = number of laser shots/sec (10).

For the values shown, the bit rate is approximately 2.4 Mb/sec. Data compression schemes could be implemented that could decrease the volume of redundant data generated by the lidar systems and thereby reduce the downlink data rate by orders of magnitiude. A good example is the 1×300 km resolution required for stratospheric aerosol measurements.

COMMAND UPLINKING AND CONTROL

Considerable study should be given to the design of the onboard computer that will control the lidar system on Eos. Suitable onboard data evaluation strategies can minimize the uplink command and control activity. In addition, the system should have onboard capability to evaluate system performance and modify system operating parameters to compensate for long-term shifts in component characteristics (i.e., an adaptive system is called for).

The system should have a default or "safe-state" mode in which it operates in the absence of any

uplink command or after a platform power interruption. Other options might include the capability to command a particular mode in real time or to load sets of modes to be executed at particular times or at particular geophysical locations in orbit. A system to satisfy the above requirements would include five digitizer channels in addition to the onboard control computer.

SYSTEM REDUNDANCY

In view of the 2-year period between revisits to the platforms for maintenance and repair, some degree of redundancy in the system would be prudent. For redundancy, three additional digitizer channels are recommended. A detector output switching matrix with cross-strap redundancy would allow the connection of any receiver channel to any digitizer channel. And finally, a backup control computer would be desirable.

GROUND COMPUTER FACILITIES

A ground computer system will be required to process, display, and store the data received from LASA, and to generate and format commands to be transmitted to LASA. Preliminary analysis capability should be included so that the quality of the incoming data can be evaluated as it is received. In addition to the backscattered and background data stored onboard during the previous orbit, the downlinked data will include real-time status and housekeeping information, which must be formatted and displayed. The ground command data set will include all routine operating command sequences and special commands for trouble-shooting and calibration procedures.

VII. CONCLUSIONS AND RECOMMENDATIONS

Lidar and cw laser systems, operating in the single wavelength or tunable mode can make unique contributions to the overall capabilities of Eos. These contributions will be in the areas of atmospheric composition and structure measurements and a set of surface-ranging measurements. Operation in the ultraviolet, visible, and infrared regions of the electromagnetic spectrum makes several unique measurement features available.

- The transmitter wavelengths are comparable to the sizes of atmospheric aerosols and cloud droplets, thereby providing the means to obtain information on aerosol profiles, cloud-top heights, PBL heights, and the geometric thickness and optical depths of thin clouds.
- The high level of monochromaticity of lidar can be used to uniquely identify molecular species and measure their concentrations against interfering background spectra. With tunable laser sources, water vapor and ozone can be measured through the DIAL technique with high vertical resolution.
- Monochromaticity and tunability of lidar, especially in the absorption bands of uniformly mixed gases such as O_2 and CO_2, make possible the direct measurement of atmospheric temperature and pressure with high vertical resolution.
- Heights of ground surfaces can be measured with unprecedented resolution and accuracy. Laser altimetry with height resolution better than 10 cm is achievable. Ice and terrain roughness measurements at centimeter levels offer higher accuracy than any other technique.
- Centimeter-level crustal movements can be detected through retroranging for improved understanding of earthquakes and tectonic plate motions. High-precision geodetic control networks can be established on a regional and global basis.
- Lidar is an active probing tool allowing for direct recovery of the measurement variable without requiring inversion techniques, thus reducing overall uncertainties. Active probing with lidar also allows height resolution of variables from the Earth's surface upward. When range information is not essential, cw lasers offer a considerable advantage over current pulsed systems in that their expected lifetimes are considerably longer.

In this report, the experiments have been divided into two basic categories, which reflect the degree of instrument readiness. Experiments requiring only currently available and demonstrated technology include:

- Precision altimetry and retroranging (GLRS)
- Water vapor column content
- Cloud-top heights
- PBL heights
- Optical depths of thin clouds

The above measurements are, in principle, candidates for early implementation on Eos (IOC).

Experiments that have not yet been performed from aircraft and/or that require additional technology development are:

- aerosol profiling and total aerosol optical thickness,
- tropospheric and stratospheric water vapor profiles,
- surface pressure and vertical profiles of temperature and pressure, and
- ozone total column amount and vertical profiles.

Some of the above experiments may be performed from aircraft platforms prior to final selection of an initial LASA configuration.

An integral strategy of Eos is to strive for technological advances in critical areas so that the measurement basis may be expanded. Toward this end, the LASA Panel Committee recommends:

- System-level studies should be initiated early in Eos to address the question of trade-offs among the following criteria: high wallplug efficiency, fault tolerance, long lifetime, and ability to operate at high pulse energies in a narrow spectral band.
- Continuous technological development of lidar subsystems, including detectors, flashlamps, laser diode pumping arrays, lightweight telescopes, and laser wavemeter-spectrometers as calibration instruments.
- An interdisciplinary solid-state material's research program is needed to shorten the lead time in laser transmitter development.
- Development of efficient harmonic conversion techniques for nonlinear crystals.
- Development of X-ray sources for pre-ionization to achieve long, unattended operation of discharge gas lasers from space.
- Continued and more detailed simulation studies, verified through aircraft and/or Shuttle and possibly space station experiments, as a natural progression from concept to Eos application.

- Implementation of methods allowing for LASA scanning capabilities on future Eos investigations.

The LASA experiments open up an exciting new opportunity to measure geophysical parameters with vertical and horizontal resolutions never before obtainable on a global scale. The resulting data will enable scientists to understand the Earth's atmosphere and surface processes at a level previously unattainable.

C-2

APPENDIX A

EYE SAFETY ISSUE

The laser eye safety issue is characterized by the transmitted laser pulse energy and intensity, and the footprint illuminated on the ground. Such a consideration is related to the FOV of the LASA telescope since the laser beam is adjusted to be equal to the telescope FOV. Under these circumstances, the appropriate FOV of the telescope is approximately 1 mr. This value may be incorporated with the allowable maximum permitted exposure (MPE) for laser excitation for safe eye exposure as presented in Table A.1 (Sliney and Wolbarscht, 1982) and tabulated in Table A.2.

As can be seen in Table A.3, lasers with energies of 1 J/pulse are eye safe from Eos altitudes for all spectral wavelengths for the unaided eye. It should be noted, however, that higher safety factors may be appropriate for viewing by the optically aided eye (binoculars or telescope), and where scintillation aperture averaging is considered. While little experimental data exists for these latter considerations, further work will be required for LASA and other downlooking laser-based systems.

Table A.1. Laser Energy, Field-of-View, and Eye Safety

Wavelength	Maximum Permitted Exposures (J cm^2)
300 to 400 nm	$0.56\ t^{0.25}$ [t = pulse length (sec)]
400 to 700 nm	5×10^{-7}
700 to 1,050 nm	$5 \times 10^{-7} \times 10^{[0.002(\lambda - 700)]}$
1,050 nm	5×10^{-6}

Allowable Energy = MPE × Area of Footprint/Safety Factor

Area of Laser Footprint on Ground = (FOV × Orbit Height)^2 × $\pi/4$

Data on MPE and the formulas used to calculate the maximum allowable laser energy per pulse from an orbital Eos altitude of 700 km (Sliney and Wolbarscht, 1982).

Table A.2. American National Standards Institute Maximum Permissible Energy for Differing Fields-of-View (Unaided Eye)

Wavelength Range	300 to 400 nm, 1.4 μm to 10 μm	400 to 700 nm	760 nm	1,060 nm
ANSI MPE (J/cm^2)	1.0×10^{-3}	5.0×10^{-7}	6.59×10^{-7}	5.0×10^{-6}

Table A.3. Maximum Permissible Laser Pulse Energy for Differing Fields-of-View

FOV (mr)	Ground Footprint (cm^2) from 700 km Orbit	Maximum Permissible Laser Pulse Energy (J)			
0.05	9.6×10^6	9.6×10^3	4.8	5.3	48.1
0.10	3.8×10^7	3.8×10^4	19.2	25.4	192.0
0.20	1.5×10^8	1.5×10^5	77.0	101.0	770.0
0.50	9.6×10^8	9.6×10^5	481.0	634.0	4,810.0
1.00	3.8×10^9	3.8×10^6	1,920.0	2,540.0	1.9×10^4
2.00	1.5×10^{10}	1.5×10^7	7,700.0	1.0×10^4	7.7×10^4
5.00	9.6×10^{10}	9.6×10^7	4.8×10^4	6.3×10^4	4.8×10^5
10.00	3.8×10^{11}	3.8×10^8	1.9×10^5	2.5×10^5	1.9×10^6

The maximum permissible laser pulse energy from a 700 km orbit based on the American National Standards Institute (ANSI) MPE levels (as shown in Table A.2) for wavelengths from the ultraviolet to the near infrared. These maximum permissible laser pulse energies are given for various FOVs and are for the unaided eye with no safety factors included. Attenuation losses of the laser beam as it propagates through the atmosphere are not included.

REFERENCES

Abshire, J.B., A comparative study of optimum and sub-optimum direct-detection laser-ranging receivers, *NASA TP 1315*, GSFC, Greenbelt, MD, September 1978.

Abshire, J.B., and J.E. Kalshoven, Jr., Multicolor laser altimeter for barometric measurements over the ocean: Experimental, *Appl. Opt., 22*, 2578, 1983.

Abshire, J.B., J.F. McGarry, R.S. Chabot, and H.E. Rowe, Airborne measurements of atmospheric pressure with a two-color streak camera-based laser altimeter, *Paper PD6*, Conference on Lasers and Electro-Optics, Baltimore, MD, May 21-24, 1985.

Abshire, J.B., and C.S. Gardner, Atmospheric refractivity corrections in satellite laser ranging, *IEEE Trans. Geosci. Remote Sens., RE-23*, 414, 1985.

Alley, C.O., Proper time experiments in gravitational fields with atomic clocks, aircraft, and laser light pulses, in *Quantum Optics, Experimental Gravity, and Measurement Theory*, edited by P. Meystre and M.O. Scully, p. 363, Plenum Publishing Corp., NY, 1983.

Bandeen, W.R., and R.S. Fraser, (Eds.), Radiative effects of the El Chichon volcanic eruption: Preliminary results concerning remote sensing, *NASA TM 84959*, 1982.

Brooks, R.L., W.J. Campbell, R.O. Ramseier, H.R. Stanley, and H.J. Zwally, Ice-sheet topography by satellite altimetry, *Nature, 274*, 539, 1978.

Browell, E.V., A.F. Carter, S.T Shipley, R.J. Allen, C.F. Butler, M.N. Mayo, J.H. Siviter, Jr., and W.M. Hall, NASA multipurpose airborne DIAL system and measurements of ozone and aerosol profiles, *Appl. Opt., 22*, 522, 1983.

Browell, E.V., A.K. Goroch, T.D. Wilkerson, and S. Ismail, Airborne DIAL water vapor and aerosol measurements over the Gulf Stream wall (abstract), *12th International Laser Radar Conference*, p. 151, Aix en Provence, France, August 13-17, 1984.

Browell, E.V., S.T. Shipley, C.F. Butler, and S. Ismail, Airborne lidar measurements of aerosols, mixed layer heights and ozone during the 1980 PEPE/NEROS summer field experiment, *NASA RP 1143*, 1985.

Browell, E.V., E.F. Danielsen, S. Ismail, G.L. Gregory, and S.M. Beck, Tropopause fold characteristics determined from airborne lidar and *in situ* measurements, Submitted to *J. Geophys. Res.*, 1986.

Bufton, J.L., J.E. Robinson, M.D. Femiano, and F.S. Flatow, Satellite laser altimeter for measurement of ice-sheet topography, *IEEE J. Trans. Geosci. Remote Sens., GE-20*, 544, 1982.

Bufton, J.L., F.E. Hoge, and R.N. Swift, Airborne measurements of laser backscatter from the ocean surface, *Appl. Opt., 22*, 2603, 1983.

Butler, D.M., *et al.*, Earth Observing System: Science and Mission Requirements Working Group Report, *NASA TM 86129*, 1984.

Cato, G.A., L.W. Carrier, and K.J. von Essen, The backscattering and extinction of visible and infrared radiation by selected major cloud models, *Appl. Opt.*, 6, 1209, 1967.

Cohen, S.C., and G.R. Cook, Determining crustal strain rates with spaceborne geodynamics ranging system data, *Manuscripta Geodaetica, 4*, 245, 1979.

Cohen, S.C., and D.E. Smith, LAGEOS scientific results: Introduction, *Geophys. Res., 20,* 9217, 1985.

Degnan, J.J., An overview of NASA airborne and spaceborne laser-ranging development, in *Proceedings of the Fifth International Workshop on Laser-Ranging Instrumentation*, Royal Greenwich Observatory, East Sussex, England, September 10-14, 1984.

Degnan, J.J., Satellite laser ranging: Current status and future prospects, *IEEE Trans. Geosci. Remote Sens., GE-23*, 398, 1985.

Elterman, L., Ultraviolet, visible and infrared attenuation for altitudes to 50 km, 57 pp., *AFCRL-68-0153*, AFCRL, Hanscomb AFB, MA, 1968.

Englisch, W., W. Wiesemann, J. Boscher, and M. Rother, Laser remote sensing measurements of atmospheric species and natural target reflectivities, in *Optical Laser Remote Sensing*, edited by D.K. Killinger and A. Mooridian, p. 38, Springer-Verlag, Berlin, 1983.

Gardner, C.S., B.M. Tsai, and K.E. Im, Multicolor laser altimeter for barometric measurements over the ocean: Experimental, *Appl. Opt., 22*, 2578, 1983.

Griffiths, H., Special difficulties of retrieving surface elevation over continental ice, in *Proceedings of Workshop on ERS-1 Radar Altimeter Data Products*, p. 61, Report ESA SP-221, European Space Agency, August 1981.

Hamill, P., and L.R. McMaster, Polar stratospheric clouds: Their role in atmospheric processes, *NASA Conference Publication 2318*, NASA, Washington, D.C., 1984.

Hochuli, U., Continued life test results for an ensemble of CO_2 lasers: Final report, *NASA Grant NSG-5042*, p. 3, Electrical Engineering Department, University of Maryland, College Park, MD, April 1981.

Hochuli, U., Investigation of RF-excited cw CO_2 waveguide lasers: Progress report, *NASA Grant NAG5-263/Degnan*, GSFC, Greenbelt, MD, April 1984.

Hopfield, H.S., Tropospheric range error at zenith, *Space Research, 12*, p. 581, Akademie-Verlag, Berlin, 1972.

Javan, A., High pressure gas laser technology for atmospheric remote sensing, *NASA Conference Publication 2138*, p. 511, Williamsburg, VA, March 1980.

Kahn, W.D., F.O. vonBun, D.E. Smith, T.S. Englar, and B.P. Gibbs, Performance analysis of the spaceborne laser ranging system, *Bulletin Geodesy, 54*, 165, 1980.

Kalshoven, J.E., Jr., C.L. Korb, G.K. Schwemmer, and M. Dombrowski, Laser remote sensing of atmospheric temperature by observing resonant absorption of oxygen, *Appl. Opt., 20*, 1967, 1981.

Kaula, W.M., G. Schubert, W.L. Lingenfelter, W.L. Sjogien, and W.R. Wollenhaupt, Apollo laser altimetry and inferences as to lunar structure, *Geochim. Cosmochim. Acta, 38*, 3049, 1974.

Kneizys, F.X., E.P. Shettle, W.O. Gallery, J.H. Chetwynd, Jr., L.W. Abreu, J.E.A. Selby, S.A. Clough, and R.W. Fenn, Atmospheric transmittance/radiance: Computer code LOWTRAN 6, *AFGL-TR-83-0187*, 200 pp., AFGL, Hanscom AFB, MA, 1983.

Kolenkiewicz, R., J. Ryan, and M.H. Torrence, A comparison between LAGEOS laser ranging and very long baseline interferometry, *J. Geophys. Res., 90*, 9265, 1985.

Korb, C.L., and C.Y. Weng, Differential absorption lidar technique for measurement of the atmospheric pressure profile, *Appl. Opt., 22*, 3759, 1983.

Korb, C.L., G.K. Schwemmer, M. Dombrowski, J. Milrod, and H. Walden, Airborne lidar measurements of the atmospheric pressure profile with tunable Alexandrite lasers, in *Proceedings of the Thirteenth International Laser Radar Conference*, Toronto, Canada, 1986.

Korb, C.L., and C.Y. Weng, A theoretical study of a two-wavelength lidar technique for the measurement of atmospheric temperature profiles, *J. Appl. Meteor., 21*, 1346, 1982.

Korb, C.L., G.K. Schwemmer, M. Dombrowski, J. Milrod, and H. Walden, Lidar measurements of atmospheric pressure and temperature with tunable Alexandrite lasers, in *Proceedings of the First International DIAL Collection and Analysis Workshop*, p. 46, Virginia, 1985.

Marini, J.W., and C.W. Murray, Correction of laser range tracking data for atmospheric refraction at elevations above 10°, *TR X-591-73-351*, GSFC, Greenbelt, MD, November 1973.

McClatchey, R.A., R.W. Fenn, J.E.A. Selby, J.S. Garing, and F.E. Volz, Optical properties of the atmosphere, *AFCRL-70-0527*, AFCRL, Hanscom AFB, MA, 1970.

McClatchey, R.A., R.W. Fenn, J.E.A. Selby, F.E. Volz, and J.S. Garing, Optical properties of the atmosphere, 113 pp., *AFCRL-72-0497*, AFCRL, Hanscom AFB, MA, 1972.

McCormick, M.P., T.J. Swissler, W.H. Fuller, W.H. Hunt, and M.T. Osborn, Airborne and ground-based lidar measurements of the El Chichon stratospheric aerosol from 90°N to 56°S, *Geofis. Int., 23*, 187, 1984.

McCormick, M.P., H.M. Steel, P. Hamill, W.P. Chu, and T.J. Swissler, Polar stratospheric cloud sightings by SAM II, *J. Atmos. Sci., 39*, 1387, 1982.

Meier, M.F., *et al.*, Glaciers, ice sheets, and sea level; Effects of a carbon dioxide-induced climatic change, *Report of the Workshop held in Seattle, WA*, September 13-15, 1984, Ad Hoc Committee on the Relationship Between Land Ice and Sea Level of the Committee on Glaciology, 330 pp., National Research Council, National Academy Press, Washington, D.C., 1985.

Melfi, S.H., J.D. Spinhirne, S-H. Chou, and S.P. Palm, Lidar observations of vertically organized convection in the planetary boundary layer over the ocean, *J. Clim. Appl. Meteor., 24*, 806, 1985.

Mitchell, J.M., and W.W. Kellogg, The polar regions and climatic change, *Committee on the Role of the Polar Regions in Climatic Change of the Polar Research Board*, National Research Council, National Academy Press, Washington, D.C., 1984.

NASA, The NASA geodynamics program: An overview, *NASA TP 2147*, Geodynamics Program Office, Office of Space Science and Applications, January 1983.

Nelson, R.L., W.B. Krabil, and G.A. Maclean, Determining forest canopy characteristics using airborne laser data, *Remote Sens. Environ., 15*, 201, 1984.

O'Brien, H.H., Red and near-infrared spectral reflectance of snow, *Report No. 332*, U.S. Army Cold Regions Research and Engineering Lab, Hanover, NH, March 1975.

Pal, S.R., and A.I. Carswell, Polarization properties of lidar scattering from clouds at 347 nm and 694 nm, *Appl. Opt., 17*, 2321, 1978.

Platt, C.M.R., and A.C. Dilley, Remote sensing of high clouds–II: Emissivity of cirrostratus, *J. Appl. Meteor., 18*, 1144, 1979.

Platt, C.M.R., and A.C. Dilley, Remote sounding of high clouds–IV: Observed temperature variations in cirrus optical properties, *J. Atmos. Sci., 38*, 1069, 1981.

Plotkin, H.H., T.S. Johnson, P.L. Spadin, and J. Moye, Reflection of ruby laser radiation from Explorer XXII, *IEEE Proc., 53*, 301, 1965.

Polar Research Board, Research emphases for the U.S. Antarctic Program, 52 pp., National Research Council, National Academy Press, Washington, D.C., 1983.

Polar Research Board, Committee on Glaciology, Environment of West Antarctica: Potential carbon dioxide-induced changes, 236 pp., *Report of a Workshop held in Madison, WI,* July 5-7, 1983, National Research Council, National Academy Press, Washington, D.C., 1984a.

Polar Research Board, Committee on the Role of the Polar Regions in Climatic Change, The polar regions and climatic change, 59 pp., National Research Council, National Academy Press, Washington, D.C., 1984b.

Russell, P.B., T.J. Swissler, and M.P. McCormick, Methodology for error analysis and simulation of lidar aerosol measurements, *Appl. Opt., 18*, 3783, 1979.

Russell, P.B., and B.M. Morley, Orbiting lidar simulations II: Density, temperature, aerosol and cloud measurements by a wavelength-combining technique, *Appl. Opt., 21*, 1554, 1982.

Sassen, K., An initial application of polarization lidar for orographic cloud seeding operations, *J. Appl. Meteor., 19*, 298, 1980.

Schwemmer, G.K., Atmospheric pressure profile measured with a differential absorption lidar, in *Proceedings of the 12th International Laser Radar Conference*, p. 157, Aix en Provence, France, August 13-17, 1984.

Shettle, E.P., and R.W. Fenn, Models for the aerosols of the lower atmosphere and the effects of humidity variations on their optical properties, 94 pp., *AFGL-TR-79-0214*, AFGL, Hanscom AFB, MA, 1979.

Shipley, S.T., E.V. Browell, D.S. McDougal, B.L. Orndorff, and P. Haagenson, Airborne lidar observations of long-range transport in the free troposphere, *Environ. Sci. Tech., 18*, 749, 1984.

Sliney, D., and M. Wolbarscht, in *Safety with Lasers and Other Optical Sources*, 1060 pp., Plenum Press, NY, 1982.

Spinhirne, J.D., M.Z. Hansen, and L.O. Caudill, Cloud-top remote sensing by airborne lidar, *Appl. Opt., 21,* 1564, 1982.

Spinhirne, J.D., M.Z. Hansen, and J. Simpson, The structure and phase of cloud tops as observed by polarization lidar, *J. Clim. Appl. Meteor., 22*, 1319, 1983.

Talbot, R.W., R.C. Harriss, E.V. Browell, G.L. Gregory, D.I. Sebacher, and S.M. Beck, Distribution and geochemistry of aerosols in the tropical north Atlantic troposphere: Relation to Saharan dust, *J. Geophys. Res., 91*, 5173, 1986.

Thekaekara, M.P., Extraterrestrial solar spectrum, 3000-6100 at 1-Å intervals, *Appl. Opt., 13*, 518, 1974.

Thomas, R.H., T.V. Martin, and H.J. Zwally, Mapping ice sheet margins from radar-altimetry data, *Ann. Glaciol., 4*, 283, 1983.

Thomas, R.H., T.J.O. Sanderson, and K.E. Rose, Effect of climatic warming on the west Antarctic ice sheet, *Nature, 277*, 355, 1979.

Uchino, O., M. Maeda, and M. Hirona, Applications of excimer lasers to laser radar observations of the upper atmosphere, *IEEE J. Quant. Electron., QE-15*, 1094, 1979.

Werner, J., K.W. Rothe, and H. Walther, Monitoring of the stratospheric ozone layer by laser radar, *Appl. Phys., B32*, 113, 1983.

Willets, D.V., and M.R. Harris, Attainment of frequency stable high energy operation of a CO_2 TEA laser by use of a telescope resonator, *IEEE J. Quant. Electron., QE-21*, 188, 1985.

Wolfe, W.L., and G.J. Zissis, (Eds.), Calculated change in bulk reflectance of ocean water with increasing concentration of phytoplankton, in *The Infrared Handbook*, Figure 3-124, Environmental Research Institute of Michigan, Ann Arbor, MI, 1978.

Zagwodzki, T.W., and D.L. White, Laboratory test results of the high-speed optical tracking system for the spaceborne geodynamic ranging system, in *Proceedings of the SPIE 1986 Technical Symposium on Optics and Optoelectronics*, Orlando, FL, April 1986.

Zwally H.J., R.H. Thomas, and R.A. Bindschadler, Ice-sheet dynamics by satellite laser altimetry, in *Proceedings of the IEEE International Geoscience and Remote Sensing*, Catalog # 81CH1656-8, 2, 1012, NASA TM 82128, GSFC, Greenbelt, MD, May 1981.

Zwally, H.J., Observing polar ice variability, *Ann. Glaciol., 5*, 191, 1984.